9-1-2011

Capillary Interactions Among Microparticles and Nanoparticles at Fluid Interfaces

Chuan Zeng
University of Massachusetts - Amherst, czeng@physics.umass.edu

CAPILLARY INTERACTIONS AMONG MICROPARTICLES AND NANOPARTICLES AT FLUID INTERFACES

A Dissertation Presented

by

CHUAN ZENG

Submitted to the Graduate School of the
University of Massachusetts Amherst in partial fulfillment
of the requirements for the degree of

DOCTOR OF PHILOSOPHY IN PHYSICS

September 2011

Physics

CAPILLARY INTERACTIONS AMONG MICROPARTICLES AND NANOPARTICLES AT FLUID INTERFACES

A Dissertation Presented

by

CHUAN ZENG

Approved as to style and content by:

Anthony D. Dinsmore, Chair

Benny Davidovitch, Member

Narayanan Menon, Member

Robert M. Weis, Member

Donald Candela, Department Chair
Physics

To those at the interface of science and philosophy.

ACKNOWLEDGMENTS

I would like to thank my advisor Professor Anthony D. Dinsmore for giving me the opportunity to join this project and his continuous help and guidance through all stages of graduate study. I would also like to extend my gratitude to the members of my committee, Professor Benny Davidovitch, Professor Narayanan Menon and Professor Robert M. Weis, for their helpful comments and suggestions on all stages of this project. I am glad to have Professor Fabian Brau joining us during his visit to UMass campus.

I acknowledge all the members in Dinsmore Research Group for making our work fun and fruitful together. I greatly appreciate what the Physics Department has been offering: rigorous training, vibrant environment, everyone's readiness to discuss, and the physicist's way of thinking.

I want to thank the NSF-supported Materials Research Science and Engineering Center on Polymers at UMass (MRSEC, DMR-0820506) and NASA Fluid Physics program (NASA 02-OBPR-03-C-0188-0122) for funding this research.

Finally thank my parents for unwavering support which is beyond what I can express in words. Thank my wife, Le, for sharing the tranquil life in Amherst, and wherever. I also have to thank Andrew, our son, for being healthy and happy, without which the thesis could not have been finished in such a manner.

ABSTRACT

CAPILLARY INTERACTIONS AMONG MICROPARTICLES AND NANOPARTICLES AT FLUID INTERFACES

SEPTEMBER 2011

CHUAN ZENG

B.Sc., UNIVERSITY OF SCIENCE AND TECHNOLOGY OF CHINA

M.Sc., UNIVERSITY OF MASSACHUSETTS AMHERST

Ph.D, UNIVERSITY OF MASSACHUSETTS AMHERST

Directed by: Professor Anthony D. Dinsmore

Particles can be adsorbed to liquid-fluid interface to minimize interfacial energy. The adsorbed particles interact in many ways. There has been a lot of theoretical predictions as well as experimental measurements of the interaction potential between particles confined at interfaces. Experimentally, we track multiple particles using optical microscope image processing of isolated pairs of particles and of more concentrated systems. Statistical methods were implemented to compute microparticle interaction forces from tracking data. The accuracy of different methods were tested with Monte Carlo simulation, which showed that care is needed to avoid artifacts. Our measurements confirmed the absence of significant pair-interactions among charged microparticles and liquid droplets at flat air-water interfaces. At the interface between water and a fluorocarbon, however, we observed strong interactions that cannot be explained by capillary interactions among neutral particles. Theoretically,

we focused on the capillary interaction mediated by the curvature of interface. The perturbation to a cylindrical interface upon adsorption of a single spherical particle is studied first. We present an analytical model of the interfacial shape and energy upon adsorption of a single particle, and then calculate the interaction between two particles. Based on our result for a cylindrical interface, we propose a general formula for the force on a particle on a curved interface having constant mean curvature (*i.e.*, not subject to an external forces). This study provides an important step toward understanding the interactions among interfacial particles.

TABLE OF CONTENTS

LIST OF TABLES

Table **Page**

LIST OF FIGURES

Figure **Page**

CHAPTER 1

INTRODUCTION

Since the beginning of last century [1], particles at liquid interface have been of great interest from fundamental science to engineering application [2, 3]. Particles confined at two-dimensional interface provide a ideal analogous system to study crystallization in two dimensions [4, 5], while particles packed around liquid droplets can act as emulsifier to stabilize droplets from coalescing [1, 6].

1.1 Surface tension and surface energy

The interface between two immiscible fluids is subjected to a positive tension [7]. The tension arises from the cohesive forces among the liquid molecules. In the bulk of one liquid phase, each molecule is attracted equally in every direction by neighboring liquid molecules. The molecules at the interface do not have the same type of molecules on all sides of them. Therefore, molecules at the interface are pulled inwards to its bulk phase, which creates a tension on the interface and forces the interface to contract to the minimal area. In terms of energy, interfacial tension is the energy cost of creating unit area of interface, *i.e.*, there is a positive interfacial energy proportional to the total area of interface.

1.2 Adsorption of microparticles at interfaces

To minimize surface energy, particles can be adsorbed to liquid-fluid interface. As illustrated in Figure 1.1, consider a spherical particle with radius R initially in phase I without loss of generality. The surface tension between the particle and phase I is

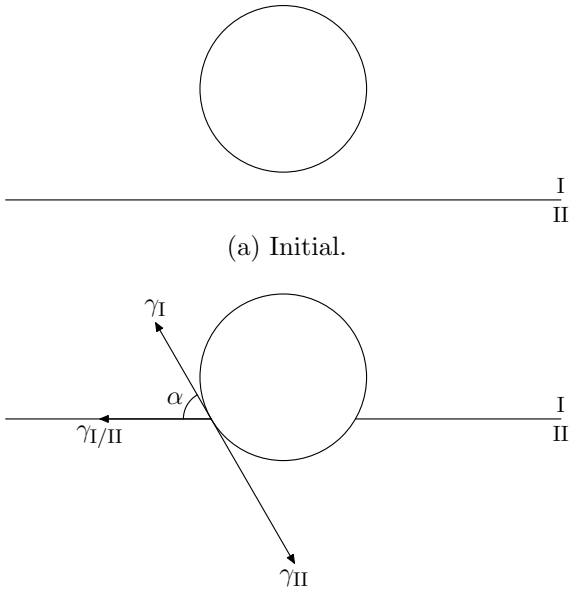

(a) Initial.

(b) Final.

Figure 1.1: Adsorption of particle at interface.

γ_{I}, and the surface tension between the particle and phase II is γ_{II}. The interfacial tension between phase I and phase II is $\gamma_{\mathrm{I/II}}$. The particle sits at the interface in the final state. Force balance at contact line along tangential direction gives the Young-Dupre equation [8]

$$\gamma_{\mathrm{I/II}} \cos\alpha + \gamma_{\mathrm{I}} = \gamma_{\mathrm{II}}, \tag{1.1}$$

which requires $|\cos\alpha| \leq 1$, *i.e.* $|\gamma_{\mathrm{I}} - \gamma_{\mathrm{II}}| \leq \gamma_{\mathrm{I/II}}$. In this case, the interfacial area was reduced by a disk with radius $R\sin\alpha$, and the area on the particle transferred from phase I to phase II was $2\pi R^2(1-\cos\alpha)$. Thus we have $\Delta E = -\gamma_{\mathrm{I/II}}\pi R^2 \sin^2\alpha + (\gamma_{\mathrm{II}} - \gamma_{\mathrm{I}})\, 2\pi R^2(1-\cos\alpha)$. Recalling $\gamma_{\mathrm{II}} - \gamma_{\mathrm{I}} = \gamma_{\mathrm{I/II}}\cos\alpha$, we get

$$\Delta E = -\gamma_{\mathrm{I/II}}\pi R^2(1-\cos\alpha)^2 \leq 0. \tag{1.2}$$

Thus the energy minimum is always achieved when particle sits at interface. Take water-air interface for example, $\gamma_{\mathrm{I/II}} = .07\ \mathrm{kg}\cdot\mathrm{s}^{-2}$, and $R = 1\ \mu\mathrm{m}$, then $\Delta E \sim 10^{-13}(1-\cos\alpha)^2$ J. Correspondingly, $\Delta E \sim 10^{-19}(1-\cos\alpha)^2$ J for nanoparticles. At

room temperature, $k_{\mathrm{B}}T \sim 10^{-21}$ J. Therefore, microparticles can usually be stably bounded at interfaces, while nanoparticles can escape from the interface owing to thermal fluctuations [9]. Particularly for horizontal interfaces, it is also important to notice that the force of gravity is negligible, since the change of energy is $\rho V g h \sim \rho g R^4 \sim 10^{-20}$ J for a microparticle to fall 1 μm.

Generally speaking, the experimentally observed contact angle depends on history. It exhibits hysteresis in a range between receding angle and advancing angle [8]. The surface inhomogeneity, either chemical (stains, blotches, blemishes) or physical (surface irregularities), also leads to nonuniformity in contact angle. For now, we assume no hysteresis and uniform contact angle. This is an important assumption, the experimental evidence to which will be shown for microparticles both indirectly and directly.

1.3 Interactions between particles

Microparticles at the interface interact with each other in various ways, which fall into three categories: electrostatic, capillary and Casimir. Furthermore, electrostatic and capillary effects usually couple together through the deformability of the fluid interface. The early study of this interaction was pioneered by Levine *et al.* [10, 11, 12], both theoretical and experimentally. As we will see, there has been quite a controversy over recent years about the overall interaction of microparticles at fluid interface.

1.3.1 Electrostatics

Charged particles in polar solvent are surrounded by a cloud of their counterions, which can be modeled to be distributed on a thin layer with a finite length l_{D} from the particle surface. This length l_{D} is called *Debye screening length*. The surface charge and the layer of counterion are usually combined as *Debye double-layer*. When a

particle is sitting at an interface of a polar solvent and a non-polar solvent, the double layer on the polar side forms an electric dipole [13, 14, 15]. Particles can thus repel each other in this way with energy proportional to $1/r^3$.

On the non-polar liquid side, surface charge is screened over a distance of several microns and the interaction reduces to Coulombic repulsive [16]. Although the mechanism of charge at the interface of particle and non-polar solvent is not yet clear, there are experimental evidences as well as proposed explanation [17, 18].

The experiments and theory on charged particles and electric-field-induced deformation will be reviewed in more detail in Chapter 2.

1.3.2 Capillary

Capillary plays an important role in particle interactions. Two different mechanisms have been identified in the literature and are summarized here: the deformation of interface by an externally applied force and the undulation of contact line arising from particle roughness and contact line pinning.

1.3.2.1 Deformation of interface

The shape of the interface is determined by Young-Laplace equation:

$$\Delta p = 2H\gamma. \tag{1.3}$$

Here Δp is the pressure difference across the interface, H is the mean curvature of the interface and γ is the interfacial tension. For an interface with height z written as a function of x and y in a flat reference plane with Cartesian coordinates, $2H = \nabla \cdot \dfrac{\nabla z(x,y)}{\sqrt{1+|\nabla z(x,y)|^2}}$. For quasi-flat interface,

$$|\nabla z(x,y)| \ll 1, \tag{1.4}$$

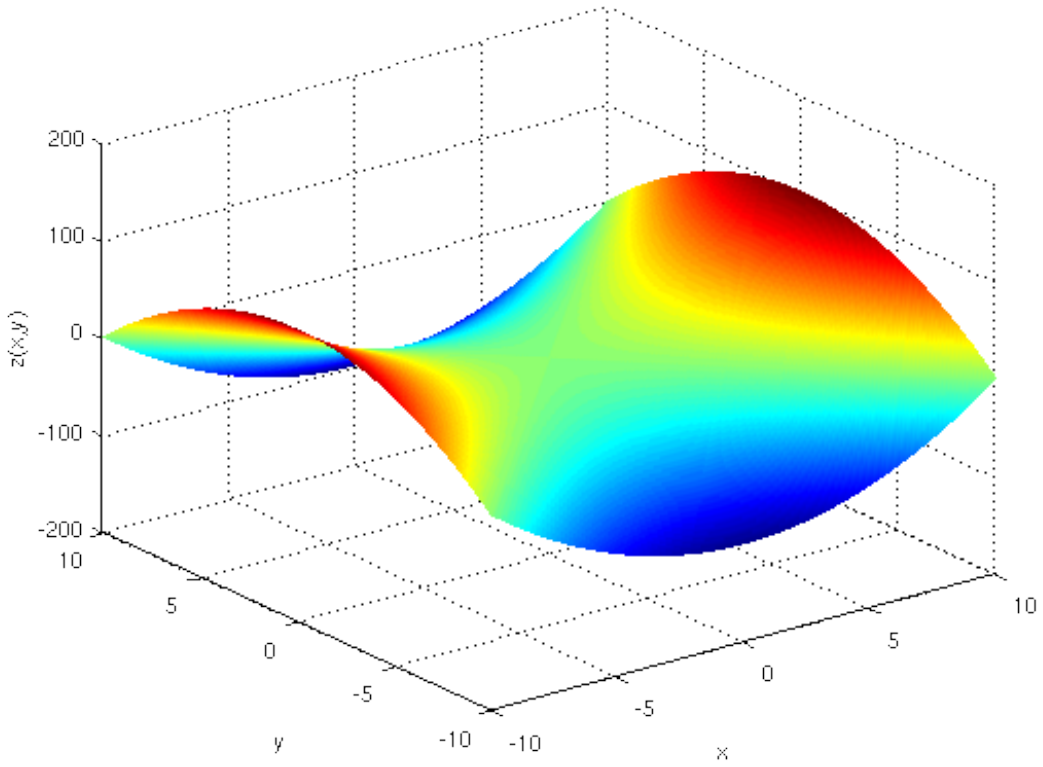

Figure 1.2: Curved interface: an example.

$2H = \nabla^2 z(x, y)$. Now the Young-Laplace equation is reduced to Laplace's equation

$$\nabla^2 z(x, y) = \frac{\Delta p}{\gamma}. \tag{1.5}$$

As an entry into capillary interactions, we consider the case when a normal force f acts on an azimuthally symmetric particle at the interface (Figure 1.3). The shape of interface is described as $z(r)$, because of the azimuthal symmetry about the vertical axis. r_c is the radius of contact line; γ is the interfacial tension. We assume that the interface is initially flat and ignore the force of gravity on the two fluids. Hence $\Delta p = 0$. Laplace's equation in cylindrical coordinate with azimuthal symmetry is

$$\frac{1}{r}\partial_r r \partial_r z = 0. \tag{1.6}$$

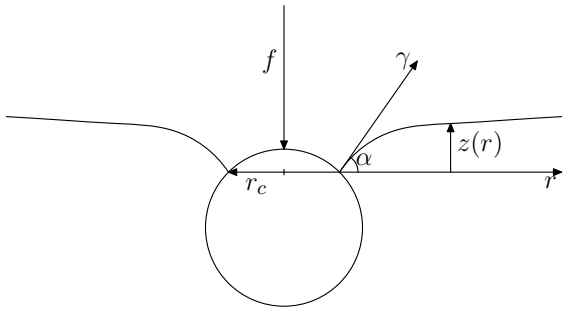

Figure 1.3: Interface deformed by normal force acting on particle. $\Delta p = 0$.

The force balance along the contact line gives the boundary condition

$$f = 2\pi r_c \gamma \sin\alpha. \tag{1.7}$$

With the assumption of Equation 1.4, Equation 1.7 reduces to

$$f = 2\pi r_c \gamma \, \partial_r z|_{r=r_c} . \tag{1.8}$$

Solving Equation 1.6 with Equation 1.8 yields

$$z = \frac{f}{2\pi\gamma} \ln \frac{r}{r_c}. \tag{1.9}$$

This deformation causes an interaction between particles [19]. The interaction energy is a combination of work done by the vertical forces on each particle plus the change of interfacial energy. It can be shown that the interfacial energy cancels the work done by one of the vertical forces. Thus the interaction between two particles is approximately the work done by one force f along z direction:

$$U = \frac{f^2}{2\pi\gamma} \ln \frac{r}{2R} \tag{1.10}$$

where R is the radius of particle. This interaction potential is analogous to electrostatics in two-dimension [20, 21]. The force f acts as line charge density λ, and

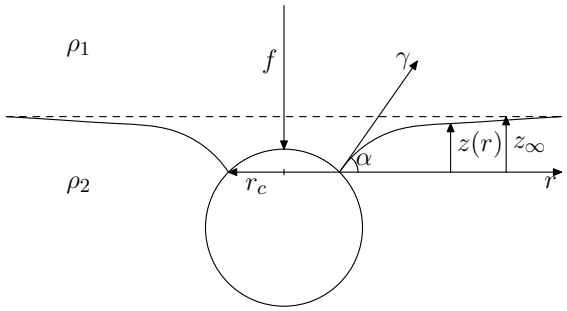

Figure 1.4: Interface deformed by normal force acting on particle. $\Delta p \neq 0$.

Table 1.1: Analogy between capillary interaction and two-dimensional electrostatics.

Capillary	Electrostatic (2D)
f	λ
γ	ϵ
$\frac{1}{2\pi\gamma} f_1 f_2 \ln d$	$-\frac{1}{2\pi\epsilon}\lambda_1\lambda_2 \ln d$

the interfacial tension γ acts as permittivity ϵ. However, the sign of interaction is opposite to that of electrostatics. The "capillary charges" of the same sign attract each other, while opposite capillary charges repulse.

The result of Equation 1.9 can be generalized to the case with gravity. The density mismatch of two fluids gives rise to a pressure difference across the interface

$$\Delta p = \Delta\rho g \left(z - z_\infty\right) \tag{1.11}$$

where $\Delta\rho = \rho_2 - \rho_1$. For the stable case, the low-density fluid is on top, corresponding to positive Δp. Note that $z\left(r_c\right)$ is defined to be zero and z_∞ is *unknown*. Δp is negative since the pressure decreases along z direction. Holding the assumption of Equation 1.4, we have the Young-Laplace equation in cylindrical coordinates:

$$\frac{1}{r}\partial_r r \partial_r z = \frac{\Delta\rho g \left(z - z_\infty\right)}{\gamma}. \tag{1.12}$$

Substituting $z-z_\infty$ with ζ, and defining *capillary length* $l_{\mathrm{C}} = \sqrt{\frac{\gamma}{\Delta\rho g}}$, we get a modified Bessel's equation:

$$\frac{1}{r}\partial_r r \partial_r \zeta = \frac{\zeta}{l_{\mathrm{C}}^2}. \tag{1.13}$$

With boundary conditions

$$\zeta(\infty) = 0, \tag{1.14}$$

$$f = 2\pi r_c \gamma \left.\partial_r \zeta\right|_{r=r_c}, \tag{1.15}$$

the solution to Equation 1.13 is $\zeta(r) = -\dfrac{f l_{\mathrm{C}} K_0\left(\dfrac{r}{l_{\mathrm{C}}}\right)}{2\pi r_c \gamma K_1\left(\dfrac{r_c}{l_{\mathrm{C}}}\right)}$, where $K_n(x)$ is the modified Bessel function of the second kind. Our definition of coordinate requires $z(r_c) = 0$, thus $z_\infty = -\zeta(r_c)$. Finally we get

$$z(r) = \frac{f l_{\mathrm{C}}\left[K_0\left(\dfrac{r_c}{l_{\mathrm{C}}}\right) - K_0\left(\dfrac{r}{l_{\mathrm{C}}}\right)\right]}{2\pi r_c \gamma K_1\left(\dfrac{r_c}{l_{\mathrm{C}}}\right)}. \tag{1.16}$$

For the limiting case of $r \ll l_{\mathrm{C}}$, Equation 1.16 reduces to Equation 1.9[1]. To satisfy Equation 1.4, we require $\partial_r z \le \left.\partial_r z\right|_{r=r_c} \ll 1$, *i.e.*, $f \ll 2\pi r_c \gamma$. For water-air interface, l_{C}=2.7 mm. For microparticles, $2\pi r_c \gamma \sim 10^{-7}$ N, so the preceding assumptions apply if $f \sim 10^{-7}$ N. The gravitational force on a particle is $\rho g V \sim 10^3 \times 10 \times 10^{-18}$ N $= 10^{-14}$ N $\ll 10^{-7}$ N.

In a macroscopic system, the normal force f could be provided by gravity, with a well-know demonstration being the *Cheerios effect* [22]. While a more general and elaborate calculation of interface shape was provided by Huh *et al.* [23], the linear superposition approximation of gravity-induced capillary interaction was proved to

[1]For $0 < x \ll 1$, $K_0(x) \to \ln\frac{2}{x} - \gamma_E$, where γ_E is Euler-Mascheroni constant (0.5772...). For $0 < x \ll \sqrt{2}$, $K_1(x) \to \frac{1}{x}$.

be good for sub-millimeter scale particles [24]. An interesting demonstration of this interaction was found in meniscus-climbing insects [25]. For charged particles, the *effective* normal force could be provided by electrostatics of the system, which was referred to as *electrodipping force* [18]. However, the superposition assumption is questioned when computing capillary forces between charged particles at an interface [26]. It was claimed that the two-particle term dominates and many-body interaction would emerge.

A bigger concern is whether the electric-induced capillary attraction can overcome the direct-electrostatic repulsion, which triggered quite a lot of theoretical debate [27, 28, 29, 30, 31, 32, 15]. In part this problem is complicated by the fact that the distribution of charge is typically unknown.

1.3.2.2 Undulation of contact line

In the previous derivation, we assumed that the contact angle is constant so that the contact line is a perfect circle. However, the contact line could be undulated, or irregular, in the presence of surface roughness and/or chemical inhomogeneity. The irregular wetting perimeter on the particle surface could also result in a significant long-range attraction [33]. In the calculation of this interaction, the geometry of the contact line is expressed in a multipole expansion, which leads to an elegant analogy to multipole expansions in electrostatics [34, 35, 36, 20]. Depending on the angle of mutual orientation, the interaction energy could exhibit a minimum, or it could represent a monotonic attraction [20]. Quantitatively [37, 36, 20], the interaction energy is much larger than $k_{\mathrm{B}}T$ for undulation amplitudes larger than 5 nm; for deviation of about 50 nm, the interaction energy is in the order of $10^4 k_{\mathrm{B}}T$.

Experimentally the irregular wetting behavior has been tested [38] and applied to create a variety of structures [39, 40, 41, 42]. Surface roughness of microparticle could be anisotropic, and it also makes particle different from each other. Unfortunately, we

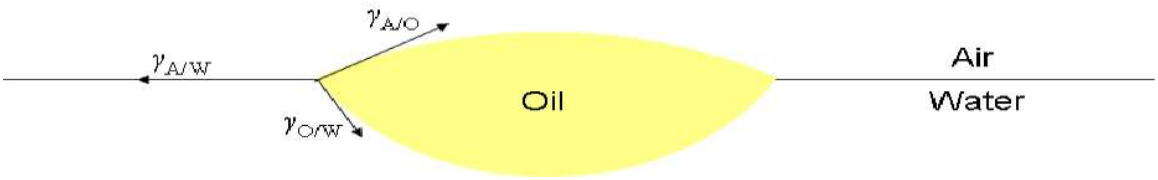

Figure 1.5: Adsorption of an oil droplet at water-air interface.

do not have good way to control or characterize surface roughness of microparticle. A good way to circumvent this complexity is investigating microdroplet instead of solid particle, since liquid does not support surface roughness (Figure 1.5). In Chapter 2 we present some results on microdroplets.

1.3.3 Casimir

Like the fluctuation of vacuum energy, the thermal-fluctuation of contact line and interface could also induce attractive interaction between microparticles [43, 44]. This interaction was shown to be very sensitive to the boundary conditions imposed at the contact line [45]. However, the resulting forces are too small to cause a significant attraction for colloid particles.

1.3.4 Anisotropic particles

When adsorbed to an otherwise flat interface, particles with anisotropic shape may cause deformation of the interface even without external forces. This is because the contact angle condition can not be satisfied without deforming the interface. The deformation of interface will further induce interaction among particles in absence of external normal force. Several groups [42, 46, 47, 48, 49] investigated anisotropic particles adsorbed to interface and showed the anisotropic interaction when gravity is insignificant. These study provide indirect evidence for the condition of constant constant angle.

1.4 The effect of interfacial curvature

Instead of being flat, the fluid interface may be curved before any particle is adsorbed. We are interested in the adsorption of particles to curved interfaces, as well as the interaction due to the curvature of the interface. To investigate the most elementary aspects of this problem, we focus on spherical particles. We aim at addressing the following questions: 1) Due to the curvature of interface, how does the adsorption energy change with respect to Equation 1.2? 2) Where does a particle go when adsorbed to an interface with nonuniform curvature? 3) Do particles interact with each other without external forces? If so, what are the implications for self-assembly of particles or stabilization of droplets using solid particles?

1.4.1 Curvature of surfaces

The mathematical characterization of surface curvatures is reviewed in this subsection.

At any given point of a surface, there is an infinite number of normal planes passing the normal direction of the surface (Figure 1.6). The intersection of the surface with any of those planes gives a curve, the curvature k of which can be found at the given point. The maximal and minimal values of k are defined as principal curvatures k_1 and k_2, with the corresponding planes called planes of principal curvatures. In differential geometry, this is essentially an eigenvalue problem about the shape operator[2] [50, 51, 52, 53]. The two principal curvatures are the eigenvalues of the shape operator at the point. For the special case of a sphere, the principal

[2]The shape operator is given in terms of the components of the first and second fundamental forms by the Weingarten equations:

$$S = (EG - F^2)^{-1} \begin{pmatrix} eG - fF & fG - gF \\ fE - eF & gE - fF \end{pmatrix}.$$

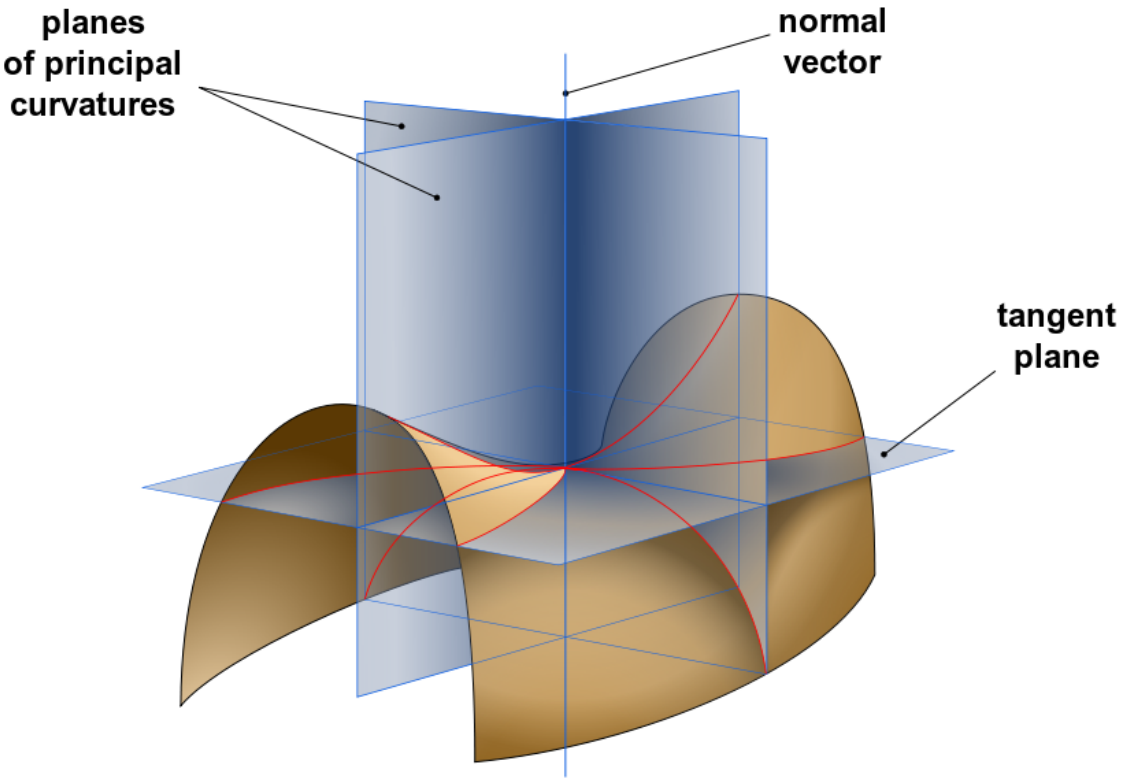

Figure 1.6: Saddle surface with normal planes in directions of principal curvatures. (Figure from Wikipedia.)

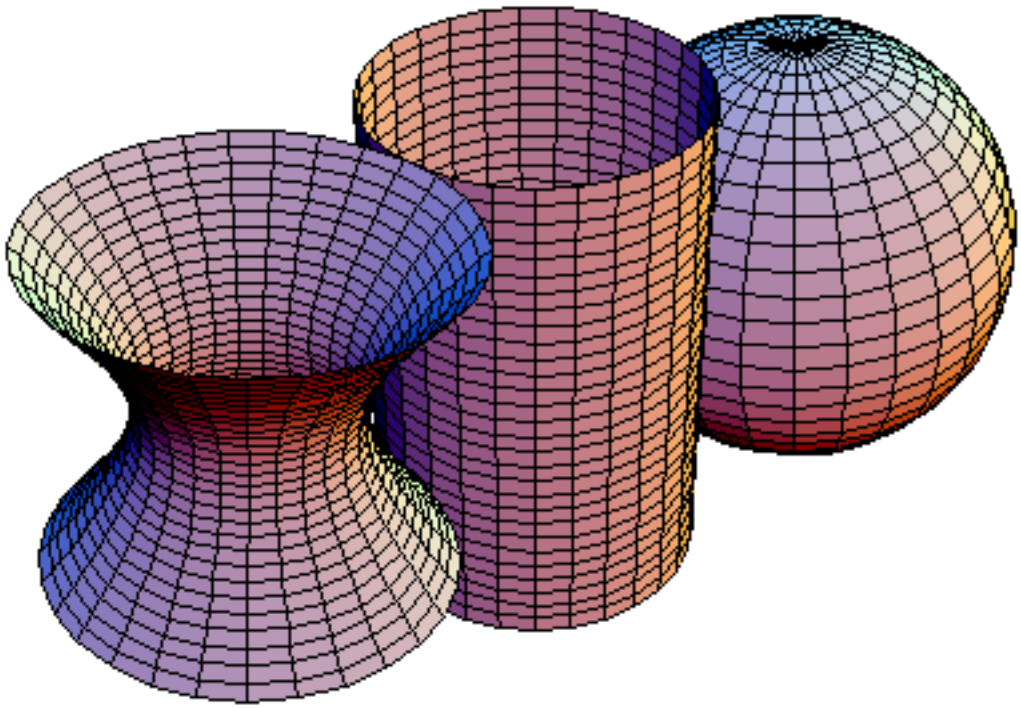

Figure 1.7: Surfaces with constant negative, zero and positive Gaussian curvature. From left to right: a surface of negative Gaussian curvature (hyperboloid), a surface of zero Gaussian curvature (cylinder), and a surface of positive Gaussian curvature (sphere). (Figure from Wikipedia.)

curvatures are degenerate. In this case all the normal planes give the same value of k, which equals the inverse of the sphere radius.

The *mean curvature*, as introduced in Section 1.3.2.1, is the average of principal curvatures [54]:

$$H := \frac{1}{2}\left(k_1 + k_2\right). \tag{1.17}$$

We also define Gaussian curvature K as

$$K := k_1 k_2. \tag{1.18}$$

For example, Figure 1.7 shows surfaces with constant negative, zero and positive Gaussian curvature.

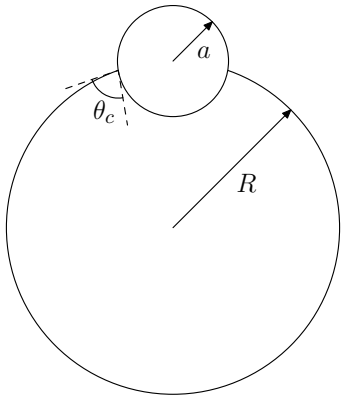

Figure 1.8: A spherical solid particle adsorbed to a spherical liquid drop or gas bubble.

1.4.2 Spherical interface

Consider a spherical solid particle with radius a adsorbed to a spherical liquid drop or gas bubble with radius R (Figure 1.8). Like the case of flat interface, the contact angle condition can be trivially satisfied all around the contact line by adjusting the relative distance of the particle center and drop/bubble. This is in principle due to the axisymmetry around the line connecting the center of particle and interface. The interface remains perfectly spherical. By calculating the interfacial energy before and after the adsorption while holding the radius or volume of drop fixed, the adsorption energy can be shown as [55, 56]

$$\Delta E = \Delta E_{\text{flat}} \left[1 + O\left(\frac{a^2}{R^2}\right)\right], \tag{1.19}$$

$$= \Delta E_{\text{flat}} \left[1 + O\left(a^2 H^2\right)\right], \tag{1.20}$$

where ΔE_{flat} is the adsorption energy for flat interface (Equation 1.2).

Because of symmetry, the first particle adsorbed to spherical interface does not have any preference on the angular position with respect to the center of interface. Even if more than one particle is adsorbed, the interface will still remain spherical. As a result, the contact line for each particle remains perfectly circular, and the capillary

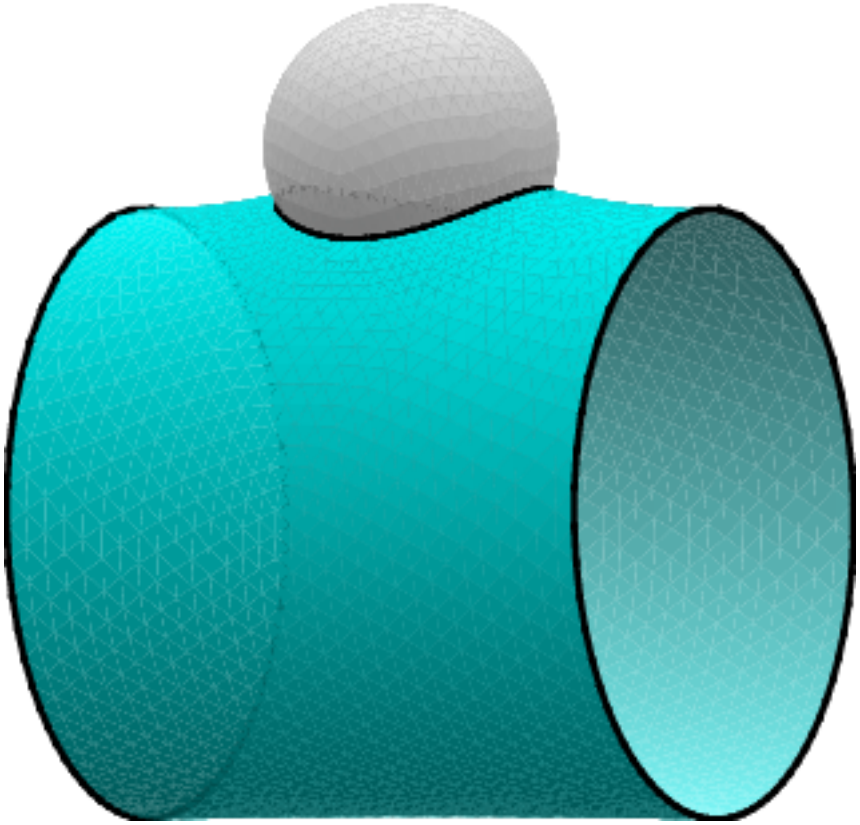

Figure 1.9: A spherical solid particle adsorbed to a cylindrical interface.

force on each particle has zero lateral component. The curvature of spherical interface does not lead to any interaction among adsorbed particles.

1.4.3 Cylindrical interface

The cylindrical interface stands out as we look for the simplest shape of an interface that can break the axisymmetry around the contact line (Figure 1.9). However the relative height of the solid particle is adjusted, the contact angle condition can not be satisfied at all points around the contact line simultaneously. As a result, the cylindrical interface has to be deformed around the particle. We solve for the perturbed shape of interface in Chapter 3 and then show that the deformation leads to interaction among adsorbed particles.

Anisotropic particle and cylindrical interface both cause interfacial deformation by introducing geometric frustration to the condition of contact angle. It is not a surprise that anisotropic particles interact with each other at a cylindrical interface. Lewandowski *et al.* [57, 58, 59] conducted experiments with anisotropic particles at nonplanar interfaces, in which shape-induced oriented assembly was observed. Also a agreement with theoretical model was shown. These work provides another set of indirect evidence to the condition of constant contact angle.

1.4.4 Catenoid interface

As a pioneering work on particles at curved interface, Wurger studied the special case of a catenoid-shaped interface theoretically [60]. The catenoid is a three-dimensional shape with a mean curvature of zero (Figure 1.10). The Gaussian curvature of a catenoid, however, is nonzero and nonuniform over the surface. In [60], the author predicted the motion of adsorbed particle at the catenoid interface as well as the possible pattern which could be formed by the particles.

By contrast, cylindrical interface has zero Gaussian curvature and nonzero mean curvature, and the curvatures of an unperturbed cylinder are uniform everywhere on the surface. Our modeling on cylindrical interface and Wurger's result on catenoid interface would perfectly complement each other in the efforts toward arbitrarily curved interfaces, as we summarized in Chapter 5.

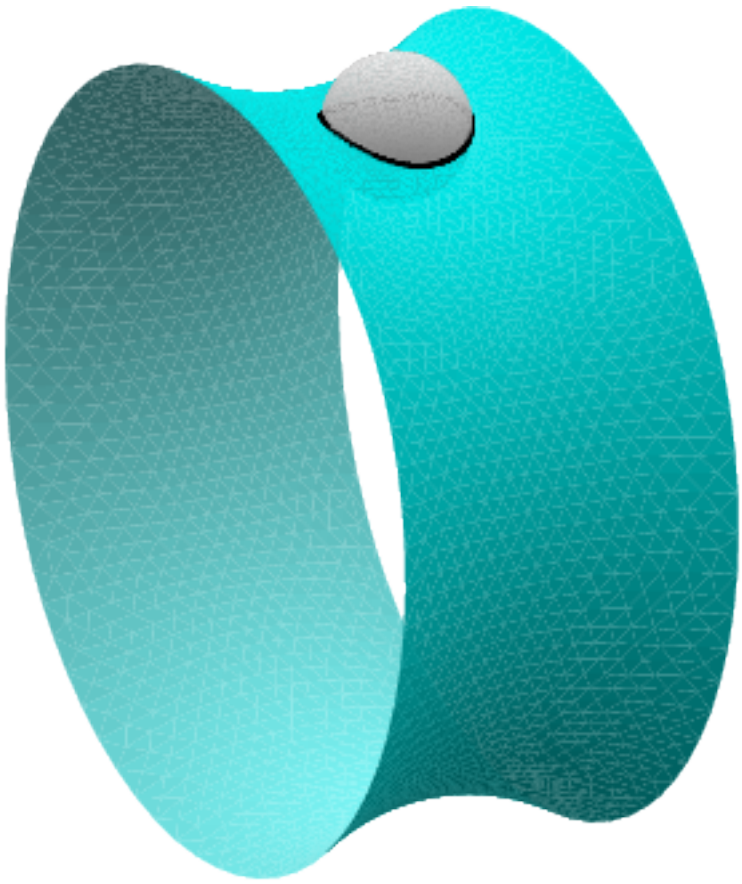

Figure 1.10: A spherical solid particle adsorbed to a catenoid interface.

CHAPTER 2

PAIR INTERACTION MEASUREMENT

2.1 Introduction

There has been substantial effort in the past decade to measure the pair interaction of particles at interface. In this section, I provide a summary of recent experimental results as well as what needs to be done in the future. In the following sections, I describe original experiments on the interactions involving not only particle monomers but also clusters of particles.

Nikolaides *et al.* [61, 62, 63] studied the dynamics of particles trapped in a secondary minimum at a separation of approximately four particle diameters and measured the potential energy curve near that minimum (Figure 2.1). Poly(methyl methacrylate) (PMMA) particles stabilized with poly(hydroxystearic acid) were adsorbed on water droplets in decahydronaphthalene (decalin). A seven-particle hexagonal crystallite was investigated with the center-to-center distance r measured over time. The potential was obtained from inverting the Boltzmann distribution of $P(r)$. It was demonstrated that there was a long-range attractive interaction between charged particles. The particles have a long-range repulsive interaction owing to their charges. The authors proposed that the long-range attraction arose from distortion of the interface by an electric field caused by the charge on the particles.

Aveyard *et al.* [64] determined long-range repulsive force as a function of separation between two charged, spherical polystyrene particles (2.7 μm diameter) at a interface between water and a mixture of decane and undecane using laser tweezers. The interaction forces as large as piconewtons were reported.

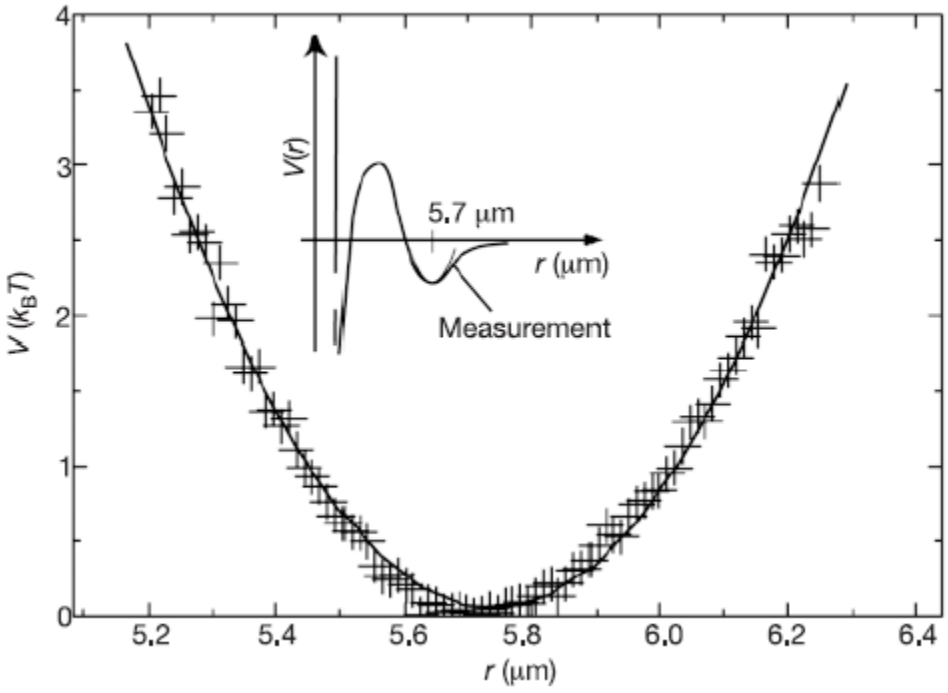

Figure 2.1: Measured secondary potential minimum (from [61]).

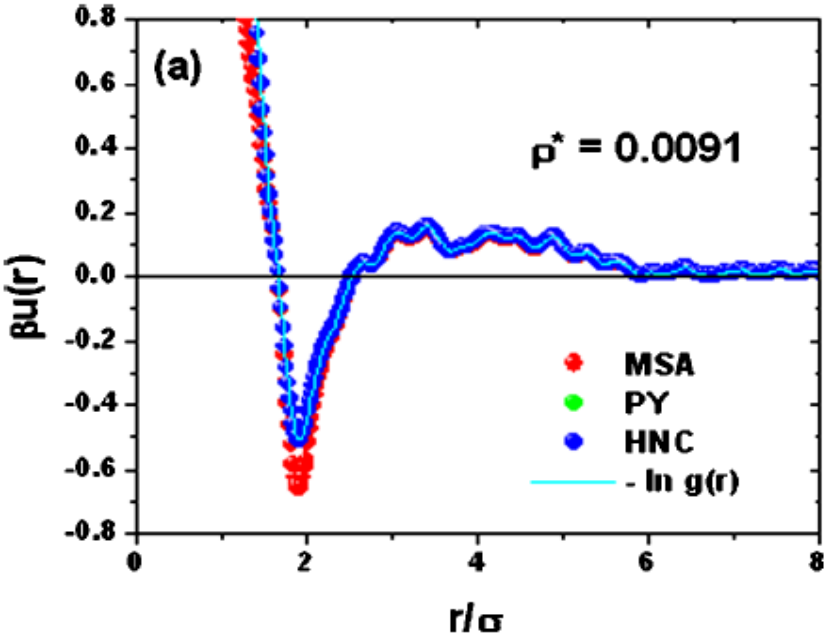

Figure 2.2: Measured pair potential interaction (from [65]).

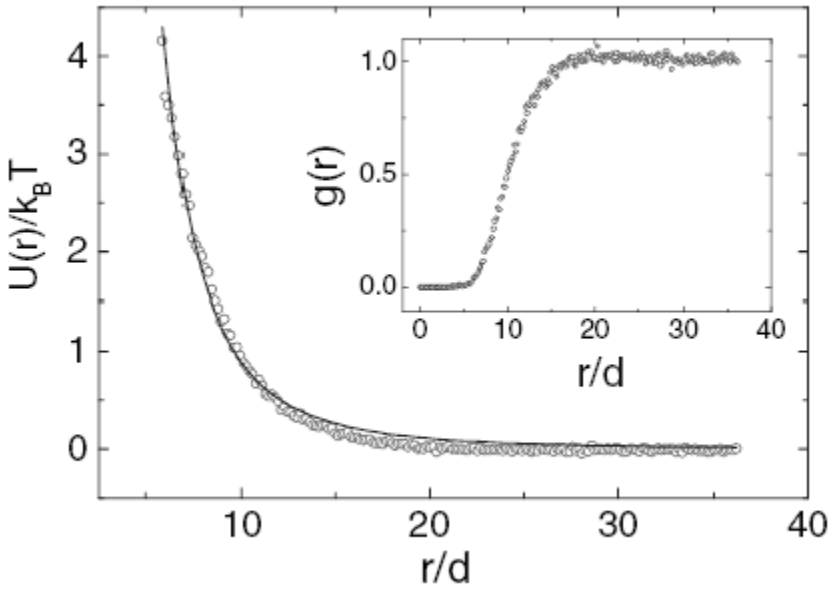

Figure 2.3: Repulsive potential extracted from $g(r)$ (from [66]).

Other groups investigated the spatial distribution of particles at flat interface (*e.g.* [65, 66]) and calculated the interacting energy from radial distribution function $g(r)$. Gomez-Guzman *et al.* measured the attractive interactions of colloidal particles at water-air interface using inverse Ornstein-Zernike convolution method (Figure 2.2). The particles reported in the article were non-fluorescent polystyrene sulfate particles, but the same behavior was also observed with fluorescent particles [67]. Chen *et al.* [66] spread anionic carboxyl polystyrene latex spheres at a water-air interface and inverted the Boltzmann distribution of $g(r)$ (Figure 2.3). Since in those experiments an ensemble of many particles was examined, the conclusions regarding the 2-body potential are valid only with the assumption that the pair interaction is additive.

It is worth noting that the previous measurements do not match each other. The secondary minimum observed in [61] did not appear in either [65] or [66]. And in [66] there is no attraction, while [65] showed attraction over shorter range than repulsion. As suggested in [61], the interaction is highly sensitive to surface properties,

charge and pH, as well as salt concentration. The interaction may also depend on the type of oil used (as we report in this thesis). The different charge of particles may affect the mechanism of adsorption in the first place [68, 69, 70]. Moreover, the interactions might not be pair-wise additive. Therefore, to precisely and convincingly measure the interaction potential, a *single* pair should be *isolated* from other particles and long time dynamics would be necessary to quantify the weak interaction on the order of $k_{\mathrm{B}}T$. The effect of salt concentration *etc.* could be addressed after then. Hence we performed experiments on highly diluted colloid system and measured the pair interaction. We focus on the air-water interface for comparison the results of [61, 62, 63, 65, 66]. We also show data for the interface between water and a fluorocarbon oil, which gives quite different results.

2.2 Sample preparation

Carboxyl-modified polystyrene bead suspensions in water were purchased from Interfacial Dynamics Corporation. We use two types of particles with diameters of 1.7 μm (Surfactant-Free Carboxyl White Polystyrene Latex, Product Number: 7-1800, Batch Number: 739,1, SKU: C37277) and 2.0 μm (Surfactant-Free Fluorescent Yellow Green CML Polystyrene Latex, Batch Number: 2-FLY-2K.3). Because of the carboxyl surface group, these particles are negatively charged in polar solvent. As mentioned above (Section 1.3.1), 0.01 M NaCl are usually added to the suspension to reduce the Debye length of charged particles. We are investigating both the water-air and water-oil interfaces. Oils used to create interface include silicone oil, hexamethyldisiloxane, and 1,1,1-trifluoroheptan-2-ol, which provide a variety of density, viscosity and hydrophobicity.

Due to the sensitivity of interfacial experiments, it is essential to clean all chambers and glassware thoroughly and carefully [71, 72]. With contaminated interface, the particles will form various immobile mesostructures. In our experiment, we soaked

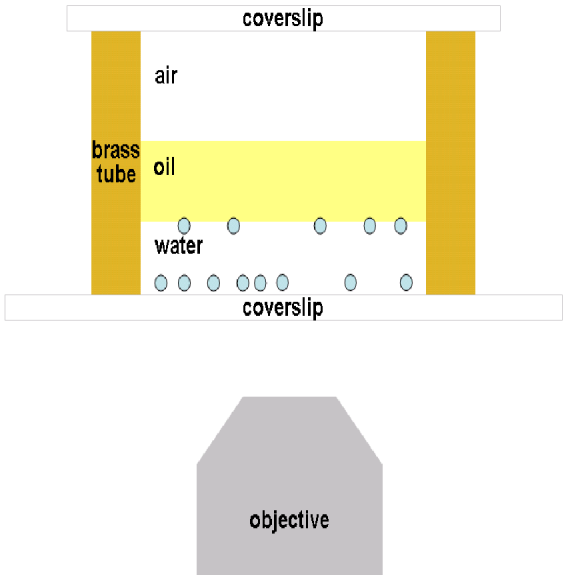

Figure 2.4: Microscopy cell.

glassware in sulfuric acid (NOCHROMIX, with oxidizer) for 12∼24 hours. Brass tubes (if applied) are washed with detergent (Sparkleen) in hot water. All parts of chamber are successively rinsed with toluene, methanol, deionized water (Millipore Direct-Q System) and air dried for 12∼24 hours.

A quasi-horizontal interface was created by adding the aqueous phase and oil phase into a cylindrical chamber (Figure 2.4). We use brass tube as the wall of chamber to reduce the thermal-induced flow in the system. By use of the brass tube, flow was suppressed from about 1 μm/s to .01 μm/s. The sedimentation of bulk particles toward the bottom glass could also cause convective flow, thus a waiting time of about 6 hr is usually necessary for the sedimentation to complete before pair-interaction measurements were done.

For water-air interface experiments, water without particles was added into the chamber, Afterward, about 10 μL methanol suspension of particles was added on top using a pipette, as a standard technique to spread particles onto water-air interface. Very diluted suspension of particles was prepared for the experiments of isolated pair measurements. Particles usually aggregate in methanol suspension since they are not

charge-stabilized. Thus our methanol suspension was typically sonicated for about 5 minutes before use. For water-oil interface experiments, water suspension of particles and oil was added into the chamber successively. The phase with higher density was added first and the other phase was added on top.

To circumvent irregular wetting (Section 1.3.2.2), microdroplets of oil were made by shaking a mixture of oil and water (volume fraction 1/1000). Microdroplets of oil at the water-air interface could be found under optical microscope.

2.3 Imaging and processing

An inverted optical microscope (Zeiss Axiovert 200) was used to image particles at flat interfaces, while confocal microscopy was necessary for experiments with curved interfaces. Objectives of 20×, 40×, and 63× were used for different magnification needs. Images were recorded with a charge-coupled device (CCD) camera and digitized with a frame grabber (Imagination PXC200A, controlled by OpenBOX).

The digital images obtained through microscopy were analyzed with Interactive Data Language (IDL, ITT Visual Information Solutions). The centroids of particles were located and tracked over a time period. The IDL code distributed by Crocker and Grier was used [73]. Because we are particularly interested in tracking pairs of particles over a long period of time, in-house code was also developed to track a small number of particles efficiently[1]. We avoided simultaneously loading a full stack of TIFF images to memory. Instead, only a few subsections of each frame was loaded based on the position of target particles in the previous frame and the knowledge on the diffusivity of the particles. When tracking isolated pairs, two subsections was loaded from each frame, corresponding to the pair of particles being tracked.

[1]IDL scripts available on servers Narmada2 and Walnut: `cfeature.pro`, `ctrack.pro`.

2.4 Measurement of diffusion coefficient

Bounded particles undergo Brownian motion in two dimensions. We can estimate the diffusion coefficient as $D = \frac{k_B T}{6\pi\eta R}$. To be specific, $D \sim 10^{-13}$ m^2/s for a microparticle immersed in bulk water. In the time scale we are interested in ($\sim$1 s), the mean square displacement of microparticles at the interface would be in the range of microns, which can be resolved with our optical microscope apparatus.

In the case of quasi-flat interface, the diffusion coefficient can be measured by fitting the plot of $\langle r^2 \rangle$ as a function of t. In the presence of measurement error σ and a constant flow v, the mean squared displacement is a quadratic function of time t:

$$\langle r^2 \rangle = \sigma^2 + 4Dt + v^2 t^2. \tag{2.1}$$

If the diffusion is isotropic, Equation 2.1 can be decomposed onto Cartesian coordinates as

$$\langle x^2 \rangle = \sigma_x^2 + 2Dt + v_x^2 t^2, \tag{2.2}$$

$$\langle y^2 \rangle = \sigma_y^2 + 2Dt + v_y^2 t^2. \tag{2.3}$$

As a result, we can estimate σ, D, and v simultaneously through a 2nd order polynomial fit. The measurement error of $\langle r^2 \rangle$ is taken into account in the polynomial fit. Representing the precision of particle tracking, σ turned out to be on the order of .1 pixel.

Figure 2.5 shows the mean square displacement $\langle r^2 \rangle$ of one particle as a function of time, with magnification of 8.1 pixel per micron. The particle is at the interface of water and silicone oil and is separated from other particles ($>\sim$ 100 micron). The solid curve is a parabola fit. Using Equations 2.1, 2.2, 2.3, we obtained $\sigma = .21$ pixel (.026 μm) indicating subpixel resolution. The fitted value of the diffusion coefficient $D = .0072$ μm^2/s. Compared with $D = .29$ μm^2/s for particle immersed in water

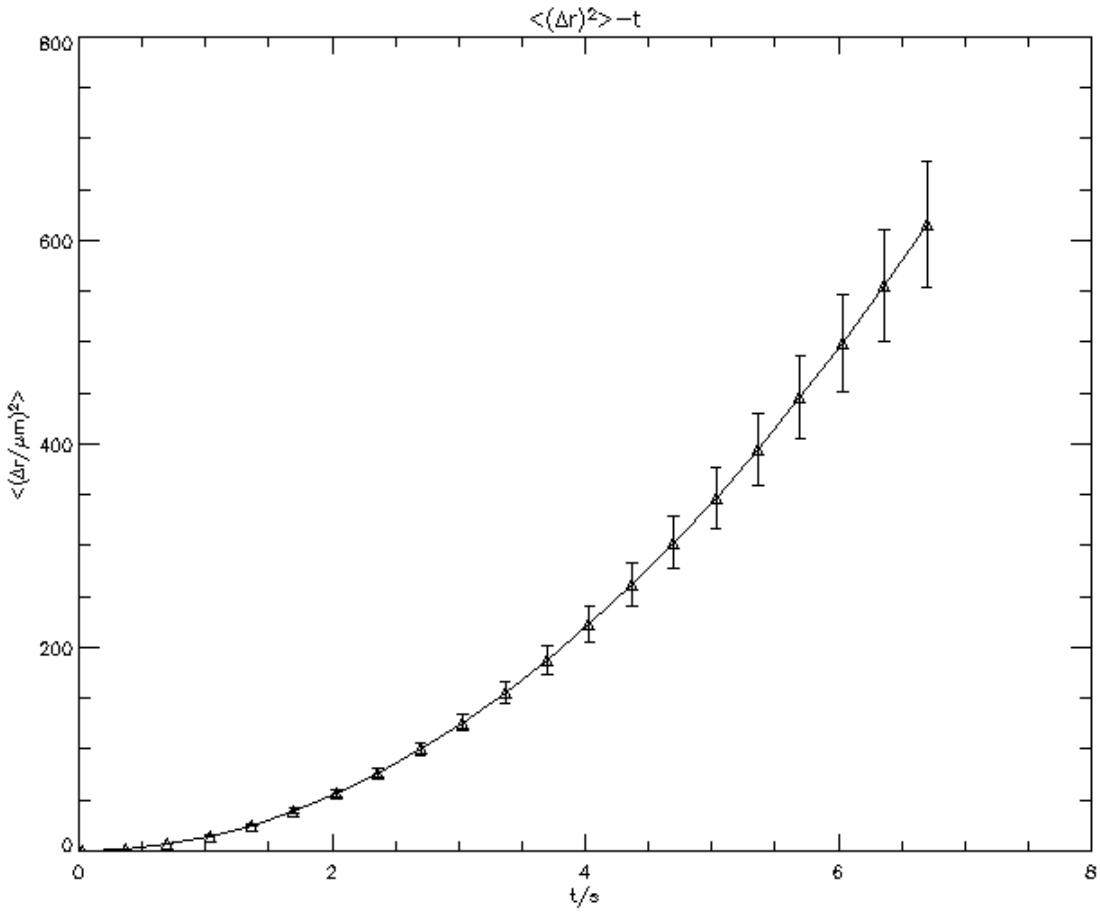

Figure 2.5: Mean-square displacement vs. time.

and $D = .0054\ \mu\text{m}^2/\text{s}$ in silicone oil, we can determine that the particle was located at the interface. The fitted value for v is $.038\mu\text{m/s}$. Then it takes about 45 min for a particle to drift over a distance of 100 μm, which would provide enough statistics for our measurement. The diffusion coefficient varies for different particles in the same system but is of the same order of magnitude ($\sim .01\ \mu\text{m}^2/\text{s}$). The variation in values of D suggests that particles might differ with respect to surface roughness or depth of immersion.

2.5 Measuring interaction between particles

In our system, the pair interaction potential between particles is typically weak, in some cases changing by much less than $k_\text{B}T$ per micron. As a result, thermal fluctuations are significant and the particles undergo diffusive motion rather than deterministic motion. To measure this $\sim k_\text{B}T$ potential through particle tracking, several statistical methods were investigated. The efficacy of each method was tested with simulated two-dimensional diffusion data.

Since we measured the pair separation as a function of time, it is straightforward to approximate the probability distribution p as a function of separation r over time as the equilibrium probability distribution. The potential of weakly interacting systems can be extracted by inverting the Boltzmann equation $U(r)/k_\text{B}T = -\ln p(r)$. This approach discards the dynamical information of the system, *i.e.*, the time-dependence of pair separation is not appreciated. As we show below, this method is subject to erroneous results when there is a strong adhesion at contact because the initially random distribution of particles is not in equilibrium.

For pairs out of equilibrium, Crocker and Grier [73] introduced the Markovian Dynamics Extrapolation (MDE) method. At first, the separation r between two particles is measured over a time period. By discretizing separation into small but finite bins, each measured r can be mapped into a particular bin (as illustrated in

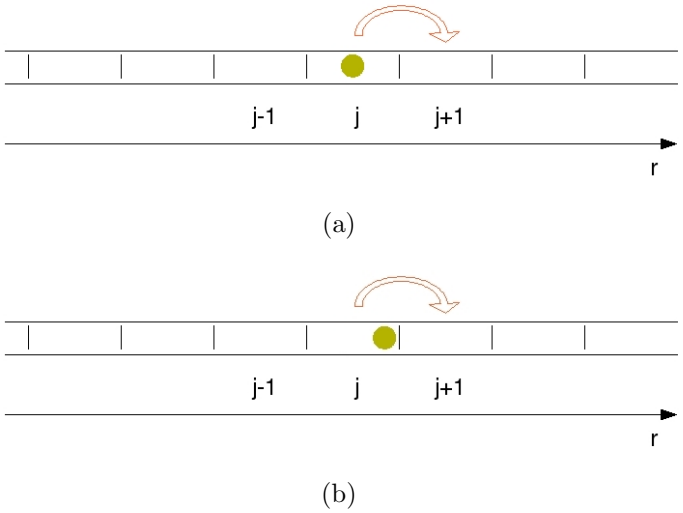

Figure 2.6: Discretized separation. The resolution within each bin is lost during the discretization. As a result, cases (a) and (b) are not distinguished after the discretization.

Figure 2.6a). Here we generally chose the bin size as the measurement error σ obtained in Section 2.4. After each time interval, r will jump from the j^{th} bin to the i^{th} bin (while it may also stay in the same bin, in which case $i = j$). Due to the nature of diffusion, the jump of observable r in a number of bins is a Markovian Process, which can be characterized by a transition probability matrix $\mathbf{P}$. For a measurement of $r(t)$ in a finite range of time, we can count the number of times n_{ij} when r jumped from the j^{th} bin to the i^{th} bin, divide it by the total number of times n_j when r jumped out from the j^{th} bin, and obtain the element p_{ij} of $\mathbf{P}$. With appropriate normalization condition, we can solve for equilibrium probability density ρ for each bin. The equilibrium distribution is just the eigenvector of $\mathbf{P}$ corresponding the eigenvalue 1.

In our implementation of Markovian Dynamics Extrapolation, we developed a Monte Carlo scheme to estimate the error of calculated $U(r)$[2]. Statistically, p_{ij} measured in this way obeys the binomial distribution. In order to estimate the error in

[2]IDL scripts available on servers Narmada2 and Walnut: `cpotential.pro`.

the measurement of p_{ij}, we can replace each n_{ij} with a random number n'_{ij} from a binomial distribution with probability p_{ij} and n_j trials. Using this randomized n_{ij}, perturbed matrix elements p'_{ij} are generated. Note that the expectation of p'_{ij} is exactly p_{ij}. However, the sum $\sum_i n'_{ij}$ is not guaranteed to be n_j. Renormalization would be necessary. Then a new result $U'(r)$ can be calculated from each randomized transition probability matrix $\mathbf{P'}$. By repeating this randomization N times, we have N perturbed potential measurement $U'(r)$. The measurement error of $U(r)$ is obtained as $\frac{\sigma_{U'(r)}}{\sqrt{N}}$, where $\sigma_{U'(r)}$ is the standard deviation of $U'(r)$ over different randomization.

Discretizing the continuous separation r into finite bins is required in both the direct Boltzmann inversion and Markovian Dynamics Extrapolation. The error introduced by the discretization increases with the size of bin. When the pair interaction is weak compared with $k_{\mathrm{B}}T$, the potential calculated in these ways is dominated by error. We confirmed this error with Monte Carlo simulation of free diffusion in two dimensions. The position of two particles as a function of time was generated from a simulation of free diffusion. The separation between two particles was extracted as a function of time, from which we applied the Markovian Dynamics Extrapolation to calculate the interaction potential. Even though the particles are diffusing independently in the simulation, the calculated potential shows complex features of order $k_{\mathrm{B}}T$. Figure 2.7 shows the calculated potential from a simulation of random walk with parameters of a typical experiment, in which we observe the motion of particles over a period of 30 min. The error estimation obtained by our Monte Carlo scheme turned out to be much smaller than the discrepancy of the potential estimation, because in our error analysis we did not take into consideration the error introduced by the discretization (Figure 2.6). We also ran the simulation as a virtually extended experiment, corresponding to 12 hr of observation. As shown in Figure 2.8, the error bars became narrower, however, the calculated potential is still far from being flat.

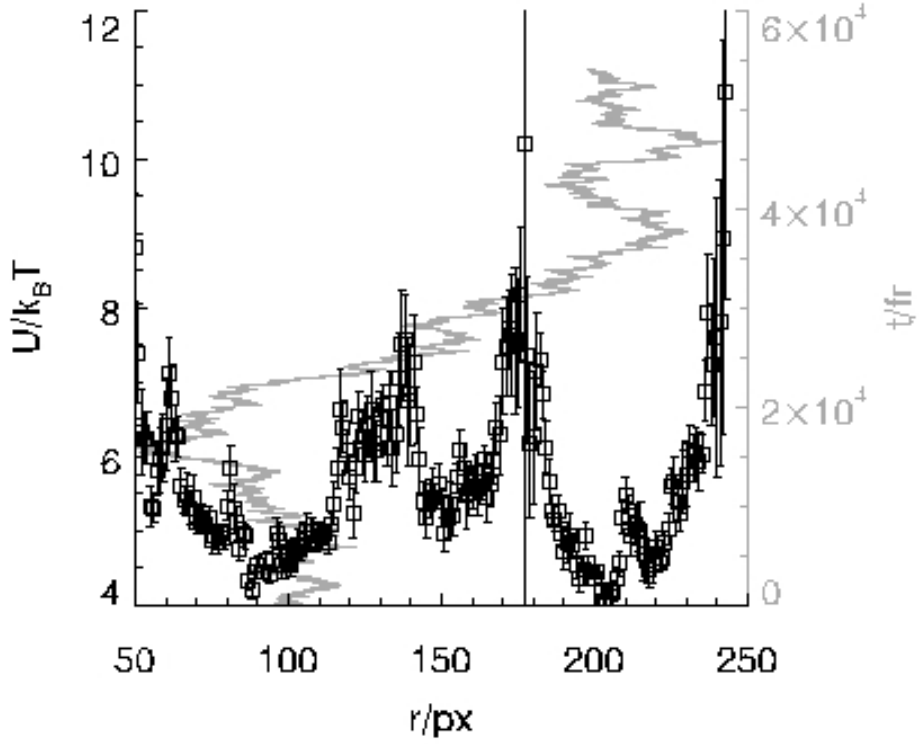

Figure 2.7: Interaction potential calculated using MDE from a simulation of random walk with parameters of a typical experiment. The diffusion coefficient was .03 px^2/fr. The position of particles was simulated for 54000 fr, corresponding to 30 min of experiment observation with video rate 30 fr/s.

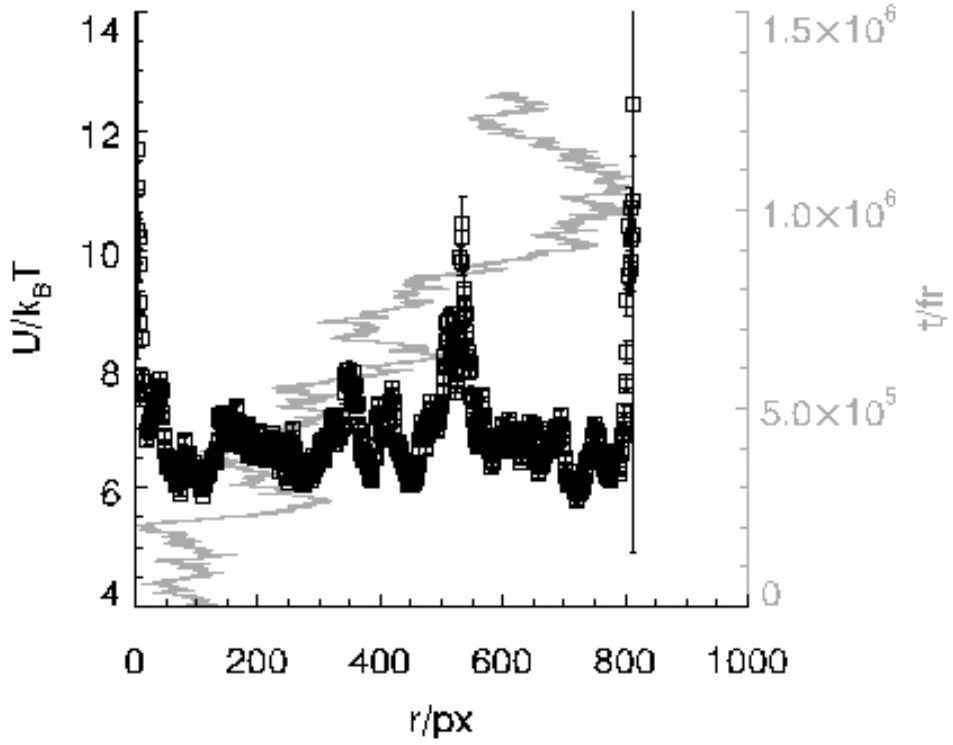

Figure 2.8: Interaction potential calculated using MDE from a simulation of random walk for a virtually extended experiment. The diffusion coefficient was .03 px^2/fr. The position of particles was simulated for 1296000 fr, corresponding to 12 hr of experiment observation with video rate 30 fr/s.

In order to avoid any artificial potential due to systematic error, an alternative method introduced by Sainis *et al.* [74] was modified and applied to our analysis. This method involves computing the drift velocity of one particle v with respect to another. This velocity was then converted to the interaction force through the Stokes-Einstein relation

$$f = \frac{k_{\mathrm{B}} T v}{D_{\mathrm{eff}}}. \tag{2.4}$$

The *effective* diffusion coefficient D_{eff} was also computed from the statistics of particle motion, as described below.

In order to measure the interparticle force at a particular separation r, the two particles were initially held with two optical tweezers at distance r in [74]. The particles were then released for a short time interval Δt, after which the distance between them were measured as r'. One such cycle generates a measurement of drift velocity

$$v(r) = \frac{r' - r}{\Delta t}. \tag{2.5}$$

Statistics of $v(r)$ was obtained by repeating the same cycle for many times. The mean $\langle v(r) \rangle$ and the effective diffusion coefficient $D_{\mathrm{eff}}(r)$ were obtained from the distribution of $r' - r$, which was fitted to the Gaussian form

$$p\left(r' - r\right) = \frac{1}{\sqrt{2\pi\sigma^2}} \exp\left[-\frac{\left(r' - r - \langle v \rangle \Delta t\right)^2}{2\sigma^2} \right], \tag{2.6}$$

where $\sigma^2 = 2 D_{\mathrm{eff}} \Delta t$. D_{eff} obtained this way is the effective diffusion coefficient of one particle with respect to the other. For non-interacting particles, it is the sum of the diffusion coefficients of both particles in the lab frame.

Optical tweezers was not applied in our experiment. In our analysis, the statistics of $v(r)$ was accumulated each time the pair separation $r(t)$ is in the range of $\left(r - \frac{1}{2}\Delta r, r + \frac{1}{2}\Delta r\right)$. Then

$$v(r) = \frac{r(t + \Delta t) - r(t)}{\Delta t}. \tag{2.7}$$

Although the discretization with bin size Δr is still needed, $v(r)$ is calculated exactly in the equation above.

We usually chose the bin size Δr to be one pixel and $\Delta t = 1$ fr. Because in each of our experiment data set, the separation r ranges over the order of 100 px, this would generate about 100 data points for a typical $v - r$ or $F - r$ curve. Choosing a smaller Δr results in less statistics in each bin and thus wider error bars, while a larger Δr would reduce the total number of data points in the $v - r$ curve.

Figure 2.9 shows the calculated drift velocity from a simulation of random walk with parameters of a typical experiment. In the simulation, we observe the motion of particles over a period of ∼45 min, which is comparable to our experimental data sets. The standard deviation for all measured v is σ_v =.14 px/fr, which is comparable of the width of error bars. In a typical experimental setup, the particle diameter is 1.7 μm. The 20× objective corresponds to a magnification of 1.49 px/μm[3]. For D_{eff} = .18 px^2/fr, the conversion factor from drift velocity to interaction force is 35 fN·fr/px. Then σ_v corresponds to $\sigma_F = 5$ fN.

Due to lack of statistics on both ends of the $v - r$ curve, the first few data points (corresponding to shortest range) always show repulsion, while the last few points usually show attraction. As a result, we only trust the points in the midrange of each $v - r$ curve, although we chose to show all data points in the plots of result. The number of points to be discarded is roughly determined by the ratio of root mean square displacement $\sqrt{2D_{\text{eff}}\Delta t}$ to bin size Δr, where Δt is the time interval. Since $(-3\sigma, 3\sigma)$ covers more than 99% of a normal distribution[4], we chose $3\dfrac{\sqrt{2D_{\text{eff}}\Delta t}}{\Delta r}$. For $\Delta t = 1$ fr, $\Delta r = 1$ px, D_{eff} = .18 px^2/fr, we have $3\dfrac{\sqrt{2D_{\text{eff}}\Delta t}}{\Delta r} \approx 2$.

---

[3]The magnification is the same for all data reported here unless otherwise stated.

[4]$\int_{-3\sigma}^{3\sigma} \dfrac{1}{\sqrt{2\pi}\sigma} \exp\left(-\dfrac{x^2}{2\sigma^2}\right) \mathrm{d}x = .9973.$

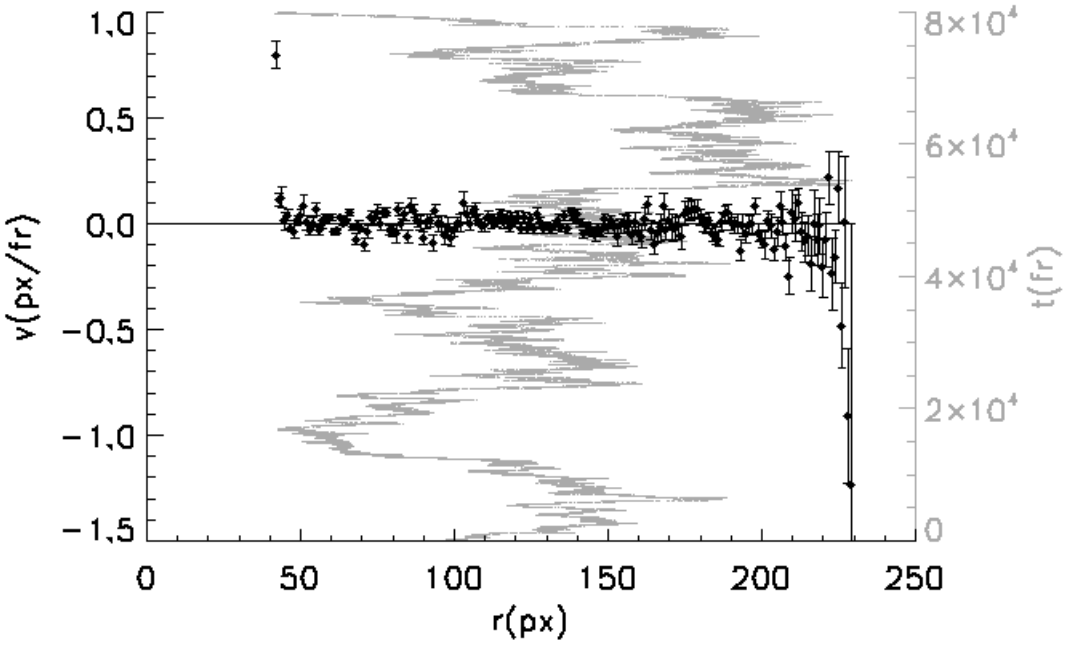

Figure 2.9: Calculated drift velocity from a simulation of random walk with parameters of a typical experiment. The gray curve is the pair separation r as a function of time t. The black points are measured drift velocity v at different separation r. The diffusion coefficient was $D_{\text{eff}} = .18$ px^2/fr. The position of particles was simulated for 80000 fr, corresponding to $\sim$45 min of experiment observation with video rate 30 fr/s.

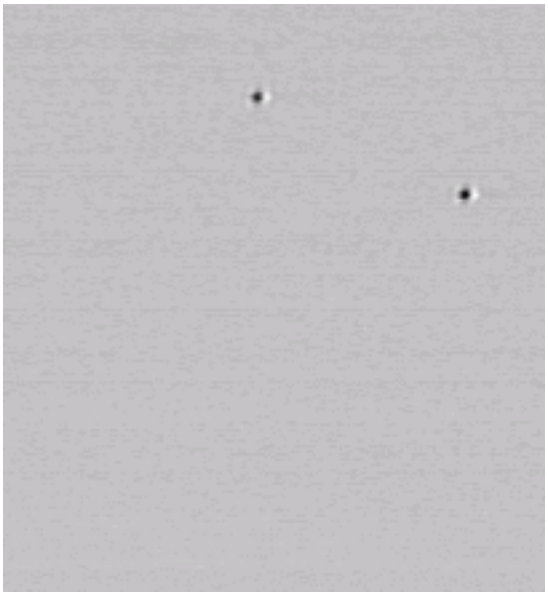

Figure 2.10: Optical microscope image of two polystyrene particles at a water-air interface. The particle diameter is 1.7 μm. The objective used was 20×, corresponding a magnification of 1.49 px/μm. Data label: 092807[5].

2.6 Result for two isolated particles

It turned out that isolated pairs of particles do not show any measurable long-range interaction. Figure 2.10 shows an image of two polystyrene particles at a water-air interface. Figure 2.11 shows a typical distribution of $v(r)$ for a particular separation r. The black curve is the measured distribution with kernel smoothing [75], which shows an agreement with Gaussian distribution (blue curve). The measured interaction for this pair is shown in Figure 2.12. The measured effective diffusion coefficient is shown in Figure 2.13, which has no significant dependence on pair separation r. The interaction force $f(r)$ is converted from the relative drift velocity $v(r)$ according to $f(r) = \dfrac{k_{\mathrm{B}}T}{D_{\mathrm{eff}}} v(r)$. We use the measured effective diffusion coefficient D_{eff} (Figure 2.13) and $T = 298$ K to convert v to f. The measured force between particles is fluctuating around zero within our resolution, which is usually a few femtonewton's.

[5]A folder named as the data label can be found in the author's directory on servers Narmada2 and Walnut.

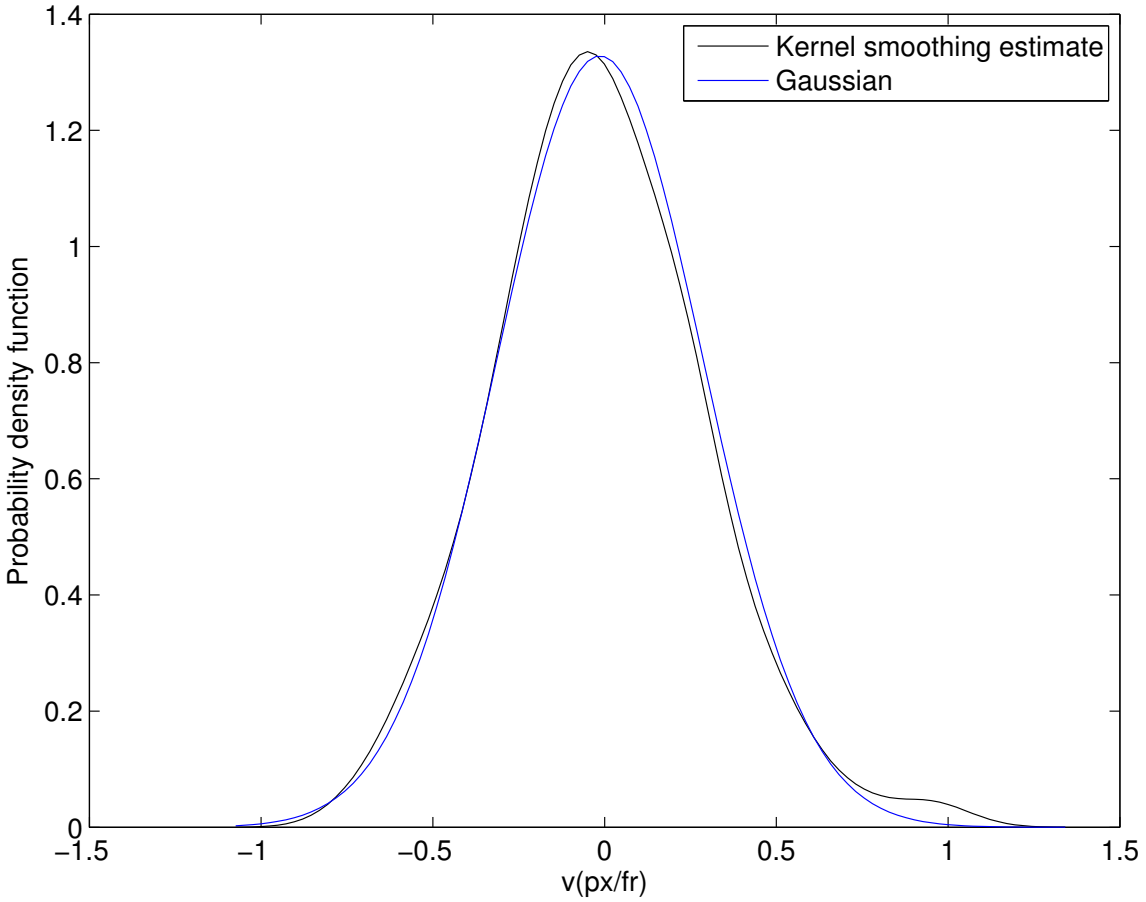

Figure 2.11: Probability density function of $v(r)$ at $r = 26$ px for particles in Figure 2.10. The black curve is the kernel smoothing density estimation. The blue curve is the probability density function for Gaussian distribution with mean $\langle v \rangle$ and standard deviation σ_v. Data label: 092807.

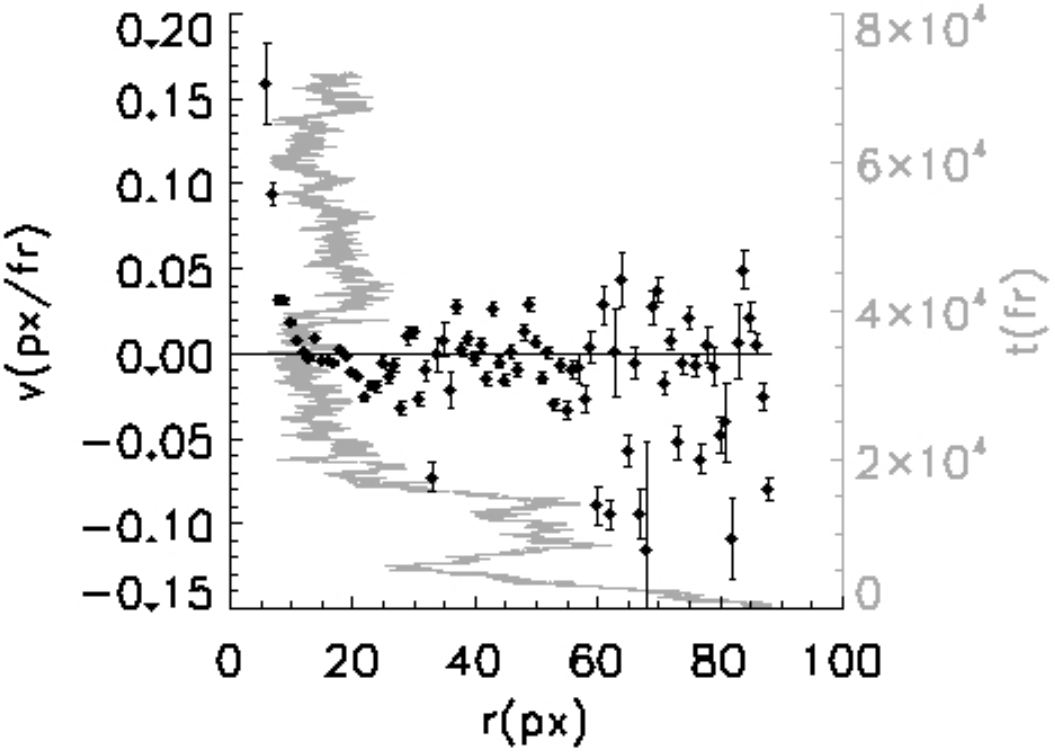

Figure 2.12: Interaction between two particles at a water-air interface. The frame rate is 30 fr/s. The gray curve is the pair separation r as a function of time t. The black points are measured drift velocity v at different separation r. The particle diameter is 1.7 μm. The objective used was 20×, corresponding to a magnification of 1.49 px/μm. $D_{\text{eff}} = .18$ px^2/fr. The conversion factor from drift velocity to interaction force is 35 fN·fr/px. Data label: 092807.

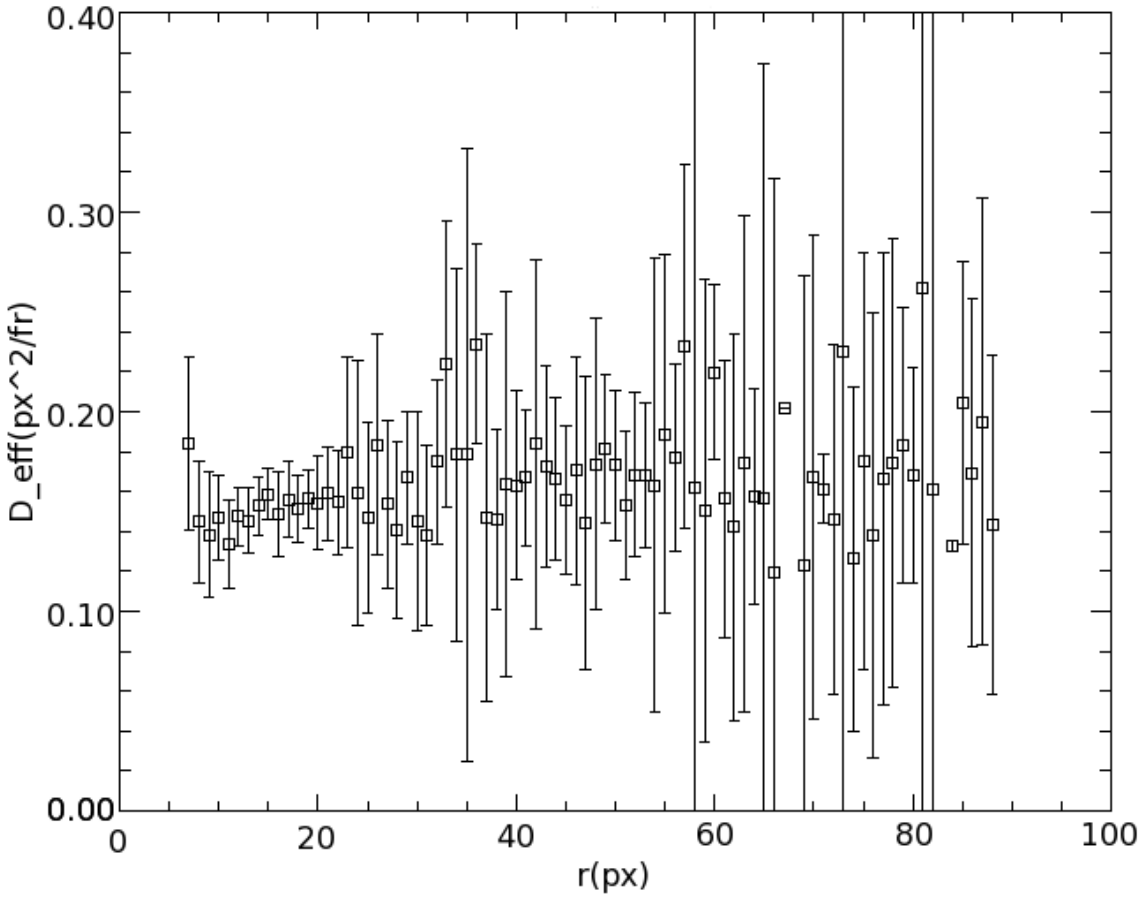

Figure 2.13: Measured effective diffusion coefficient. The frame rate is 30 fr/s. The particle diameter is 1.7 μm. The objective used was 20×, corresponding to a magnification of 1.49 px/μm. Data label: 092807.

Figure 2.14-2.21 shows measured pair interaction between polystyrene particles (diameter 1.7 μm) at interfaces of water and silicone oil from 5 different samples. .01 M NaCl was added in some samples in order to reduce the screening length and thus the electrostatic repulsion between particles. In some cases, the force is not zero within the error bars, but the deviation from zero is not systematic. Moreover, we note that the estimated error bars should correspond to the one-sigma error, and that approximately 1/3 of the data should lie more than 1 sigma from the true result. The result shows no measurable interaction force given the error bars.

We also added nanoparticles in some samples to see if the nanoparticles affect the interaction among micron-sized PS beads (Figure 2.22). We used 3-nm-diameter gold nanoparticles stabilized with (1-mercaptoundec-11-yl)tetra(ethylene glycol) (Au-TEG), which are known to adsorb at a water-oil interface [70]. The relative drift velocity data do not show significant interaction among PS beads.

We also measured the interactions between nearly isolated pairs, *i.e.*, when other particles were further away than the pair separation. Figure 2.23-2.28 shows more data on polystyrene beads at water-air interfaces. Particularly for the experiment of Figure 2.23, the pair of particles being examined was not perfectly isolated. There were other monomers and clusters of particles at about 160 px away. Therefore, the measured interaction between this pair may be affected at the range of 160 px. We stopped the data acquisition when the separation of the pair approaches 160 px. The drift velocity data do not show any significant interaction. The measured interaction in the shorter range was not affected by other particles within our resolution.

To test whether the contact-line pinning affects the interaction, Figure 2.29 shows an image of two microdroplets of 2,2,3,3,4,4,5,5-octafluoropentyl acrylate at a water-air interface. No surfactant was added. Because the "particles" in this experiment are liquid, the three-phase contact line cannot be pinned. The size of oil droplets was not well controlled. We determine from the image that the diameter of droplets

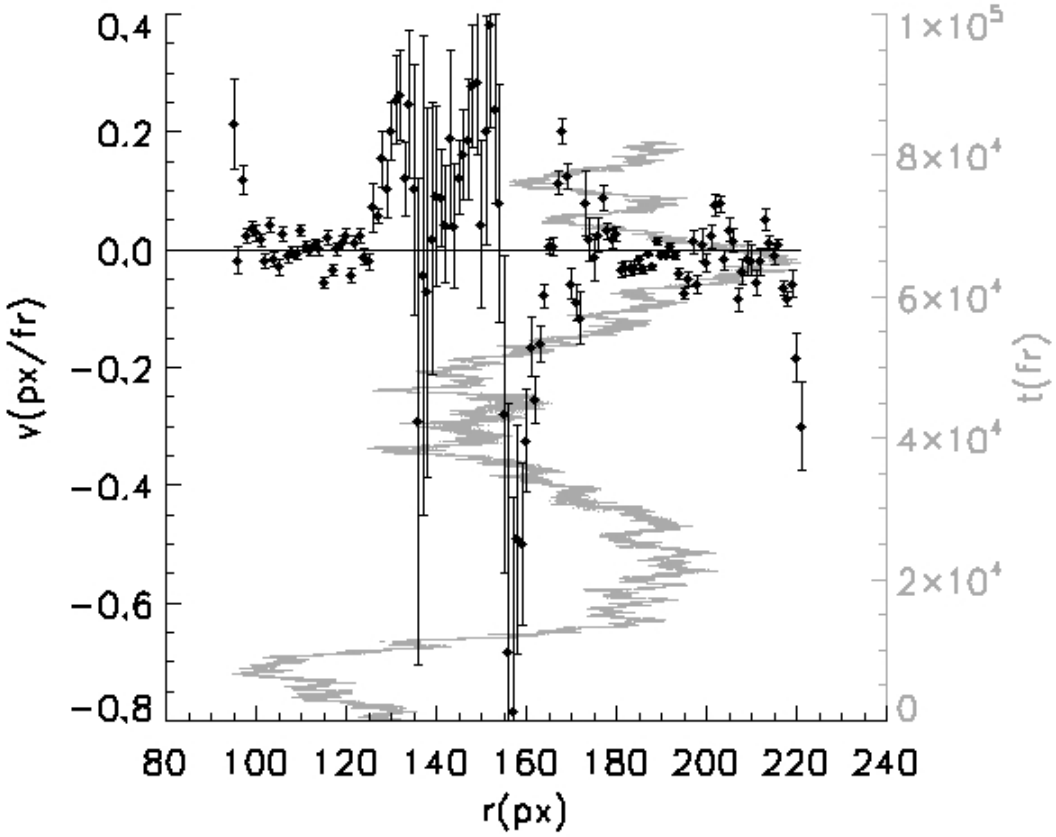

Figure 2.14: PS beads at an interface of water and silicone oil. The frame rate is 30 fr/s. The gray curve is the pair separation r as a function of time t. The black points are measured drift velocity v at different separation r. The particle diameter is 1.7 μm. The objective used was 63× with an additional magnification of 1.6, corresponding 8.1 px/μm. $D_{\text{eff}} = .92$ px^2/fr. The conversion factor from drift velocity to interaction force is 36 fN·fr/px. Data label: 120106.

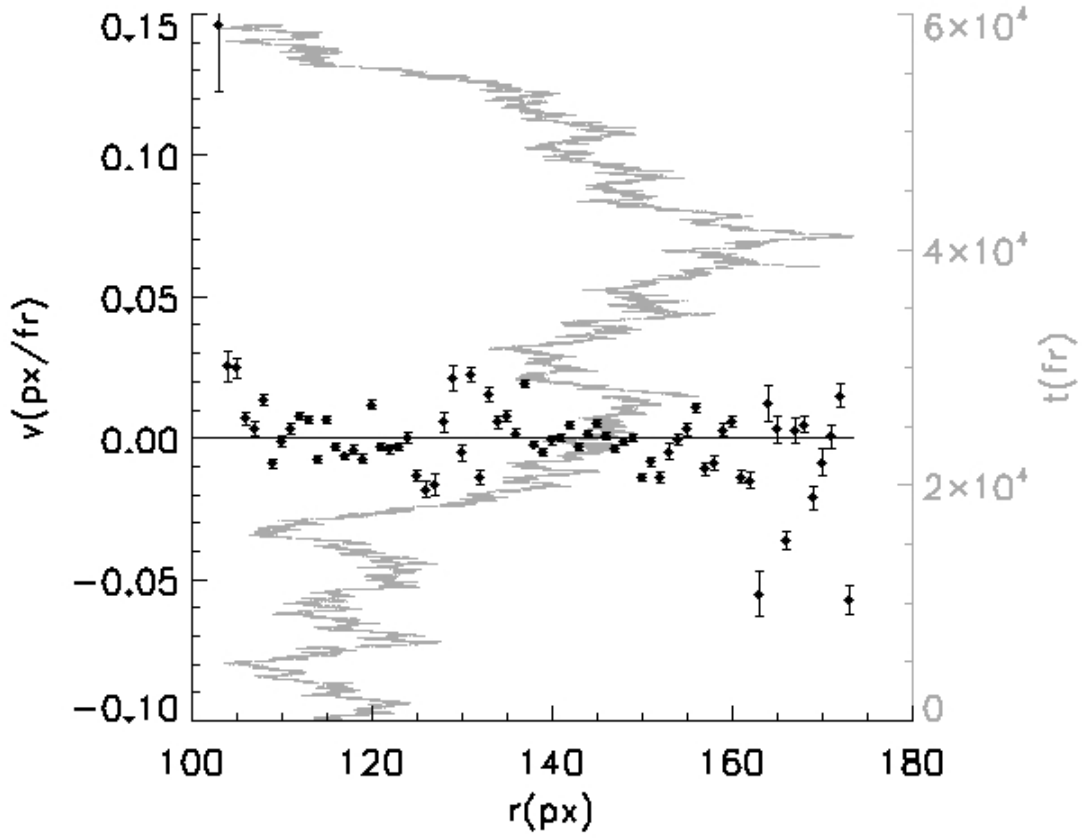

Figure 2.15: PS beads at an interface of water and silicone oil. The frame rate is 30 fr/s. The gray curve is the pair separation r as a function of time t. The black points are measured drift velocity v at different separation r. The particle diameter is 1.7 μm. The objective used was 63× with an additional magnification of 1.6, corresponding 8.1 px/μm. $D_{\text{eff}} = .22$ px^2/fr. The conversion factor from drift velocity to interaction force is 151 fN·fr/px. Data label: 012207.

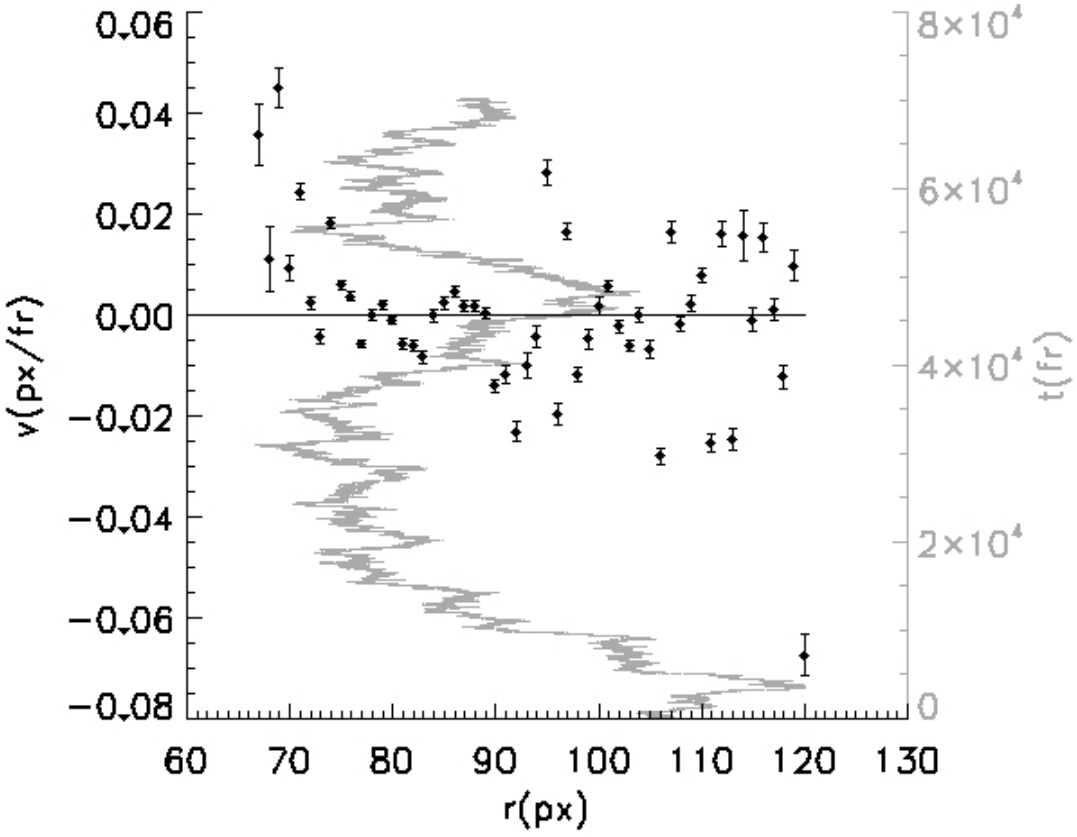

Figure 2.16: PS beads at an interface of water (.01 M NaCl) and silicone oil. The frame rate is 30 fr/s. The gray curve is the pair separation r as a function of time t. The black points are measured drift velocity v at different separation r. The particle diameter is 1.7 μm. The objective used was 63×, corresponding to a magnification of 5.2 px/μm. $D_{\text{eff}} = .22$ px^2/fr. The conversion factor from drift velocity to interaction force is 97 fN·fr/px. Data label: 020707.

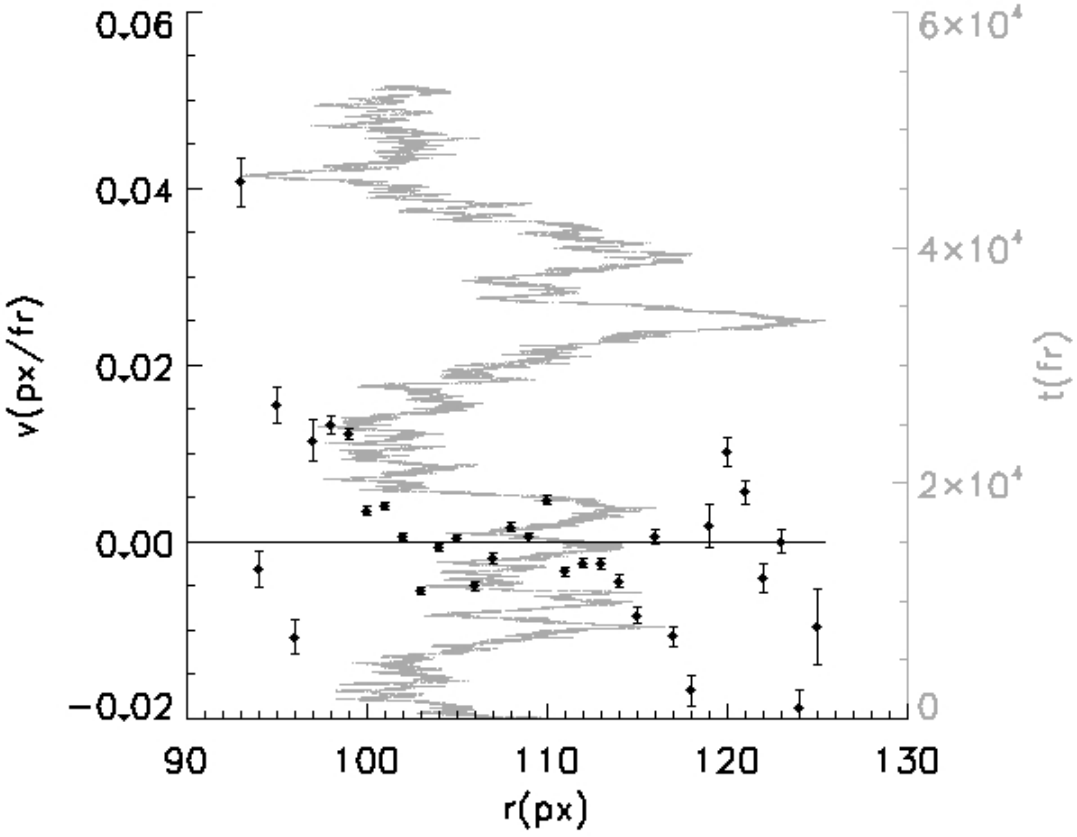

Figure 2.17: PS beads at an interface of water (.01 M NaCl) and silicone oil. The frame rate is 30 fr/s. The gray curve is the pair separation r as a function of time t. The black points are measured drift velocity v at different separation r. The particle diameter is 1.7 μm. The objective used was 63×, corresponding to a magnification of 5.2 px/μm. $D_{\text{eff}} = .16$ px^2/fr. The conversion factor from drift velocity to interaction force is 134 fN·fr/px. Data label: 020807_3.

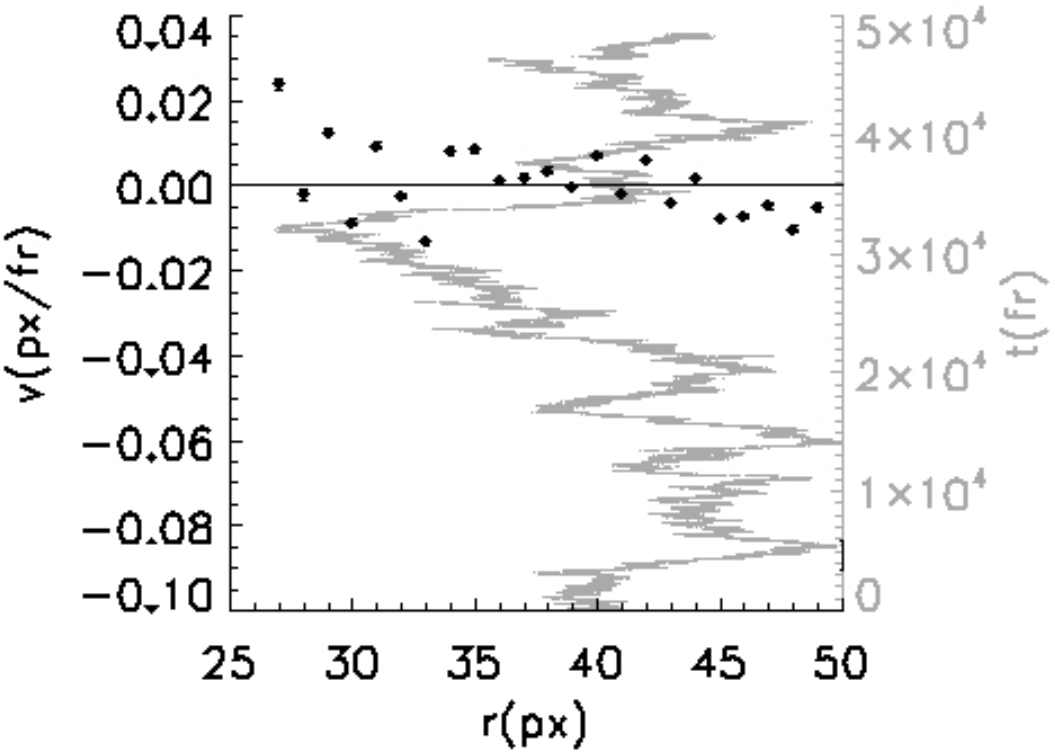

Figure 2.18: PS beads at an interface of water (.01 M NaCl) and silicone oil. The frame rate is 30 fr/s. The gray curve is the pair separation r as a function of time t. The black points are measured drift velocity v at different separation r. The particle diameter is 1.7 μm. The objective used was 63×, corresponding to a magnification of 5.2 px/μm. $D_{\text{eff}} = .17$ px^2/fr. The conversion factor from drift velocity to interaction force is 126 fN·fr/px. Data label: 020807_4.

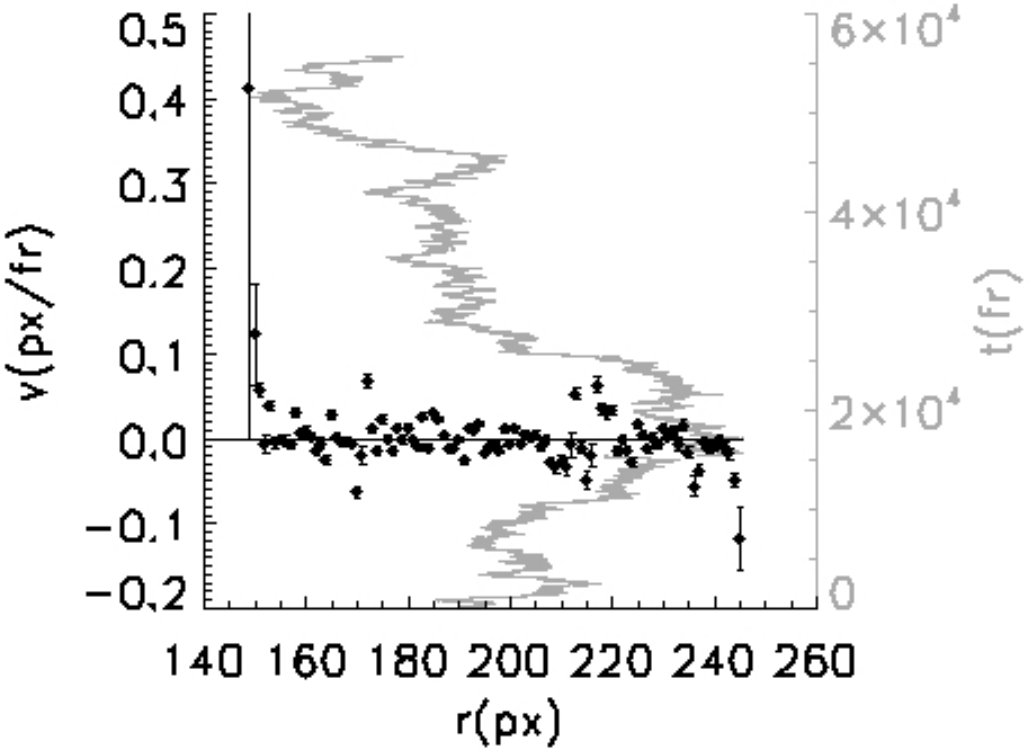

Figure 2.19: PS beads at an interface of water (.01 M NaCl) and silicone oil. The frame rate is 30 fr/s. The gray curve is the pair separation r as a function of time t. The black points are measured drift velocity v at different separation r. The particle diameter is 1.7 μm. The objective used was 63× with an additional magnification of 1.6, corresponding 8.1 px/μm. $D_{\text{eff}} = .33$ px^2/fr. The conversion factor from drift velocity to interaction force is 101 fN·fr/px. Data label: 021107/pair1.

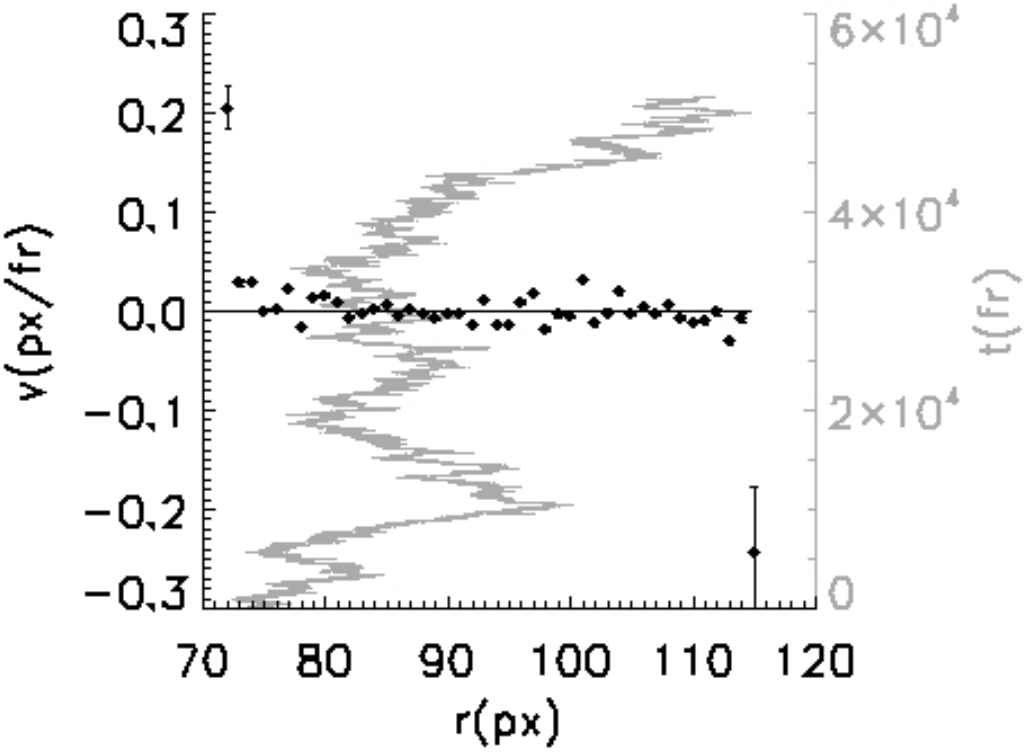

Figure 2.20: PS beads at an interface of water (.01 M NaCl) and silicone oil. The frame rate is 30 fr/s. The gray curve is the pair separation r as a function of time t. The black points are measured drift velocity v at different separation r. The particle diameter is 1.7 μm. The objective used was 63×, corresponding to a magnification of 5.2 px/μm. $D_{\text{eff}} = .24$ px^2/fr. The conversion factor from drift velocity to interaction force is 89 fN·fr/px. Data label: 021107/pair2.

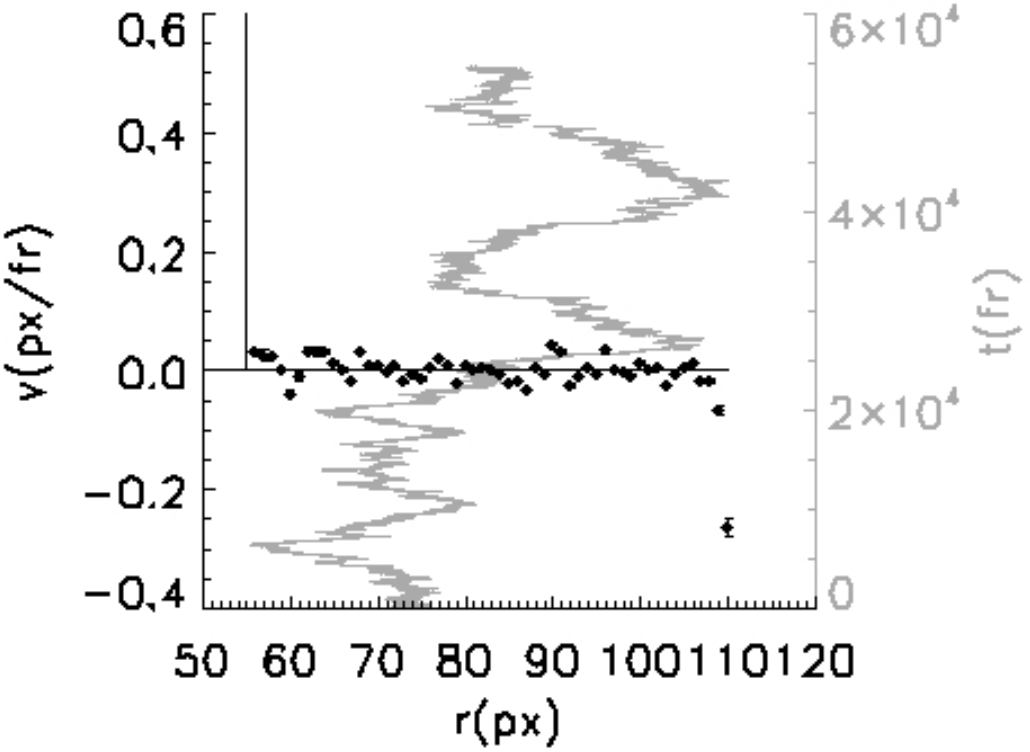

Figure 2.21: PS beads at an interface of water (.01 M NaCl) and silicone oil. The frame rate is 30 fr/s. The gray curve is the pair separation r as a function of time t. The black points are measured drift velocity v at different separation r. The particle diameter is 1.7 μm. The objective used was 63×, corresponding to a magnification of 5.2 px/μm. $D_{\text{eff}} = .30$ px^2/fr. The conversion factor from drift velocity to interaction force is 71 fN·fr/px. Data label: 021107/pair3.

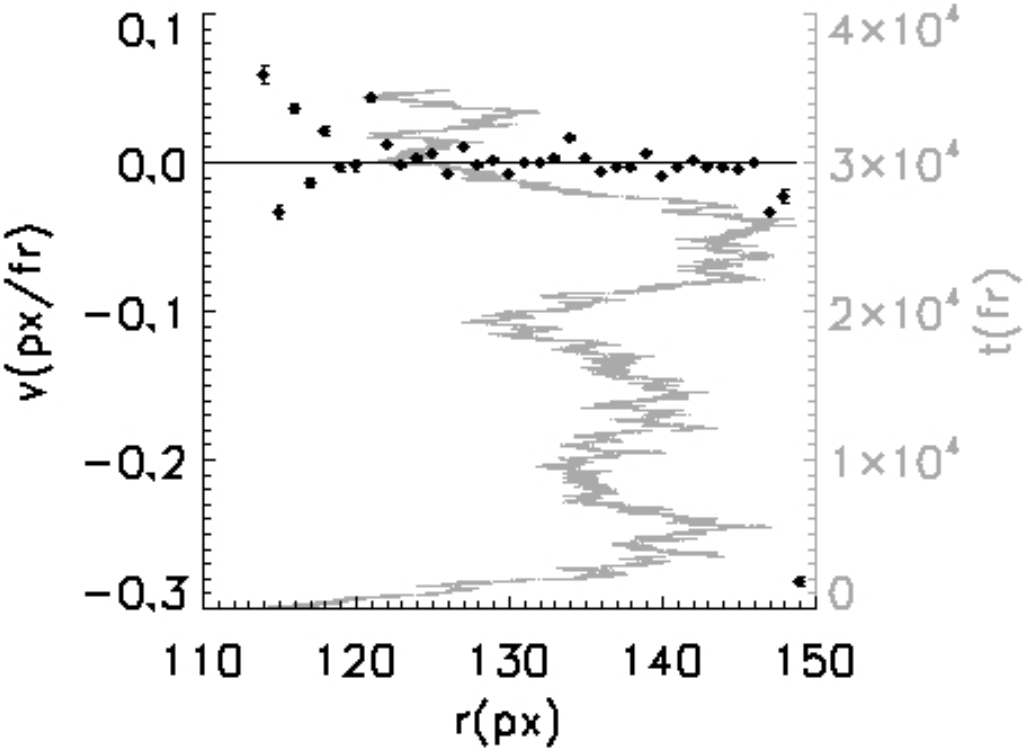

Figure 2.22: PS beads at an interface of water (.01 M NaCl, Au-TEG) and silicone oil. The frame rate is 30 fr/s. The gray curve is the pair separation r as a function of time t. The black points are measured drift velocity v at different separation r. The particle diameter is 1.7 μm. The objective used was 63× with an additional magnification of 1.6, corresponding to 8.1 px/μm. $D_{\text{eff}} = .19$ px^2/fr. The conversion factor from drift velocity to interaction force is 167 fN·fr/px. Data label: 032607/pair3.

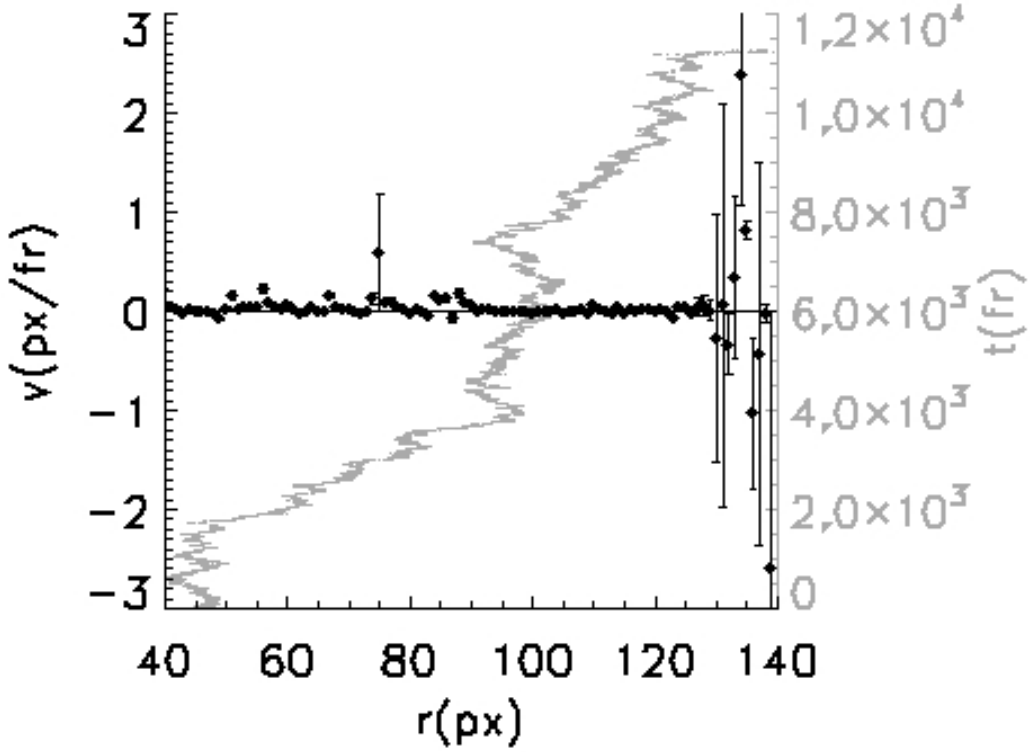

Figure 2.23: PS beads at a water-air interface with other beads approximately 160 px away. The frame rate is 30 fr/s. The gray curve is the pair separation r as a function of time t. The black points are measured drift velocity v at different separation r. The particle diameter is 1.7 μm. The objective used was 20× with an additional magnification of 1.6, corresponding to 2.35 px/μm. The conversion factor from drift velocity to interaction force is 33 fN·fr/px. Data label: 091507/pair1.

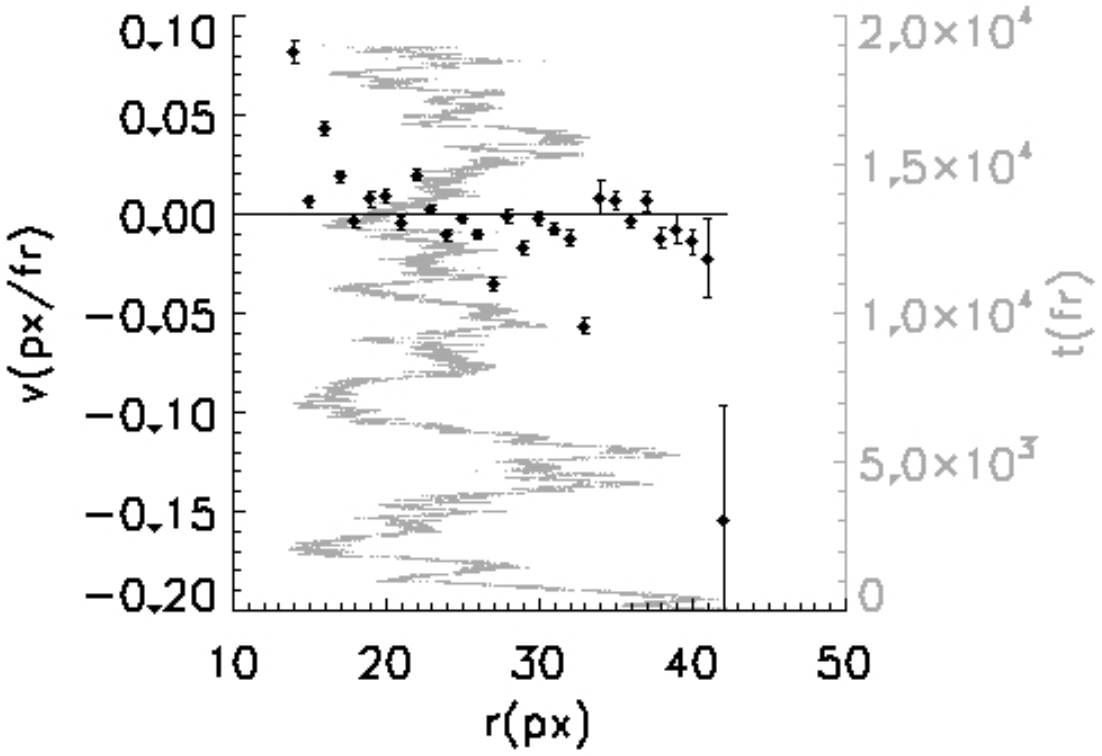

Figure 2.24: PS beads at a water-air interface. The frame rate is 30 fr/s. The gray curve is the pair separation r as a function of time t. The black points are measured drift velocity v at different separation r. The particle diameter is 1.7 μm. The objective used was 20× with an additional magnification of 1.6, corresponding to 2.35 px/μm. $D_{\text{eff}} = .29$ px^2/fr. The conversion factor from drift velocity to interaction force is 33 fN·fr/px. Data label: 091507/pair2.

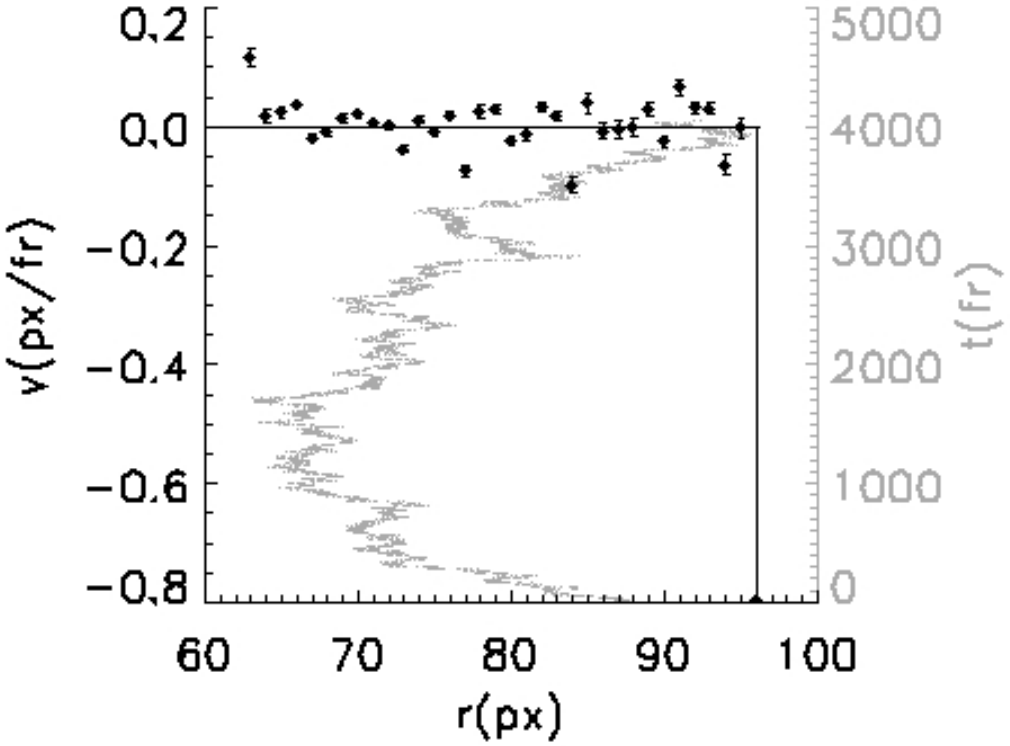

Figure 2.25: PS beads at a water-air interface. The frame rate is 30 fr/s. The gray curve is the pair separation r as a function of time t. The black points are measured drift velocity v at different separation r. The particle diameter is 1.7 μm. The objective used was 20× with an additional magnification of 1.6, corresponding to 2.35 px/μm. $D_{\text{eff}} = .28$ px^2/fr. The conversion factor from drift velocity to interaction force is 35 fN·fr/px. Data label: 091507/pair3.

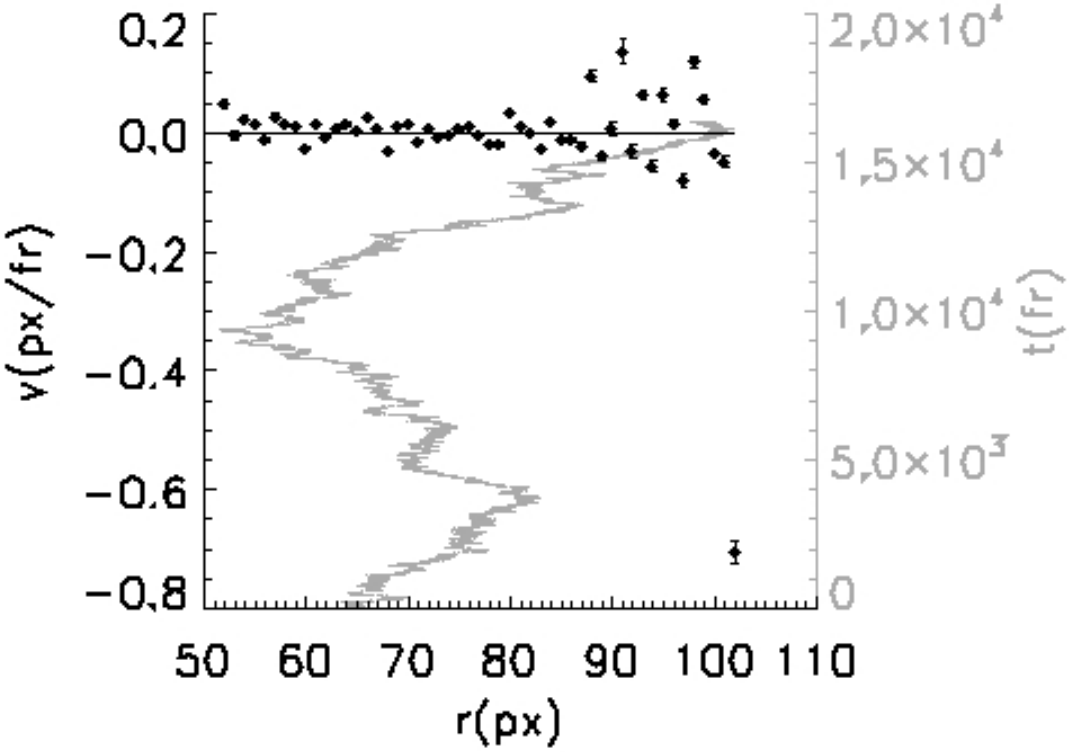

Figure 2.26: PS beads at a water-air interface. The frame rate is 30 fr/s. The gray curve is the pair separation r as a function of time t. The black points are measured drift velocity v at different separation r. The particle diameter is 1.7 μm. The objective used was 20× with an additional magnification of .63, corresponding to .96 px/μm. $D_{\text{eff}} = .25$ px^2/fr. The conversion factor from drift velocity to interaction force is 16 fN·fr/px. Data label: 091707.

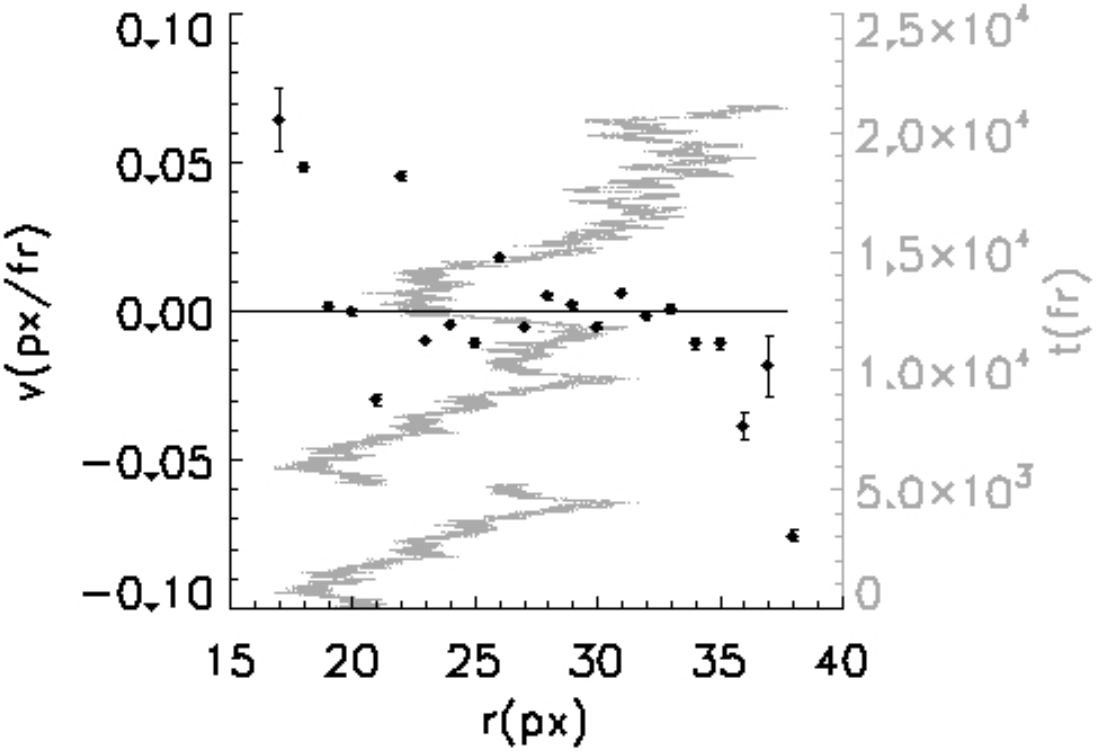

Figure 2.27: PS beads at a water-air interface. The frame rate is 30 fr/s. The gray curve is the pair separation r as a function of time t. The black points are measured drift velocity v at different separation r. The particle diameter is 1.7 μm. The objective used was 20×, corresponding to a magnification of 1.49 px/μm. $D_{\text{eff}} = .21$ px^2/fr. The conversion factor from drift velocity to interaction force is 29 fN·fr/px. Data label: 092507/pair1.

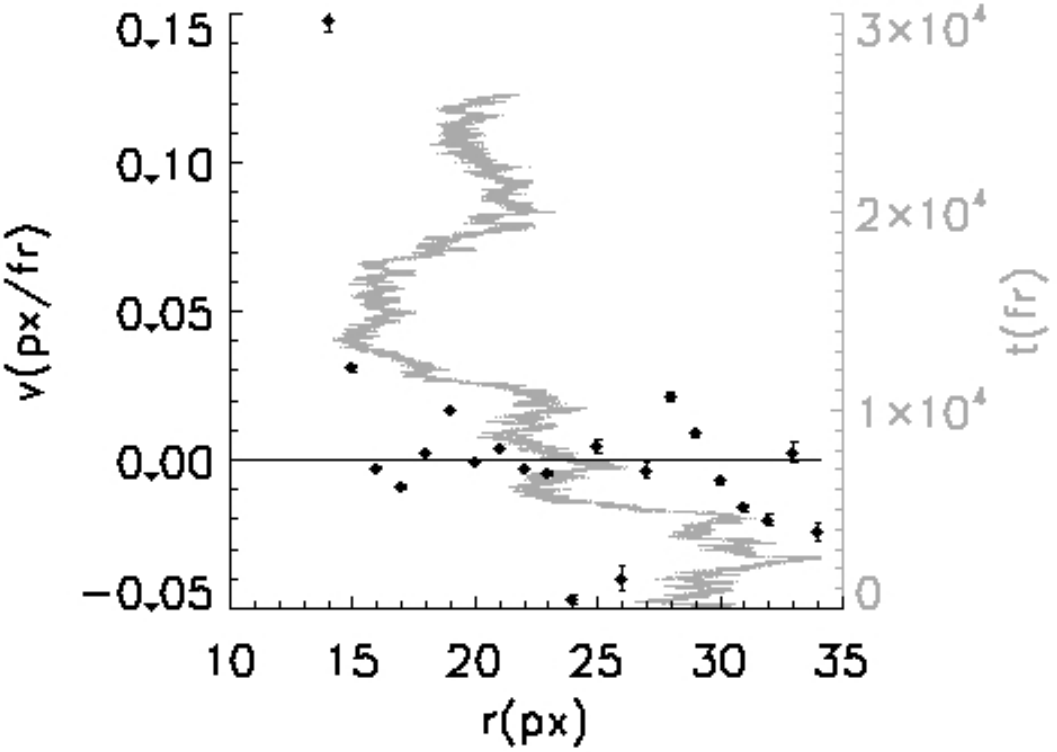

Figure 2.28: PS beads at a water-air interface. The frame rate is 30 fr/s. The gray curve is the pair separation r as a function of time t. The black points are measured drift velocity v at different separation r. The particle diameter is 1.7 μm. The objective used was 20×, corresponding to a magnification of 1.49 px/μm. $D_{\text{eff}} = .20$ px^2/fr. The conversion factor from drift velocity to interaction force is 31 fN·fr/px. Data label: 092507/pair2.

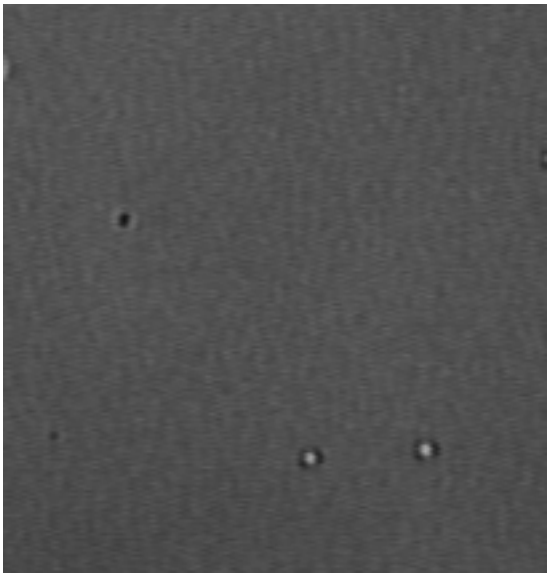

Figure 2.29: Optical microscope image of two microdroplets of 2,2,3,3,4,4,5,5-octafluoropentyl acrylate at a water-air interface. The objective used was 20×, corresponding to a magnification of 1.49 px/μm. The size of droplets indicated in the image is about 2 μm. Data label: 110607.

is about 2 μm. The measured interaction for this pair is shown in Figure 2.30. Figure 2.31-2.34 shows more measured interaction between microdroplets of different oils at water-air interfaces. The imaging of microdroplets are more unstable compared to solid particles. The data corresponding to separation $r > 150$ px in Figure 2.32 and $r > 60$ px in Figure 2.33 were due to artifacts of imaging and droplet tracking. In some experiments, a third droplet could diffuse close to the pair being observed. For example in Figure 2.34, about 30000 consecutive frames were skipped because of a third droplet, after which the third droplet diffused further away from the pair.

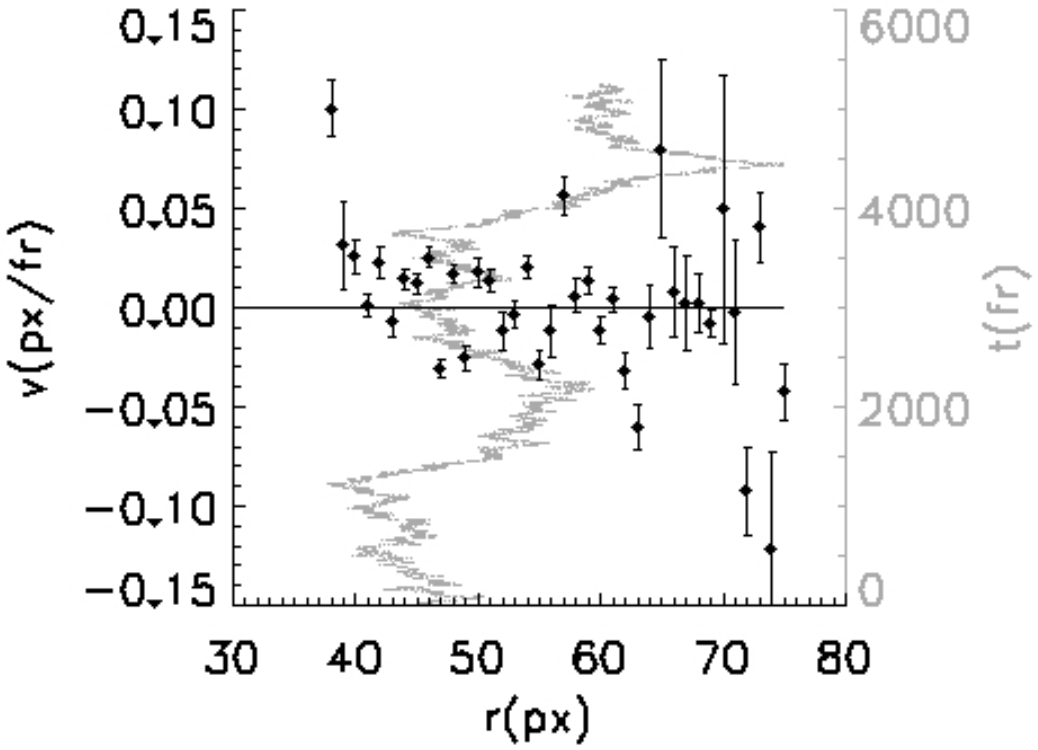

Figure 2.30: Interaction between two microdroplets of 2,2,3,3,4,4,5,5-octafluoropentyl acrylate at a water-air interface. The frame rate is 30 fr/s. The gray curve is the pair separation r as a function of time t. The black points are measured drift velocity v at different separation r. The objective used was 20×, corresponding to a magnification of 1.49 px/μm. $D_{\text{eff}} = .31$ px^2/fr. The conversion factor from drift velocity to interaction force is 20 fN·fr/px. Data label: 110607.

To summarize, we measured the relative drift velocity and thus the interaction force between two solid particles or two microdroplets at various fluid interfaces. Isolated pairs do not show significant interaction in any of the systems investigated. The formation of a dimer from an isolated pair was never observed in our experiments.

2.7 Result for two particles with other particles nearby

When a pair was investigated with one or more particles nearby, the measurement showed *effective* interaction which could be either attractive or repulsive and which

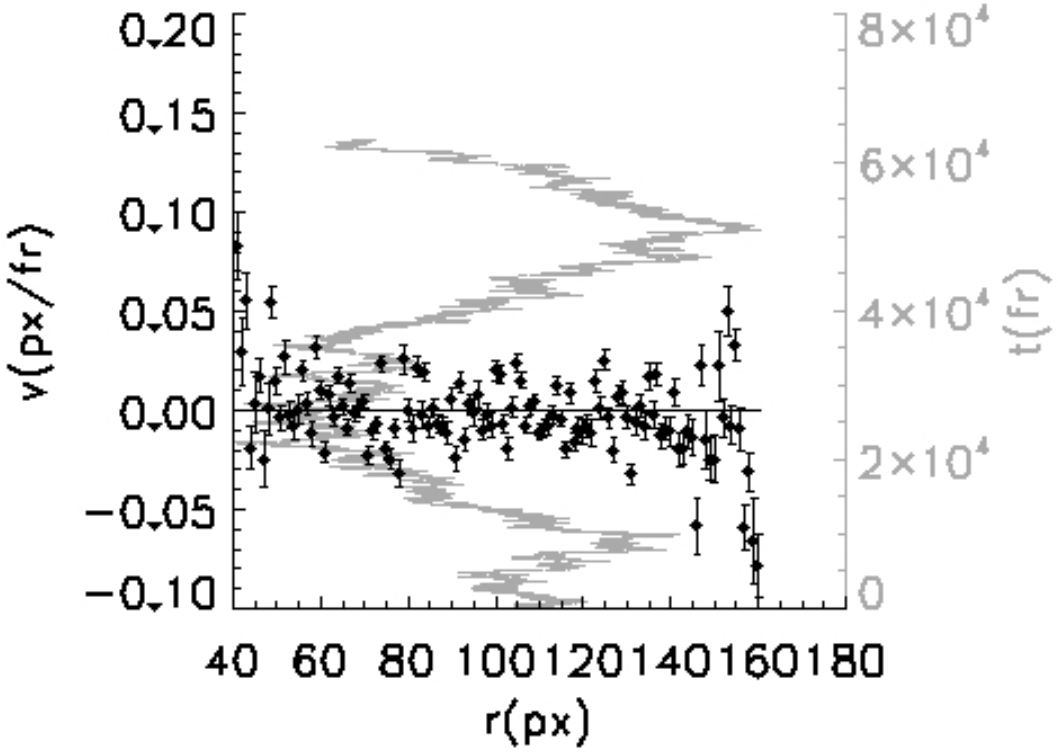

Figure 2.31: Interaction between two microdroplets of 1,1,1-trifluoroheptan-2-ol at a water-air interface. The frame rate is 30 fr/s. The gray curve is the pair separation r as a function of time t. The black points are measured drift velocity v at different separation r. The objective used was 20×, corresponding to a magnification of 1.49 px/μm. $D_{\text{eff}} = .11$ px^2/fr. The conversion factor from drift velocity to interaction force is 56 fN·fr/px. Data label: 121107/pair1.

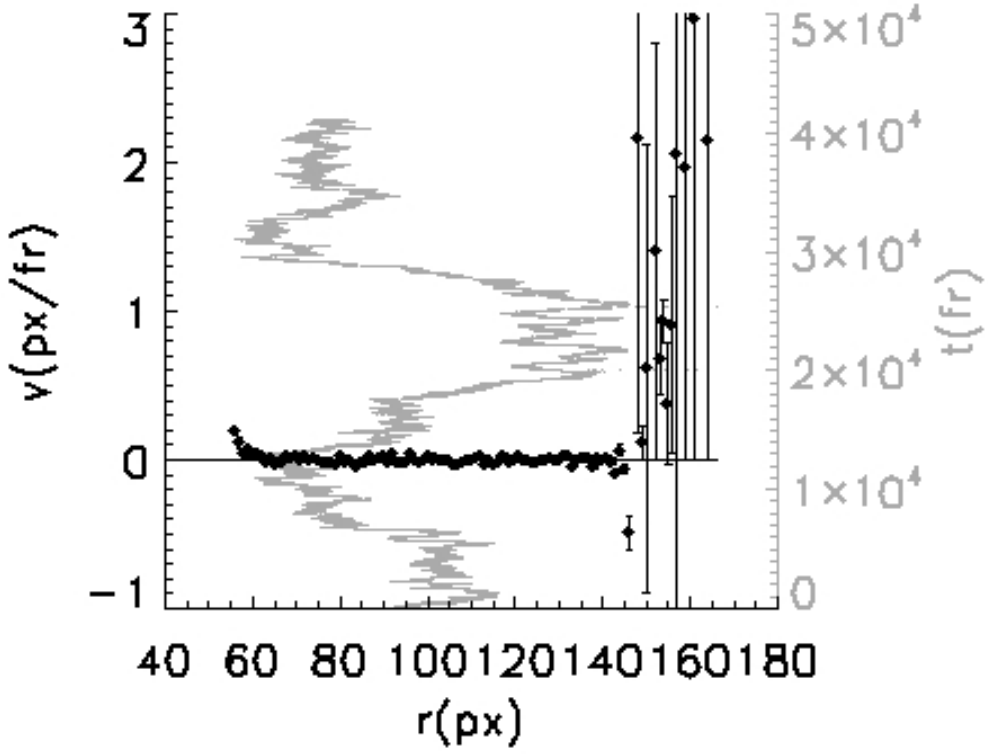

Figure 2.32: Interaction between two microdroplets of 1,1,1-trifluoroheptan-2-ol at a water-air interface. The frame rate is 30 fr/s. The gray curve is the pair separation r as a function of time t. The black points are measured drift velocity v at different separation r. The objective used was 20×, corresponding to a magnification of 1.49 px/μm. $D_{\text{eff}} = .125$ px^2/fr. The conversion factor from drift velocity to interaction force is 49 fN·fr/px. The data corresponding to separation $r > 150$ px is due to artifacts of imaging and droplet tracking. Data label: 121107/pair2.

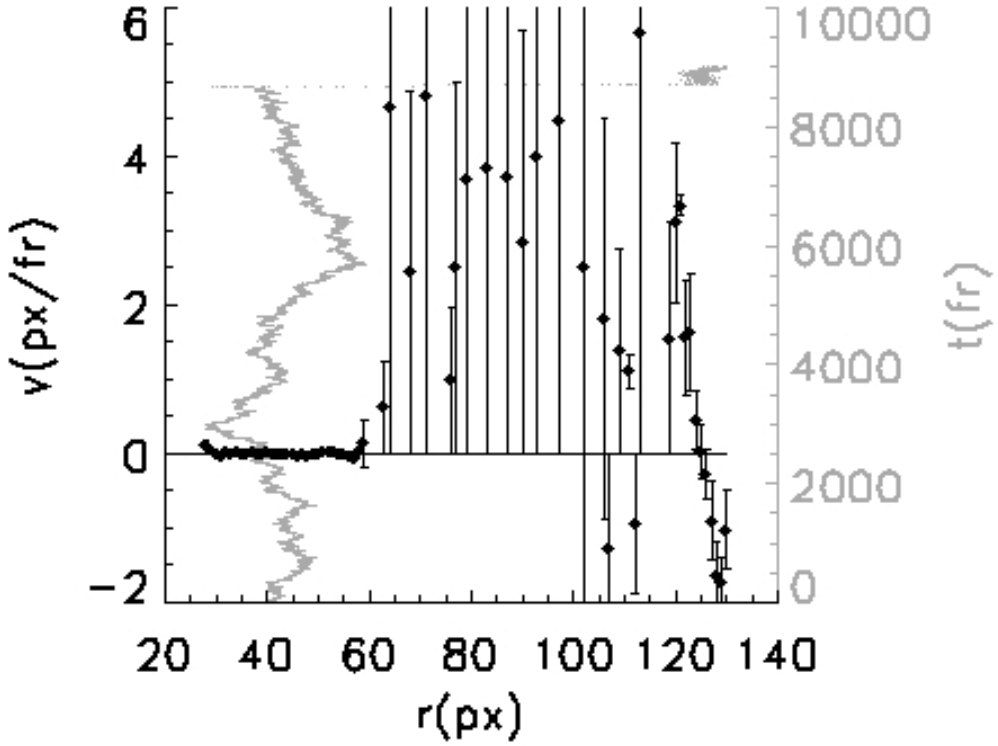

Figure 2.33: Interaction between two microdroplets of decalin at a water-air interface. The frame rate is 30 fr/s. The gray curve is the pair separation r as a function of time t. The black points are measured drift velocity v at different separation r. The objective used was 20×, corresponding a magnification of 1.49 px/μm. The conversion factor from drift velocity to interaction force is 15 fN·fr/px. The data corresponding to $r > 60$ px is due to artifacts of imaging and droplet tracking. Data label: 033108.

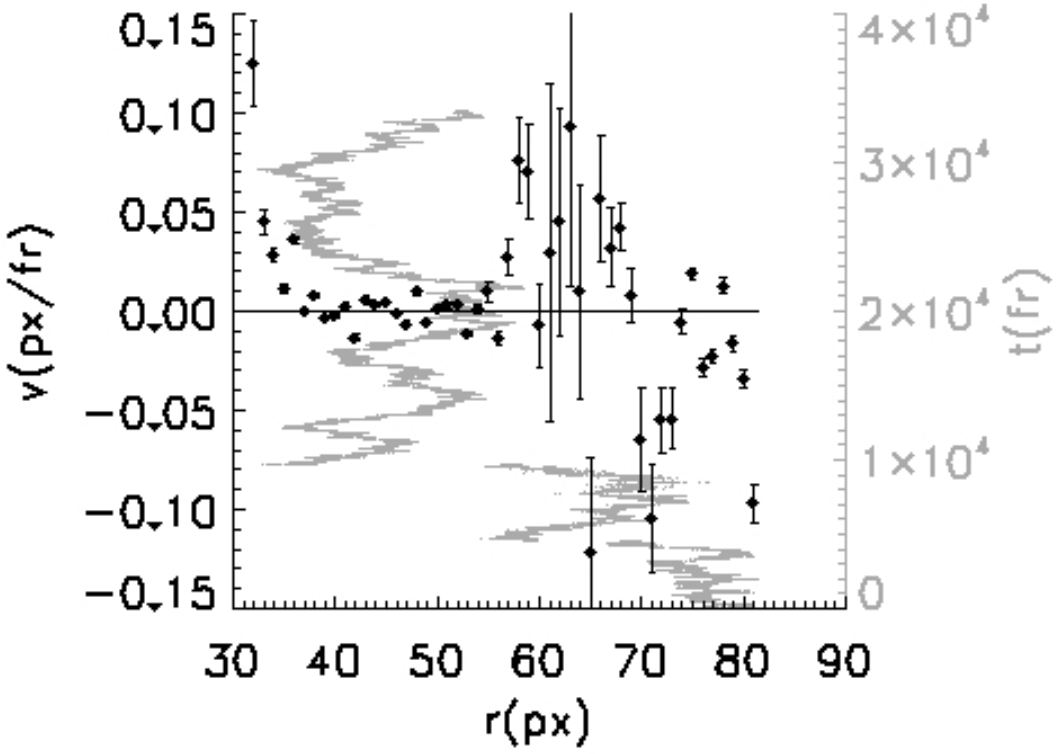

Figure 2.34: Interaction between two microdroplets of decalin at a water-air interface. The frame rate is 30 fr/s. The gray curve is the pair separation r as a function of time t. The black points are measured drift velocity v at different separation r. The objective used was 20×, corresponding a magnification of 1.49 px/μm. $D_{\text{eff}} =$ .40 px^2/fr. The conversion factor from drift velocity to interaction force is 15 fN·fr/px. About 30000 consecutive frames were skipped because of a third droplet nearby (see text). Data label: 042108.

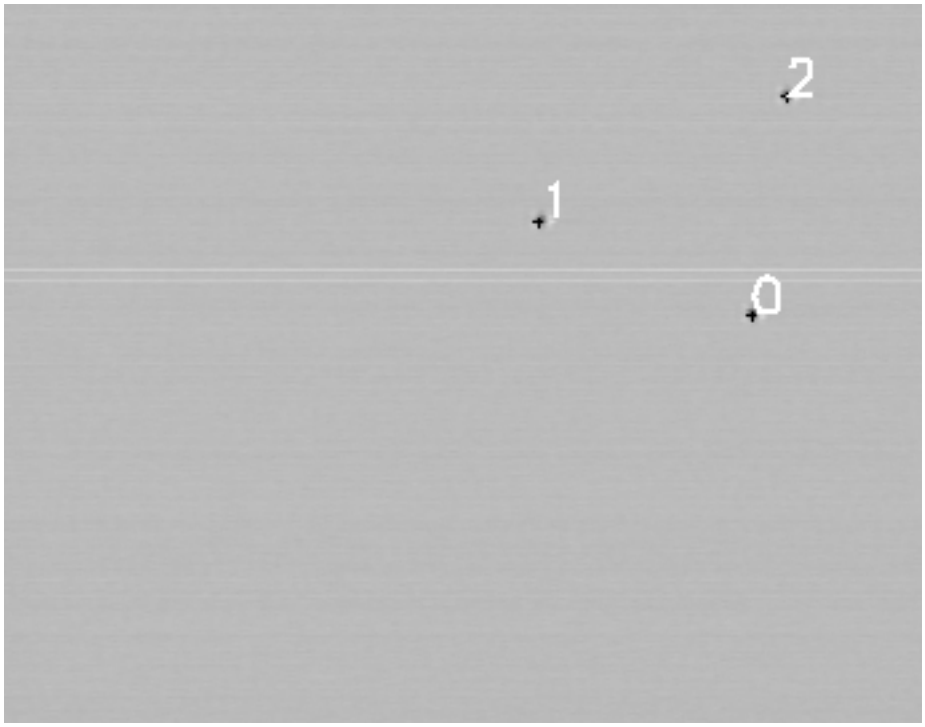

Figure 2.35: Optical microscope image of three polystyrene particles at a water-air interface. The particle diameter is 1.7 μm. The objective used was 20×, corresponding a magnification of 1.49 px/μm. The particles were labeled as 0, 1, and 2. Data label: 092807/three-body.

might be different from the sum of the force between isolated pairs (*i.e.*, might not be pair-wise additive).

Figure 2.35 shows an image with three particles at a water-air interface. The particles were labeled as 0, 1, and 2[6]. We measured the interaction between two of them as shown in Figure 2.36, 2.37, 2.38. In order to compare the interaction between particle 1 and particle 2, and the interaction between particle 0 and particle 2, the data in Figure 2.36 and 2.38 are plotted together in Figure 2.39. The effective forces between those particles are still not measurable.

[6]Figure 2.35 and Figure 2.10 were from the same sample. Particle 0 and particle 1 are the isolated pair shown in Figure 2.10. They were isolated from particle 2 by Brownian motion.

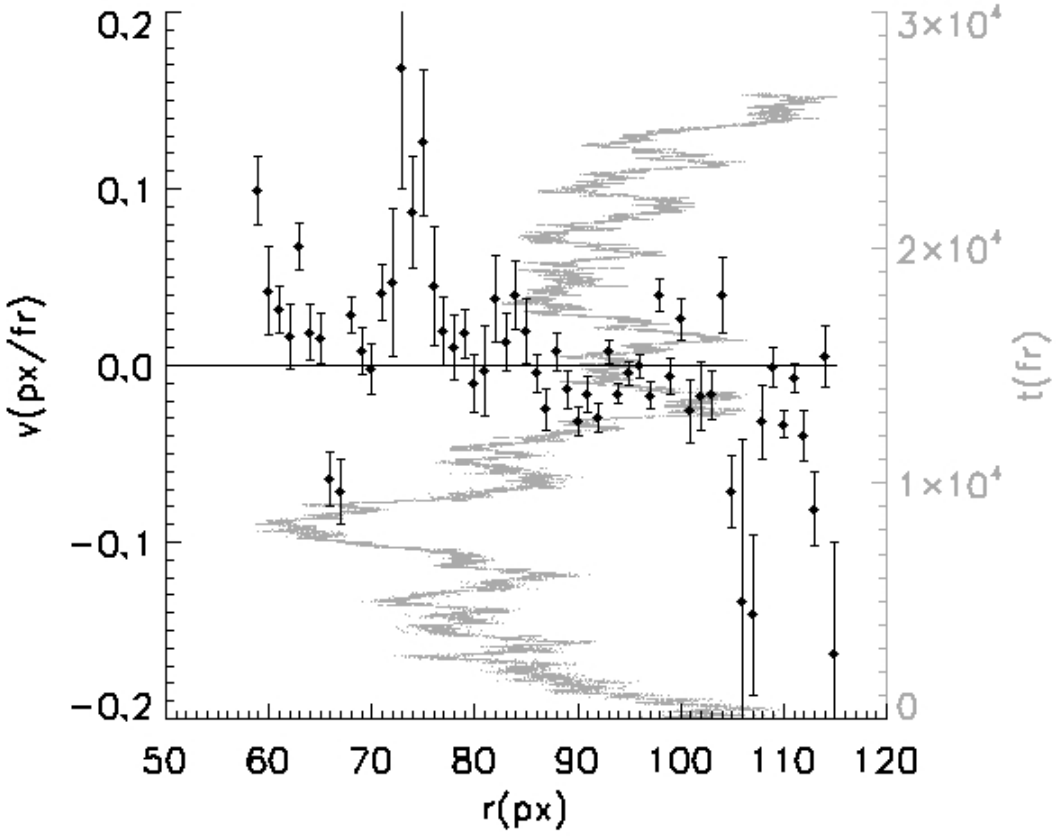

Figure 2.36: Interaction between particle 1 and particle 2 in Figure 2.35. The frame rate is 30 fr/s. The gray curve is the pair separation r as a function of time t. The black points are measured drift velocity v at different separation r. The particle diameter is 1.7 μm. The objective used was 20×, corresponding a magnification of 1.49 px/μm. The conversion factor from drift velocity to interaction force is 20 fN·fr/px (see Figure 2.37). Data label: 092807.

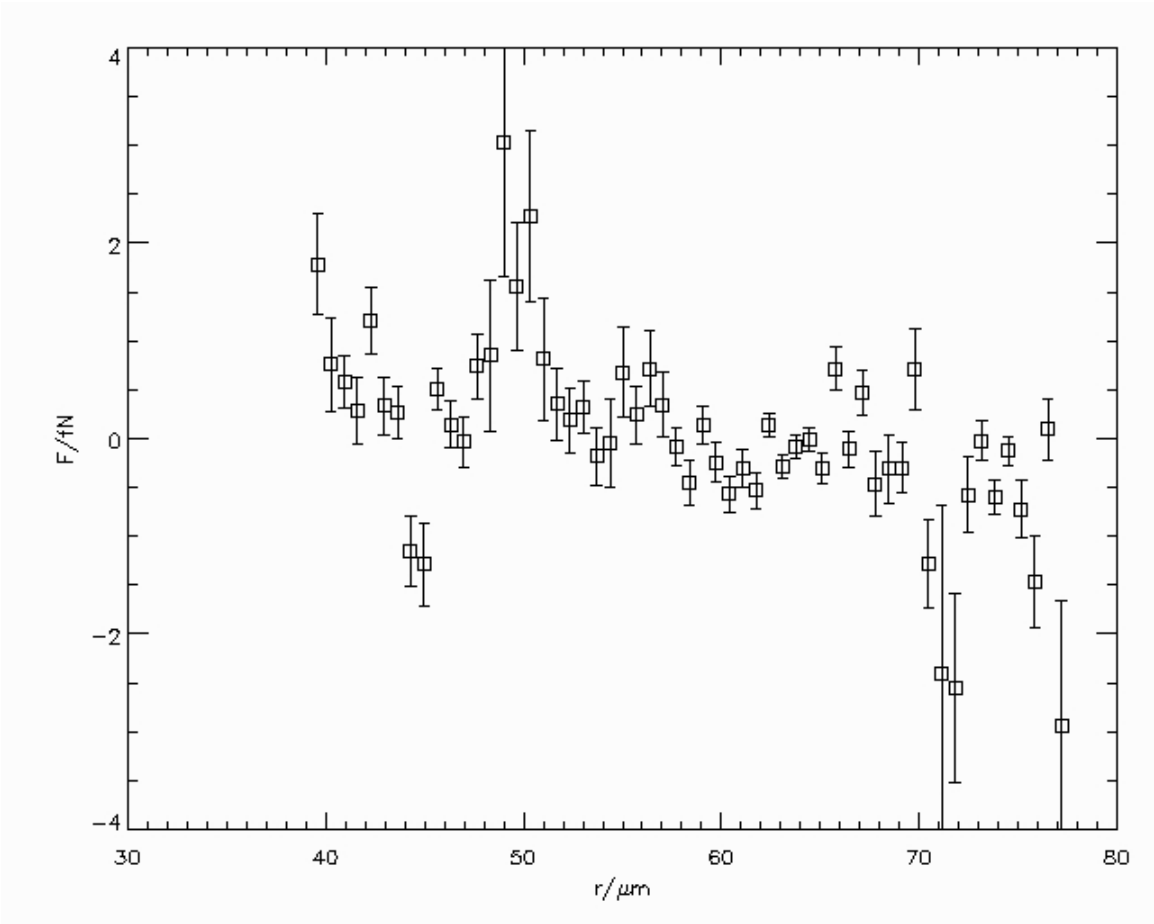

Figure 2.37: Interaction force between particle 1 and particle 2 in Figure 2.35.

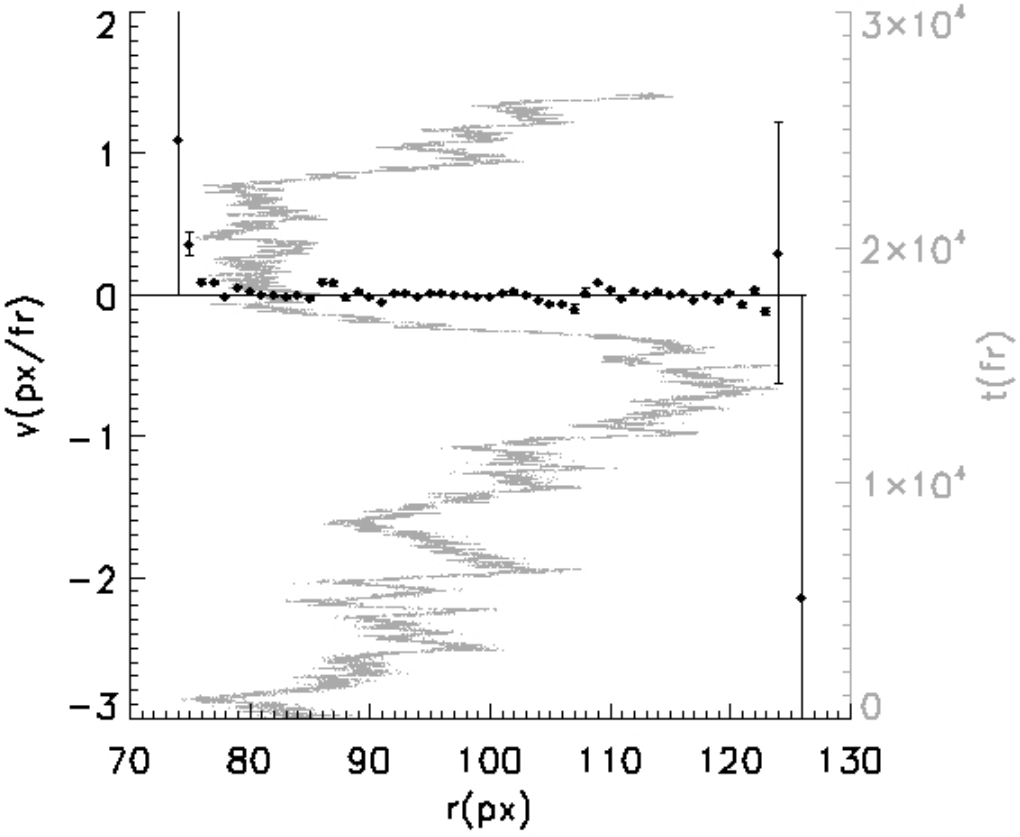

Figure 2.38: Interaction between particle 0 and particle 2 in Figure 2.35. The frame rate is 30 fr/s. The gray curve is the pair separation r as a function of time t. The black points are measured drift velocity v at different separation r. The particle diameter is 1.7 μm. The objective used was 20×, corresponding a magnification of 1.49 px/μm. The conversion factor from drift velocity to interaction force is 20 fN·fr/px. Data label: 092807.

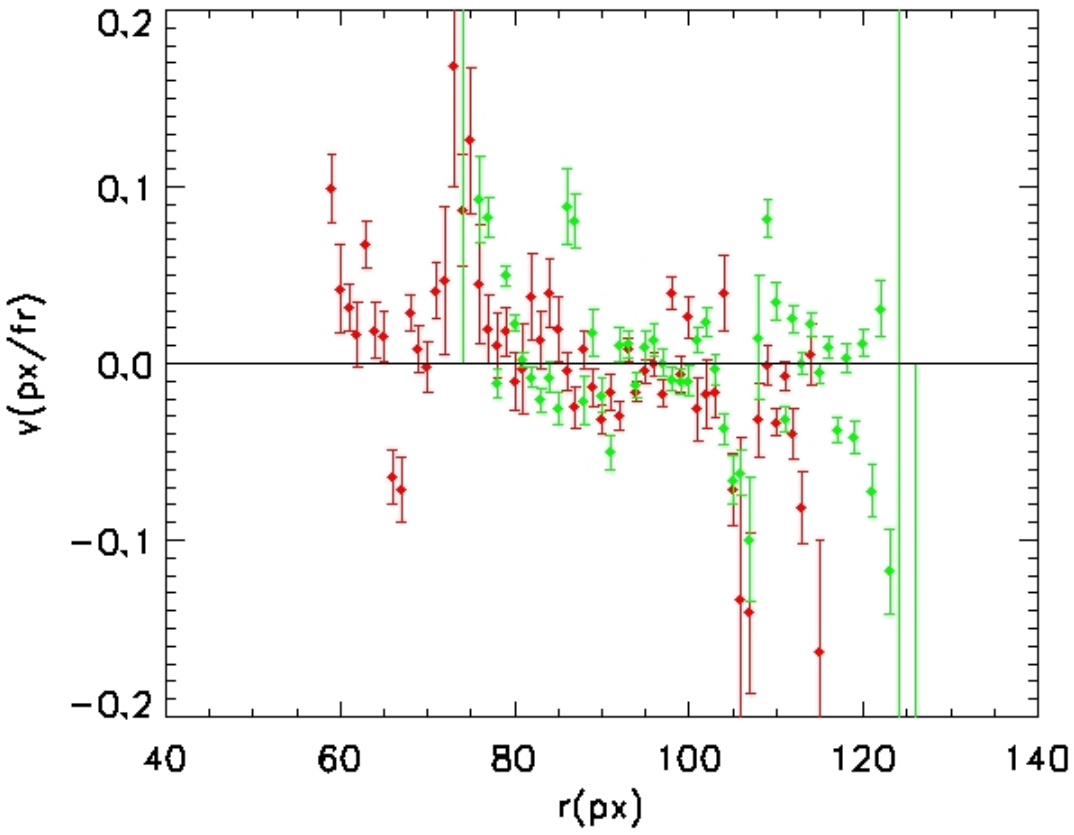

Figure 2.39: Interaction between particles in Figure 2.35. The red points are drift velocity in Figure 2.36 (particle 1 and particle 2). The green points are drift velocity in Figure 2.38 (particle 0 and particle 2). The frame rate is 30 fr/s. The particle diameter is 1.7 μm. The objective used was 20×, corresponding a magnification of 1.49 px/μm. The conversion factor from drift velocity to interaction force is 20 fN·fr/px. Data label: 092807.

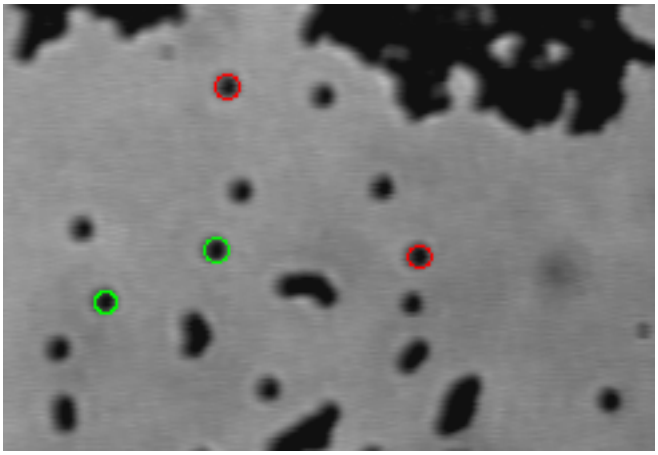

Figure 2.40: Polystyrene particles (diameter 1.7 μm) at a water-air interface. 63× objective was used, corresponding to magnification of 5.2 px/micron. Some of the monomers were circled with colors. The two monomers labeled with green circles bound and formed a dimer after a about 4 min. Data label: 101008.

As the number of particles increases at the interface, particles tend to form many clusters because of the short-range van der Waals attraction (Figure 2.40). However, there are still many monomers moving in the sample without binding others. To the eye, there *appears* to be a repulsion preventing those monomers forming clusters. We can pick any two of those monomers and measure the apparent interaction between them. As shown in Figure 2.41, the apparent interaction between the particles shown with red rings is slightly repulsive in the range of 40-60 px. There is a very small chance for two monomers to form a dimer (Figure 2.42, 2.43). In the analysis of interaction between the green-circled particles, however, there is no evidence of repulsion (Figure 2.42). The particles labeled with green rings formed a dimer, but relative drift velocity (Figure 2.42) do not show significant interaction before they formed a dimer.

For a more comprehensive study of the interactions at a crowded interface, we tracked 53 particles in the same sample as that of Figure 2.40 for a period of over 4 min. Figure 2.44 shows one frame of the tracking data with particle labels. Some of the tracked particles are within oligomers (*e.g.* particle 21) or large aggregates (*e.g.*

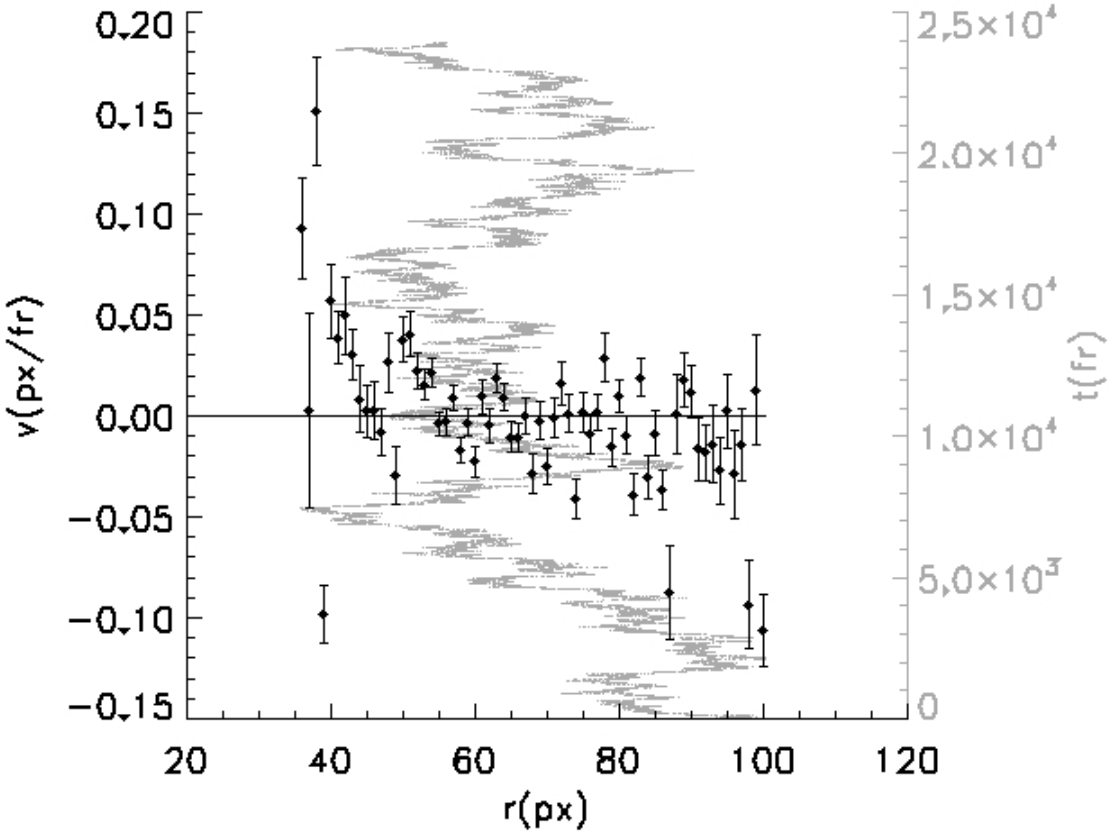

Figure 2.41: Interaction between the two particles labeled with red rings in Figure 2.40. The frame rate is 30 fr/s. The gray curve is the pair separation r as a function of time t. The black points are measured drift velocity v at different separation r. The particle diameter is 1.7 μm. The objective used was 63×, corresponding a magnification of 5.2 px/μm. The conversion factor from drift velocity to interaction force is 53 fN·fr/px. Data label: 101008.

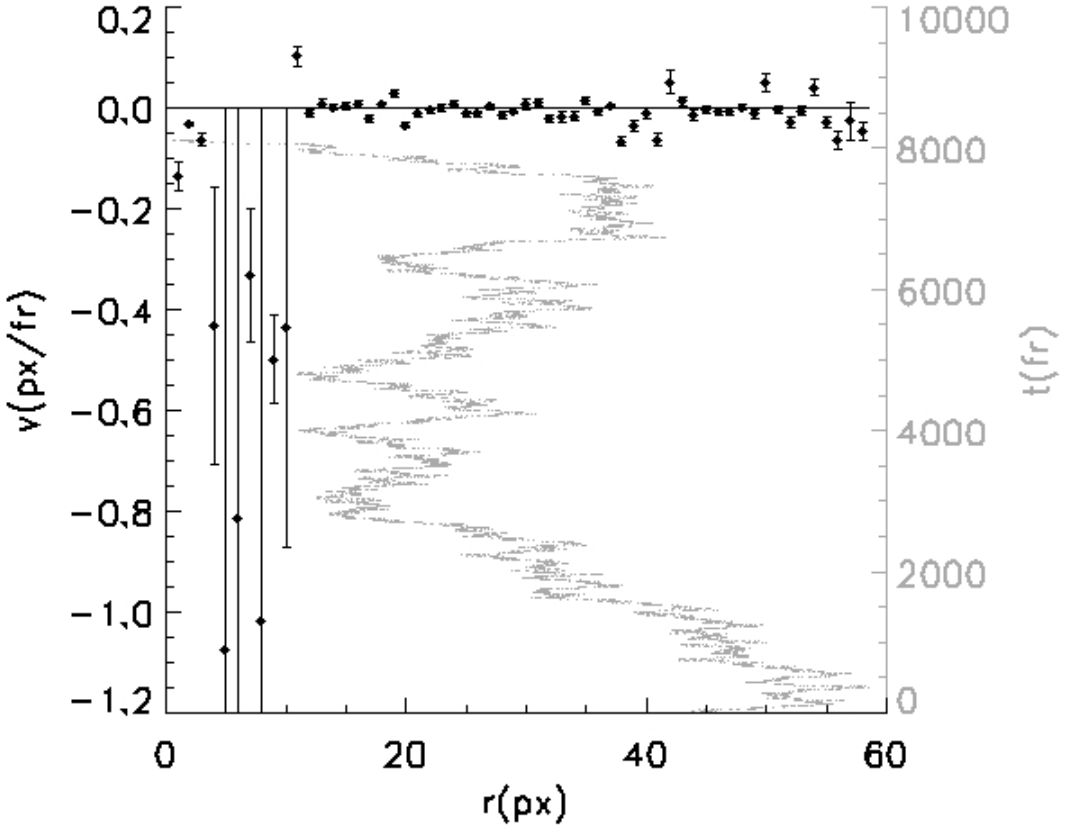

Figure 2.42: Formation of dimer interfered by many particles at a water-air interface (see monomers labeled with green circles in Figure 2.40). The frame rate is 30 fr/s. The objective used was 63×, corresponding a magnification of 5.2 px/μm. The particle diameter is 1.7 μm = 8.8 px. The gray curve is the pair separation r as a function of time t. The black points are measured drift velocity v at different separation r. Because of the size of solid particles, data points corresponding to $r \leq 8.8$ px come from the artifacts of image processing. The conversion factor from drift velocity to interaction force is 45 fN·fr/px. Data label: 101008.

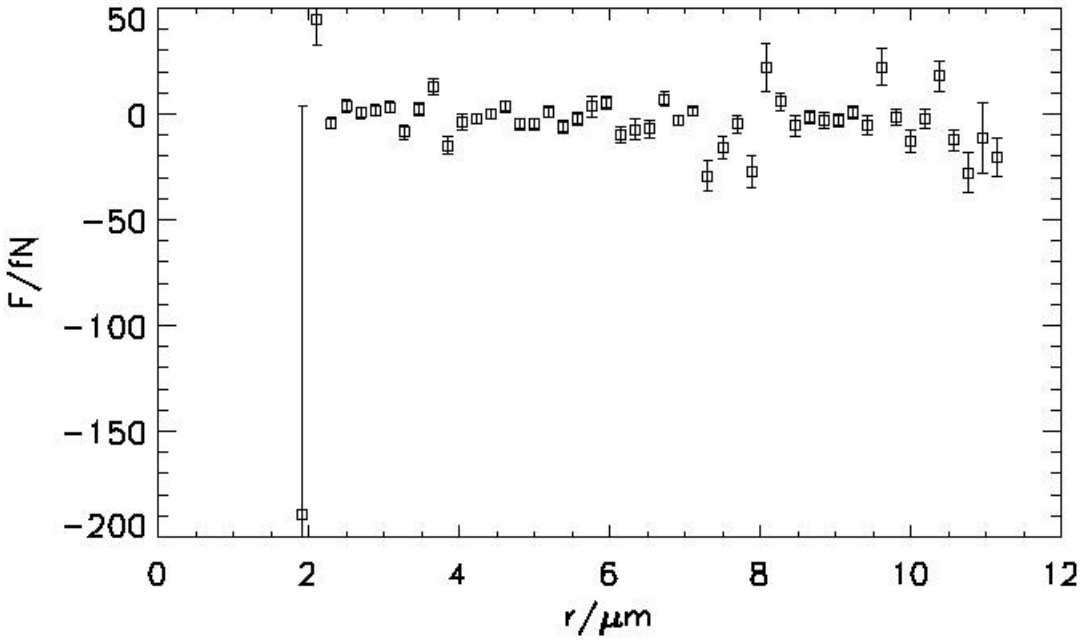

Figure 2.43: Interaction force between two particles which eventually formed a dimer (see monomers labeled with green circles in Figure 2.40). Data label: 101008.

particle 0). Some of them bound with other particles within the period of tracking (*e.g.* particle 18). Among the 53 tracked particles, 20 remained monomers throughout the period of tracking, with labels being 8, 10, 14, 15, 16, 17, 19, 20, 23, 24, 31, 32, 36, 39, 42, 43, 48, 50, 52, 53. From the 20 monomers, there are $\binom{20}{2} = 190$ combinations of pairs. The interaction of all the pairs were calculated. Most of these pairs do not show significant interaction, with examples shown in Figure 2.45, 2.46. For the particular case of particle 42 and 43, however, the separation stayed around 20 px for over 4000 fr (Figure 2.47). As a result, it appears to be a potential well. However, it is the only example that shows a possible attractive well, and the calculated relative drift velocity is still comparable to the error, and the corresponding interaction force is only about 1 fN. We thus conclude that there is no measurable force between those particles. And no evidence of a strong attraction of monomers to large aggregates (such as the one shown at the upper edge of Figure 2.40) was found.

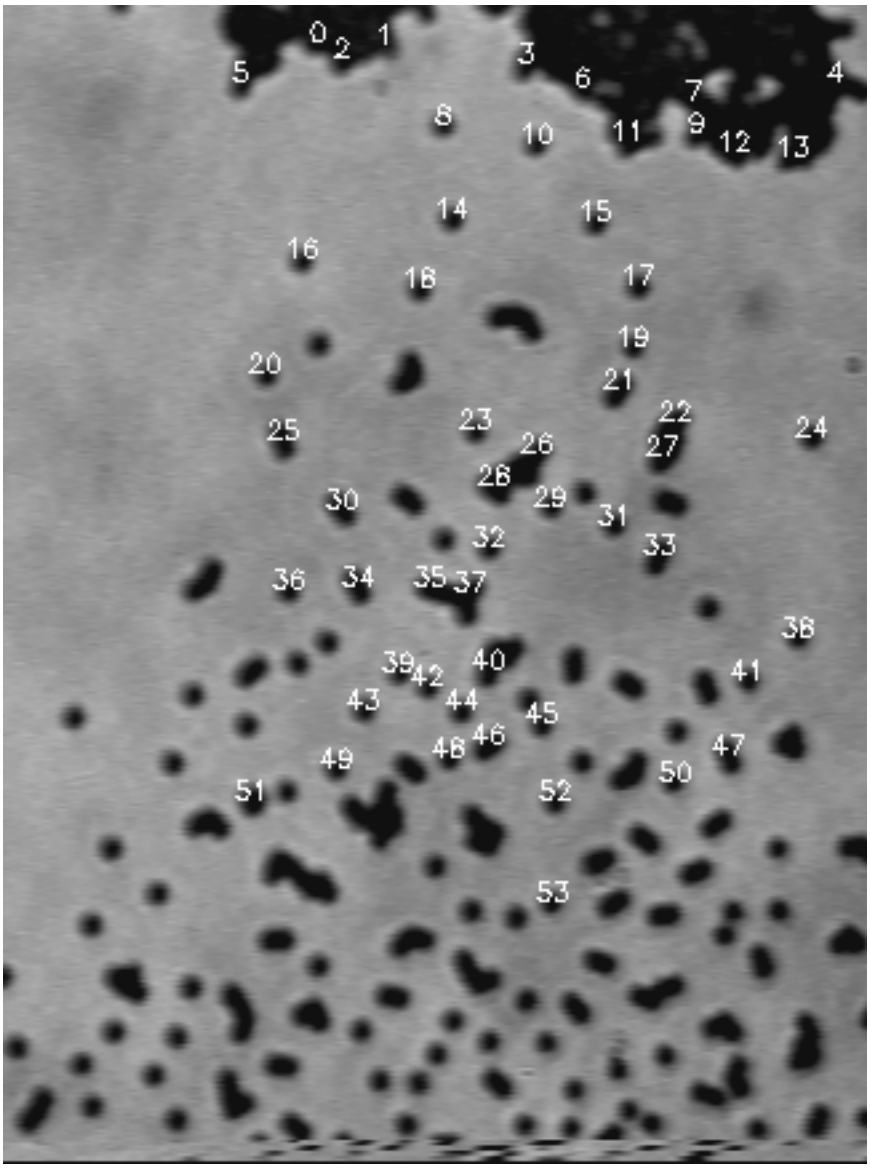

Figure 2.44: Polystyrene particles (diameter 1.7 μm) at a water-air interface. 63$\times$ objective was used, corresponding to magnification of 5.2 px/micron. Data label: 101008.

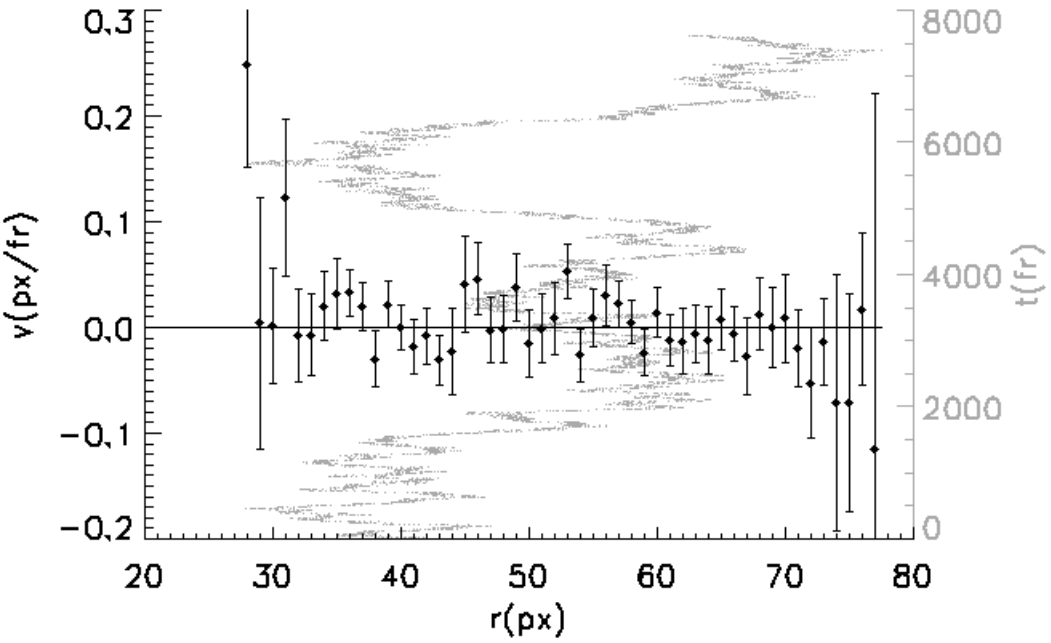

Figure 2.45: Interaction between the particle 10 and particle 15 as labeled in Figure 2.44. The frame rate is 30 fr/s. The gray curve is the pair separation r as a function of time t. The black points are measured drift velocity v at different separation r. The particle diameter is 1.7 μm. The objective used was 63×, corresponding a magnification of 5.2 px/μm. The conversion factor from drift velocity to interaction force is 53 fN·fr/px. Data label: 101008.

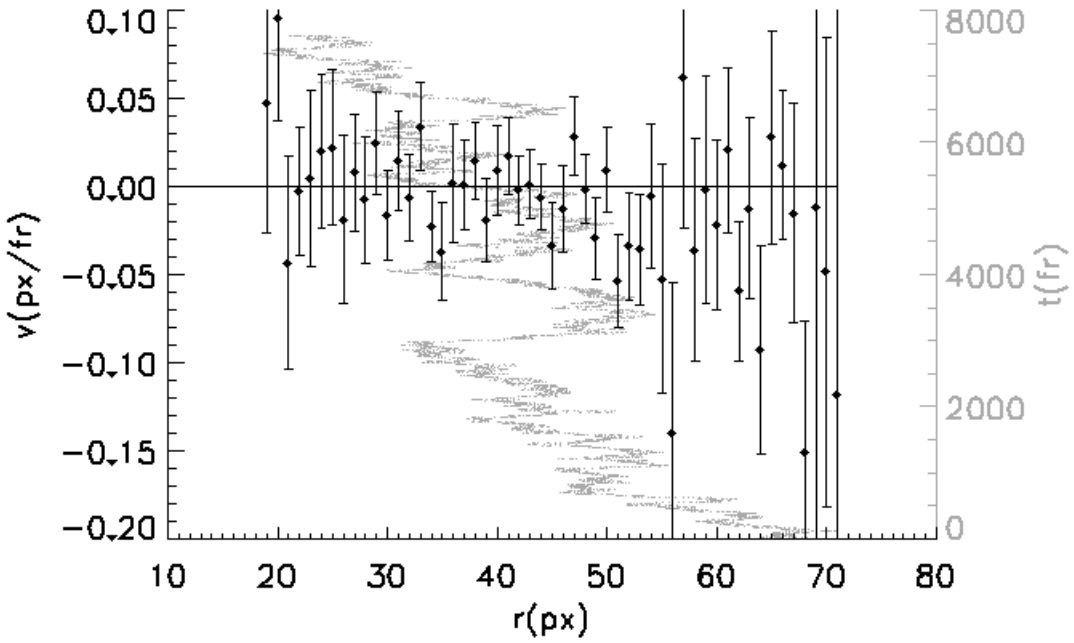

Figure 2.46: Interaction between the particle 48 and particle 53 as labeled in Figure 2.44. The frame rate is 30 fr/s. The gray curve is the pair separation r as a function of time t. The black points are measured drift velocity v at different separation r. The particle diameter is 1.7 μm. The objective used was 63×, corresponding a magnification of 5.2 px/μm. The conversion factor from drift velocity to interaction force is 53 fN·fr/px. Data label: 101008.

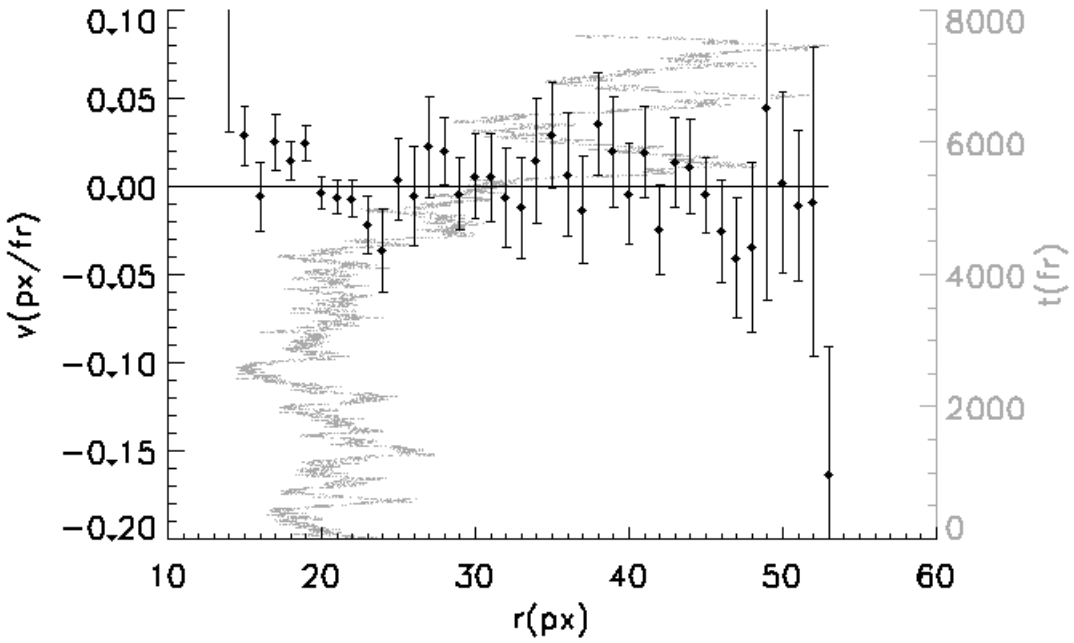

Figure 2.47: Interaction between the particle 42 and particle 43 as labeled in Figure 2.44. The frame rate is 30 fr/s. The gray curve is the pair separation r as a function of time t. The black points are measured drift velocity v at different separation r. The particle diameter is 1.7 μm. The objective used was 63×, corresponding a magnification of 5.2 px/μm. The conversion factor from drift velocity to interaction force is 53 fN·fr/px. Data label: 101008.

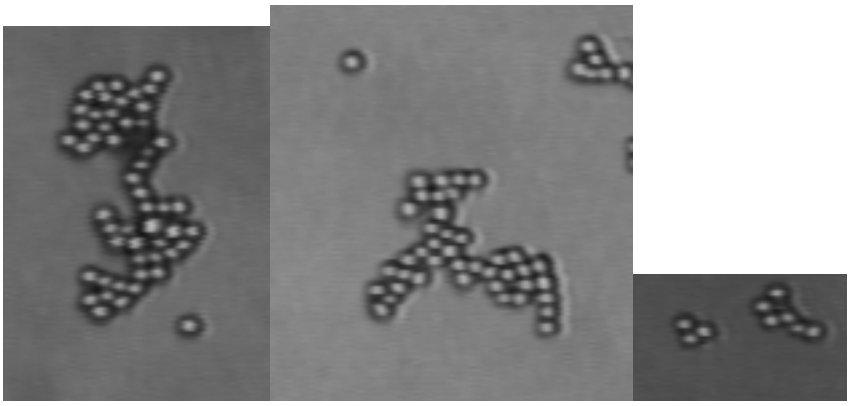

Figure 2.48: Clusters formed by 2 micron carboxyl-modified latex beads at an interface of water and 1,1,1-trifluoroheptan-2-ol.

2.8 Interactions involving clusters

To probe the effect of the type of oil, we measured interactions among particles at an interface of water and trifluoroheptan-2-ol. In this case, we observed clusters that formed throughout the sample. Figure 2.48 shows some examples of clusters.

The deterministic monomer-cluster attraction and the attraction between clusters were observed and measured. The interactions involving clusters are quite strong and give rise to mostly deterministic motion. We have watched the process of monomer approaching and then joining cluster, and also clusters attracting each other. Orientation is important in both cases due to the asymmetry of cluster shape. Strong orientational preference was observed, indicating the complex anisotropy of interface deformation.

We measured the separation between clusters (or monomer and cluster). As long as the cluster does not rearrange, we can take position of one monomer in the cluster to represent the position of the whole cluster. Velocity was obtained by differentiating the separation between clusters (or monomer and cluster) with respect to time. We observed distinct acceleration just before particles touching each other (Figure 2.50a). Because these particles are over-damped at the timescale of the frame interval, we can

relate the measured velocity to the force. The magnitude of force can be estimated as $6\pi\eta rv$, where η is the viscosity of surrounding fluid. Here, we have assumed that the friction constant of the bead is the same as for an isolated bead immersed in water. For a particle at a liquid interface, the friction constant will differ, but since the viscosities of the water and oil are comparable the error should be small. The peak speed in Figure 2.50a is about 1 pixel/frame = 3.7 μm/s. Taking the viscosity of water $\eta = 1$ mPa·s, we find force $f = 7 \times 10^{-14}$ N. We also analyzed 3 instances of cluster-cluster attraction and the results of peak velocity were with the same order of magnitude.

For comparison, we can estimate the contribution of gravity to this attractive force. From Equation 1.10 for the "Cheerios" interaction, $f = \frac{\partial U}{\partial r} = \frac{(\Delta\rho V g)^2}{2\pi\gamma r}$. Here $\Delta\rho \sim 50$ kg/m^3. Taking the surface tension of water $\gamma = 73$ mN/m, we get the contribution of gravity in the order of 10^{-23} N, which is absolutely negligible compared to the measured value.

2.9 Summary

To summarize, in Figure 2.52 we replotted data the air-water experiments described in the previous sections. The black points are from isolated pair (Figure 2.12). The red and green points represent pair interaction affected by another monomer (Figure 2.36 and Figure 2.38, respectively). The blue points represent interfered pair interaction with many other particles around (Figure 2.45). After accounting for the erroneous apparent repulsion that appears in the first few data points, we find that the isolated pair interaction is close to zero. The pair interaction affected by one monomer is also insignificant.

The absence of significant interaction betwen monomers and clusters at an air-water interface is in contradiction with previous measurements in [65] and [66]. To investigate whether the method of inverting $g(r)$ might be at fault, we calculated the

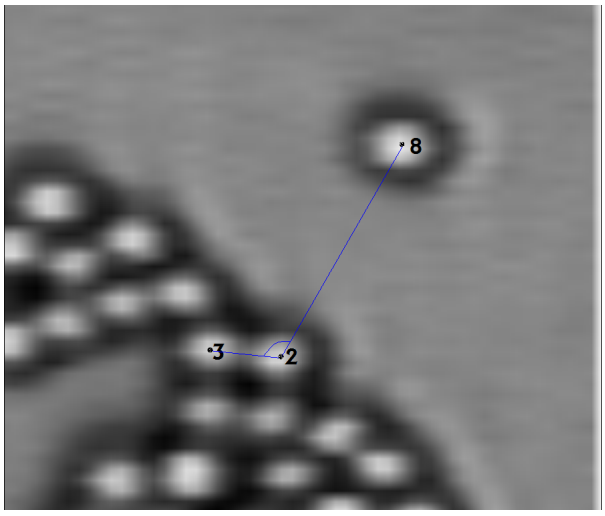

(a) Particle 8 combined particle 2

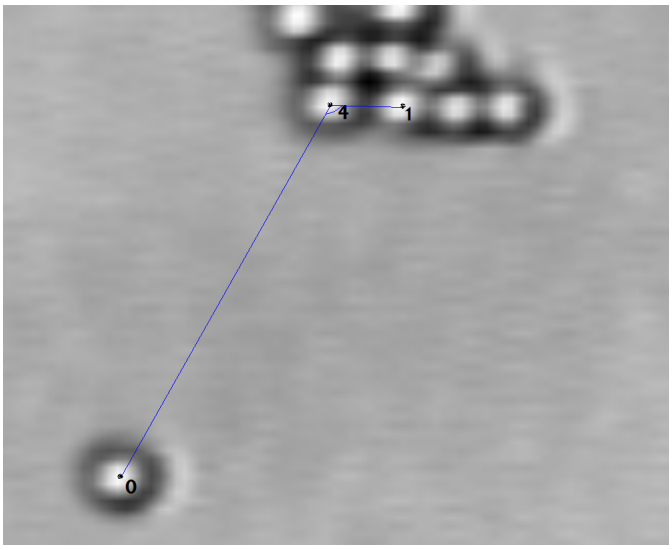

(b) Particle 0 combined particle 4

Figure 2.49: Cluster growth. PS beads (diameter: 2.0 μm) at an interface of water and 1,1,1-trifluoroheptan-2-ol. Original magnification: 8.1 pixel/μm; frame rate: 30 s^{-1}. Images enlarged to help labeling particles. Clusters formed by 2 micron carboxyl-modified latex beads at water-oil interface.

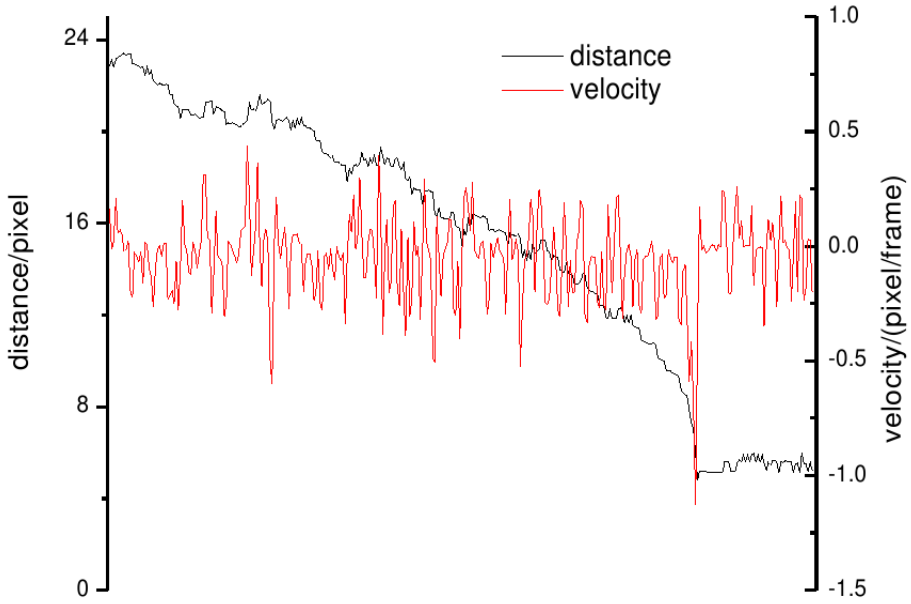

(a) Distance between particle 8 and particle 2. Relative velocity given by time derivative of distance.

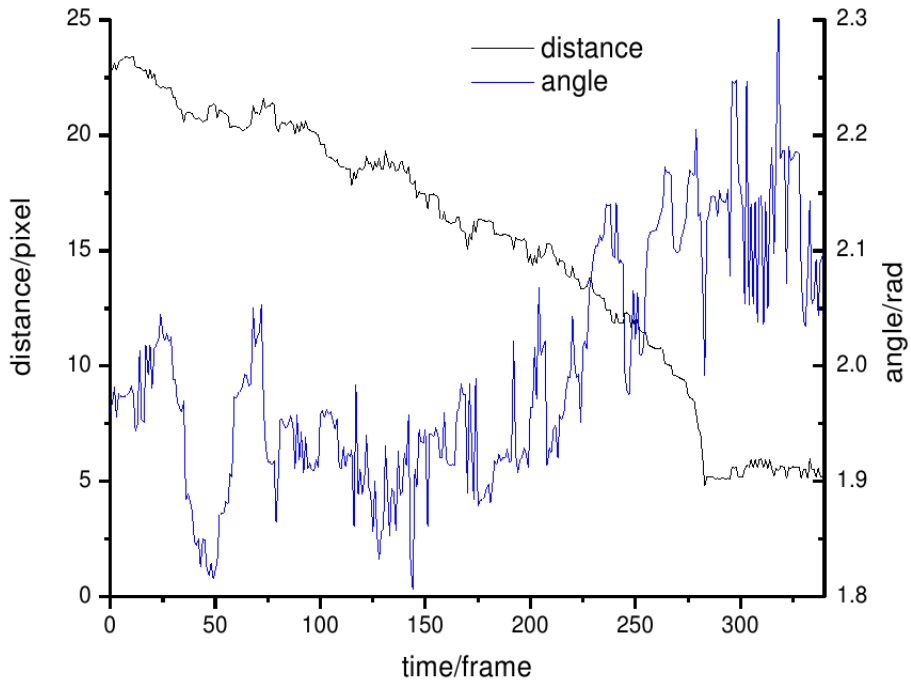

(b) Angle 823 compared with the time-evolution of monomer-cluster distance.

Figure 2.50: Analysis of cluster growth in Figure 2.49a.

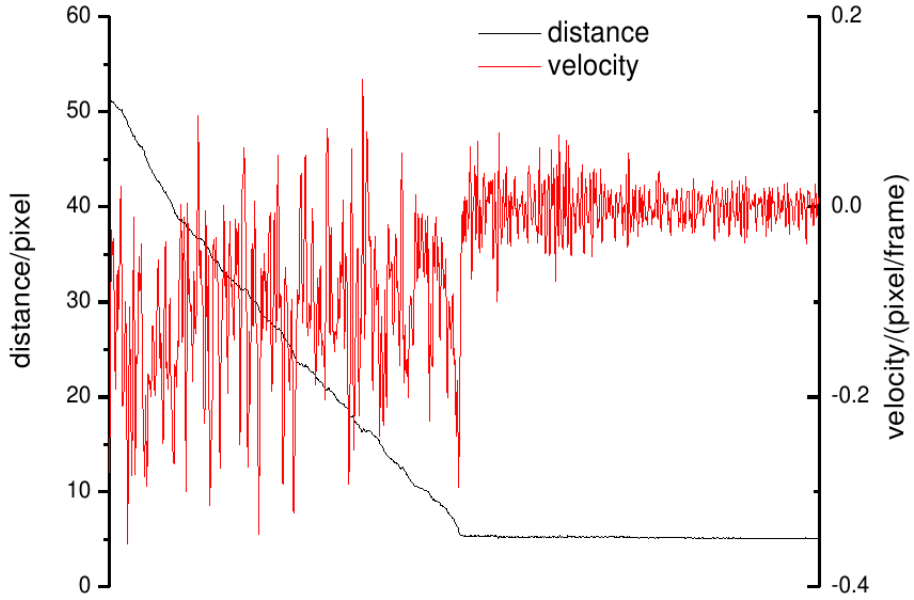

(a) Distance between particle 0 and particle 4. Relative velocity given by time derivative of distance.

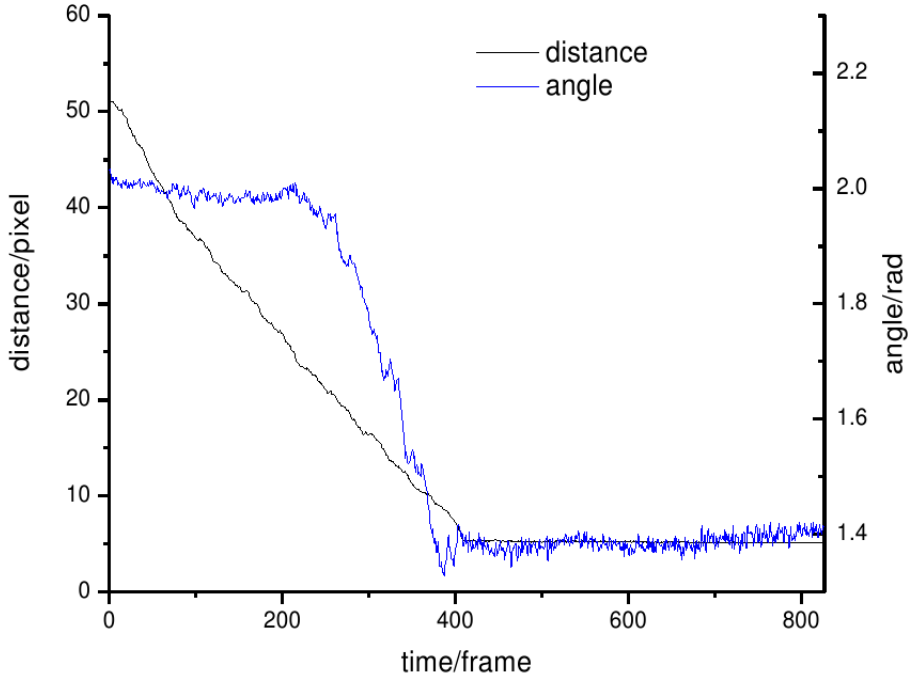

(b) Angle 041 compared with the time-evolution of monomer-cluster distance

Figure 2.51: Analysis of cluster growth in Figure 2.49b.

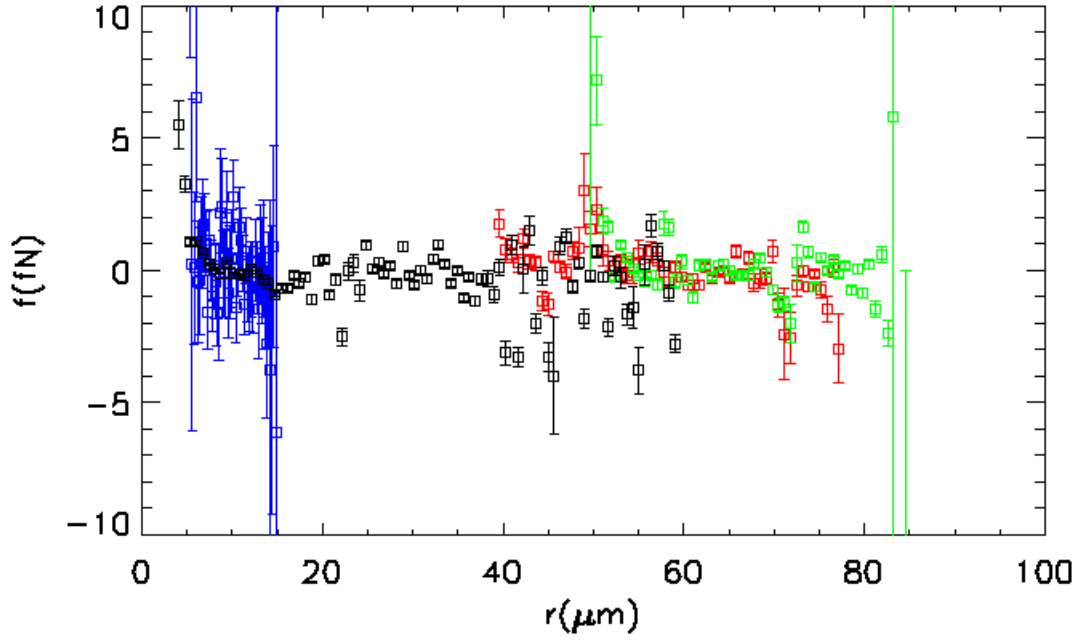

Figure 2.52: Interaction force between different pairs. Data replotted from previous sections. Black: an isolated pair (Figure 2.12). Red: a pair affected by a third particle nearby (Figure 2.36). Green: another pair affected by a third particle nearby (Figure 2.38). Blue: a pair interfered by many other particles (Figure 2.45). See text.

radial distribution function $g(r)$ in the sample of Figure 2.44. Figure 2.53 shows the $g(r)$ averaged over 3000 frames. The interframe deviations are very small, resulting in error bars much smaller than the plot symbols. The peak at about $2.5d$ (where d is the particle diameter) also implies repulsive interaction, similar to Figure 3 in [65]. Since our direct measurement of pair interaction confirms the insignificance of this interaction, we suspect the method involving $g(r)$ from an ensemble of particles cannot reflect the true interaction potential between pairs of particles. The reason could be related to the fact that the system is not at equilibrium: the relative scarcity of particles that are within 2.5 diameters of one another is not from repulsion, but instead is because some of these particles become irreversibly bound by van der Waals interaction. The method of obtaining interactions by inverting g(r) should be used with great care. The distinction from the results of Chen *et al.* [66] could arise from using different particles (though nominally the same, the charge state on the air side might differ). It is also possible that the difference arises from the fact that the other authors constructed their sample cell from teflon, which has a tendency to develop static voltages on the order of -1 kV when rubbed [76]. The present experiments were done with a metal (brass) cell, so that electrostatic charge is less likely to accumulate. The role of static charge buildup is a topic that should be investigated further.

The interaction between a monomer and a cluster at the fluorocarbon-water interface (Section 2.8) is much stronger than at the air-water interface. We ruled out the contribution of Cheerios effect due to gravity in Section 2.8. For polystyrene particles at water-air interface, $\Delta\rho$ can be as large as 10^3 kg/m^3. Then $f = \dfrac{(\Delta\rho V g)^2}{2\pi\gamma r} \sim 10^{-21}$ N, which is still undetectable. In the following chapters, we propose a correction to the standard Cheerios model arising from the anisotropic shape of the interface around each particle. Specifically in Section 6.3, we show that this correction is still insufficient to explain the measured strong interaction between particles and clusters

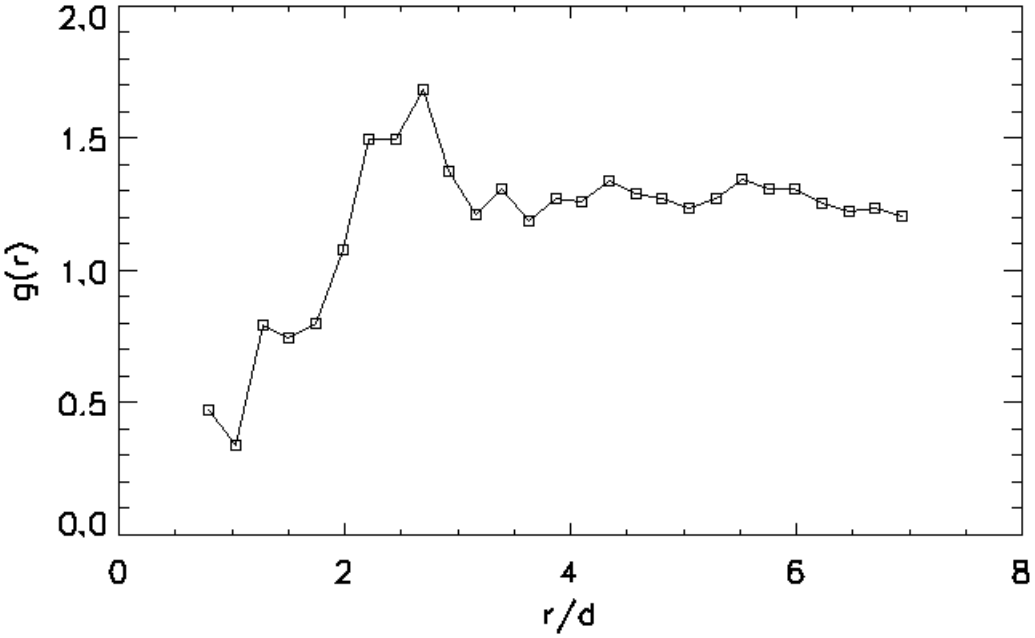

Figure 2.53: Radial distribution function $g(r)$ of colloidal particles at an air-water interface averaged over 3000 consecutive frames. The separation r is rescaled by the particle diameter d. The corresponding error bars are much smaller than the plot symbols.

in Section 2.8. Although the curvature effect may enhance the attraction, the size of a cluster determines the minimum separation it can make with a monomer.

In summary, our measurements show negligible interactions (other than van der Waals attraction) among particles at the air-water interface at low and high concentrations. This result is consistent with predictions of the capillary interactions among neutral particles. Our result differs from previous reports for a similar system, and we offered possible explanations. Among particles at a fluorocarbon oil-water interface, however, we find interactions that are far stronger than can be predicted for neutral particles. In this case, we propose that charge dissociation at the particle-oil interface might explain the results. This remains an area for future investigations.

CHAPTER 3

MATHEMATICAL MODELING OF INTERFACIAL DEFORMATION

As introduced in Section 1.3, particles on interfaces are subject to many types of forces. Our purpose here is to focus on the most elementary aspect of this diverse subject: interfacial energy with a given contact angle $0 < \theta_c < \pi$ between the solid particles and the fluid interface. We investigate how a non-planar interface is deformed when a spherical particle adsorbs.

We will follow the assumption that the particle's surface is smooth and homogeneous (Section 1.3.2.1) so that the contact angle maintains a constant value along the contact line. When a spherical particle meets an interface without azimuthal symmetry around the normal direction, the interface will be deformed upon adsorption of particle to satisfy the condition of contact angle. The purpose of this chapter is to present analytical solutions to the deformation of interfaces when a spherical particle adsorbs. In Chapter 4, we study the adsorption energy of a spherical particle to a non-planar interface.

3.1 Parabolic interface

We begin with a mathematically straightforward problem of a parabolic interface. These results will provide a useful comparison to the more realistic problem of the cylinder described in Section 3.2.

---

[0]Contributions: Anthony D. Dinsmore initiated and conducted the study. Benny Davidovitch proposed the Helmholtz equation. Fabian Brau and Chuan Zeng formulated and solved the boundary value problem. Chuan Zeng performed numerical computation.

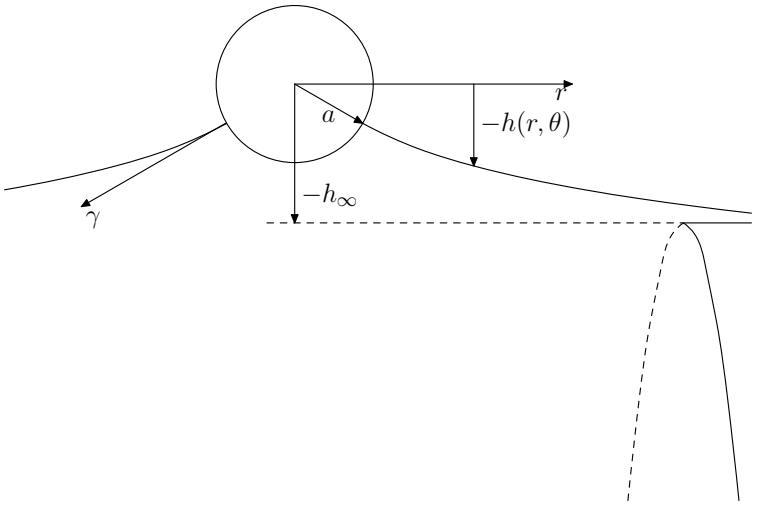

Figure 3.1: Particle adsorbed to parabolic interface. The x axis points to the right and coincides with the polar axis. y axis goes into the paper plane. ($x \equiv r\cos\theta, y \equiv r\sin\theta$.)

Consider an interface initially with shape described as

$$h(x,y) = -\frac{y^2}{2R}. \tag{3.1}$$

We will describe the shape in the Monge representation and assume $\nabla h \ll 1$ so that we can approximate H as $\frac{1}{2}\nabla^2 h$ (Equation 1.4). The condition for Equation 1.4 requires $(y/R)^2 \ll 1$. The parabola is parametrized this way to emphasize its total curvature $1/R$. A particle with radius a is brought into contact with the interface along x-axis (Figure 3.1). The particle is expected to be pushed up by the Laplace pressure. If the center of the particle is defined as origin, the equation describing the unperturbed interface would be shifted down by $-h_\infty$.

3.1.1 Poisson's equation

We look for solution to the Poisson's equation in polar coordinates:

$$\nabla^2 h = \frac{1}{r}\partial_r r \partial_r h + \frac{1}{r^2}\partial^2_{\theta,\theta} h = -\frac{1}{R}. \tag{3.2}$$

The rotational and mirror symmetries of the system restrict the form of solution to

$$h = a_0 + \sum_{n=1}^{\infty} \left(a_n r^{2n} + \frac{b_n}{r^{2n}} \right) \cos 2n\theta - \frac{r^2}{4R}, \tag{3.3}$$

with a_0, a_n, and b_n to be determined.

3.1.2 Boundary condition on particle surface

The contact angle is defined as the angle made by the normal of particle surface and the normal of interface. The condition for 90° contact angle turned out to be straightforward by taking the 1st order approximation on $\partial_r h$ and $\partial_\theta h/r$:

$$\partial_r h|_{r=a} = \frac{h(a,\theta)}{a}. \tag{3.4}$$

3.1.3 Solution

The shape of interface deformed by one particle was solved from Equations. 3.2 and 3.4. By imposing the asymptotic condition that the interfacial shape be parabolic far away, we obtain

$$h = -\frac{a^2}{4R} - \frac{r^2 \sin^2\theta}{2R} + \frac{a^4}{12Rr^2} \cos 2\theta. \tag{3.5}$$

The first term in the solution corresponds to vertical shift h_∞ in Figure 3.1. The second term is the undisturbed interfacial shape The third term is the deformation caused by the adsorbed particle. It is a field of quadrupolar symmetry in xy-plane. For arbitrary contact angle θ_c, it was shown that the solution can be obtained by replacing a with $a \sin\theta_c$.

Result shows that there is a deformation that decays as a power law. However, the parabola is not a satisfactory example because it does not have constant mean curvature.

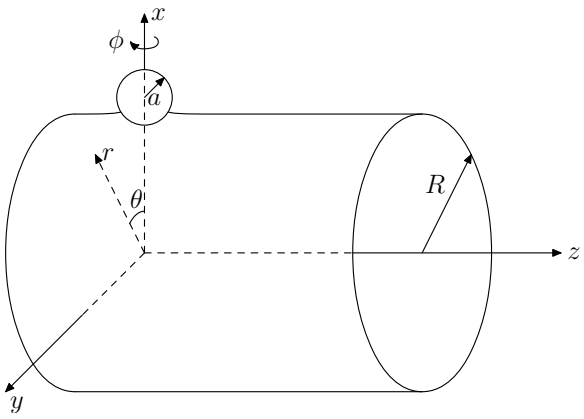

Figure 3.2: Particle at cylindrical interface, with coordinate frames redefined. Polar axis coincides with x axis.

3.2 Cylindrical interface

In this section we focus on the simplest, yet nontrivial constant mean curvature (CMC) surface: an infinitely long cylinder[1] of radius $R \ll a$. The interface will be described as

$$r(\theta, z) = R + f(\theta, z)\frac{a^2}{R}, \tag{3.6}$$

with $x = r\cos\theta$, $y = r\sin\theta$ (Figure 3.2). Note that (x, y, z) and (r, θ) are defined differently from the previous section. Here $\dfrac{a^2 f}{R}$ is the deformation of the interface perpendicular to the initial cylinder. Dimensional analysis suggests that the order of dimensionless factor f should not exceed $O(1)$, which will also be supported by the calculation described here.

3.2.1 Generalization of parabolic interface

In this section we attempt to approximately find an analytical solution to the cylindrical interface using the result from the previous section.

As the 2nd order approximation of cylinder, the result from the parabola in the previous section can be extrapolated to cylindrical coordinates ($x \to z$, $y \to R\theta$).

[1]The stability of CMC surface is *not* discussed in the present study.

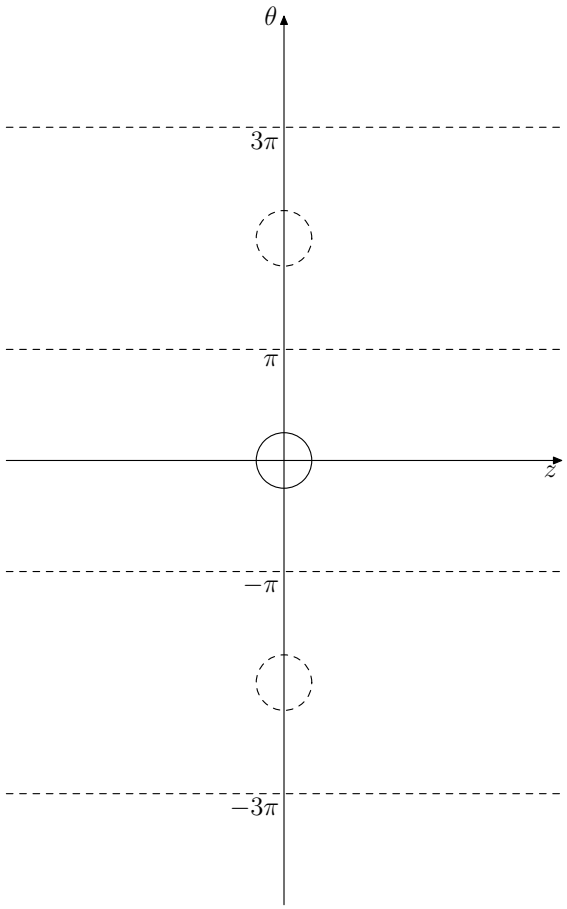

Figure 3.3: Method of images.

The quadrupole deformation in Equation 3.5 is mapped as

$$r = R + \frac{a^4 \sin^4 \theta_c}{12R} \frac{z^2 - R^2\theta^2}{\left(z^2 + R^2\theta^2\right)^2}, \tag{3.7}$$

$$f = \frac{a^2 \sin^4 \theta_c}{12} \frac{z^2 - R^2\theta^2}{\left(z^2 + R^2\theta^2\right)^2}. \tag{3.8}$$

f is now of $O(1)$ near contact ($z^2 + R^2\theta^2 \sim a^2$) and $f \sim O\left(\delta^2\right)$ when $z^2 + R^2\theta^2 \sim R^2$, with the ratio $\delta = \frac{a}{R}$.

However, the quadrupole solution does not satisfy the periodicity condition for the cylindrical interface, which requires

$$f(\theta + 2\pi, z) = f(\theta, z) \quad \forall\theta. \tag{3.9}$$

To better approximate the cylindrical interface perturbed upon adsorption of particle, image quadrupoles were introduced and summed up to meet the conditions of continuity and periodicity (Figure 3.3). The resulted deformation f is

$$f = \frac{a^2 \sin^4 \theta_c}{12} \sum_{n=-\infty}^{\infty} \frac{z^2 - R^2(\theta + 2n\pi)^2}{\left[z^2 + R^2(\theta + 2n\pi)^2\right]^2} \tag{3.10}$$

$$= \frac{a^2 \sin^4 \theta_c}{24R^2} \frac{\cosh \frac{z}{R} \cos\theta - 1}{\left(\cosh \frac{z}{R} - \cos\theta\right)^2}. \tag{3.11}$$

Near contact, $\frac{z}{R} \sim \theta \sim \delta$,

$$\frac{\cosh \frac{z}{R} \cos\theta - 1}{\left(\cosh \frac{z}{R} - \cos\theta\right)^2} = 2 \frac{\frac{z^2}{R^2} - \theta^2}{\left(\frac{z^2}{R^2} + \theta^2\right)^2} \left[1 + O\left(\delta^2\right)\right]. \tag{3.12}$$

The leading term of Equation 3.11 is exactly the same as Equation 3.8, *i.e.*, the image quadrupoles act as high order corrections and would not disturb the condition of contact angle significantly.

3.2.2 Helmholtz equation

The surface described by Equation 3.6 maintains mean curvature of $\frac{1}{2R}$. With $\delta \ll 1$, one can show that the leading term of the perturbation f satisfies the Helmholtz equation [77]:

$$\nabla^2 f + \frac{f}{R^2} = 0, \tag{3.13}$$

where $\nabla^2 = \frac{1}{R^2}\partial^2_{\theta,\theta} + \partial^2_{z,z}$.

3.2.3 Boundary condition

3.2.3.1 Equation of contact line

Similar to z_∞ in Figure 1.4, the balanced distance between center of particle and axis of cylinder is *unknown*. However, it is obvious that the leading order of this

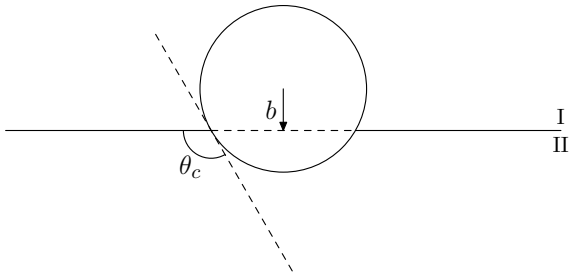

Figure 3.4: Definition of contact angle θ_c.

separation is $R + b$ with b defined as $b = -a\cos\theta_c$ (Figure 3.4). We fix the center of the particle at $R + b$ and allow the interface to shift along x-direction and minimize interfacial energy. We write the equation of particle surface as

$$(r\cos\theta - R - b)^2 + r^2\sin^2\theta + z^2 = a^2. \tag{3.14}$$

The equation of contact line can be solved from Equation 3.6 and 3.14. Assuming $a \sim b \sim R\theta$, the contact line is a circle with radius $\sqrt{a^2 - b^2}$ in θz-plane:

$$\begin{aligned}
\left[\left(R + \frac{a^2}{R}f\right)\left(1 - \frac{\theta^2}{2}\right) - R - b\right]^2 + \left(R + \frac{a^2}{R}f\right)^2\theta^2 + z^2 =& a^2 \\
\left[\left(1 + \delta^2 f\right)\left(1 - \frac{\theta^2}{2}\right) - 1 - \tilde{b}\right]^2 + \left(1 + \delta^2 f\right)^2\theta^2 + \tilde{z}^2 =& \delta^2 \\
\left(1 + f\delta^2 - \frac{\theta^2}{2} - 1 - \tilde{b}\right)^2 + \theta^2 + \tilde{z}^2 + O\left(\delta^3\right) =& \\
\left(f\delta^2 - \frac{\theta^2}{2} - \tilde{b}\right)^2 + \theta^2 + \tilde{z}^2 + O\left(\delta^3\right) =& \\
\tilde{b}^2 + \theta^2 + \tilde{z}^2 + O\left(\delta^3\right) =& \\
R^2\theta^2 + z^2 =& a^2 - b^2 + R^2 O\left(\delta^3\right).
\end{aligned} \tag{3.15}$$

Dimensionless $\tilde{b}$, $\tilde{z}$ were rescaled with R. $\tilde{b}$ is of the same order as δ, while $\tilde{z}$ can be large.

3.2.3.2 Normal to particle surface at contact

$$
\begin{aligned}
a\hat{\boldsymbol{n}}_p =& (r\cos\theta - R - b, r\sin\theta, z) \\
\hat{\boldsymbol{n}}_p =& \left[\frac{\left(R+\frac{a^2}{R}f\right)\cos\theta - R - b}{a}, \frac{\left(R+\frac{a^2}{R}f\right)\sin\theta}{a}, \frac{z}{a}\right] \\
=& \left[\left(\frac{R}{a}+\frac{a}{R}f\right)\left(1-\frac{\theta^2}{2}\right) - \frac{R}{a} - \frac{b}{a} + O\left(\delta^3\right), \frac{R\theta}{a} + \frac{a}{R}f\theta + O\left(\delta^2\right), \frac{z}{a}\right] \\
=& \left[-\frac{R\theta^2}{2a} + \frac{a}{R}f - \frac{b}{a} + O\left(\delta^3\right), \frac{R\theta}{a} + \frac{a}{R}f\theta + O\left(\delta^2\right), \frac{z}{a}\right] \\
=& \left[O(1) + O(\delta), O(1) + O\left(\delta^2\right), O(1)\right].
\end{aligned}
$$

3.2.3.3 Perturbed cylindrical interface

$$
\begin{aligned}
x =& \left(R+\frac{a^2}{R}f\right)\cos\theta, \\
y =& \left(R+\frac{a^2}{R}f\right)\sin\theta, \\
z =& z.
\end{aligned}
$$

We represent the height of the interface x as a function of y and z. Then the vector normal to the interface is $\hat{\boldsymbol{n}}_i \propto (1, -\partial_y x, -\partial_z x)$. Assuming $\partial_\theta f \sim \frac{1}{\delta}$, $\partial_z f \sim \frac{1}{a}$ at contact (which will be verified later), we derive $\partial_y x$, $\partial_z x$ up to $O\left(\delta^2\right)$:

$$
x = \left\{R+\frac{a^2}{R}f\left[\theta(y,z),z\right]\right\}\cos\theta(y,z), \tag{3.16}
$$

$$
y = \left\{R+\frac{a^2}{R}f\left[\theta(y,z),z\right]\right\}\sin\theta(y,z). \tag{3.17}
$$

Taking the derivative of both sides of Equation 3.17 with respect to y, we obtain:

$$\begin{aligned} 1 &= \left(R + \frac{a^2}{R} f\right) \cos\theta \partial_y \theta + \frac{a^2}{R} \partial_\theta f \partial_y \theta \sin\theta \\ \partial_y \theta &= \frac{1}{\left(R + \frac{a^2}{R} f\right) \cos\theta + \frac{a^2}{R} \partial_\theta f \sin\theta}. \end{aligned} \tag{3.18}$$

The derivative with respect to z may be written as

$$\begin{aligned} 0 &= \left(R + \frac{a^2}{R} f\right) \cos\theta \partial_z \theta + \frac{a^2}{R} \partial_z f \sin\theta, \\ \partial_z \theta &= -\frac{a^2 \partial_z f \sin\theta}{(R^2 + a^2 f)\cos\theta + a^2 \partial_\theta f \sin\theta}. \end{aligned} \tag{3.19}$$

Find $\partial_y x$ and $\partial_z x$ from Equation 3.16 using Equations 3.18 and 3.19:

$$\begin{aligned} \partial_y x &= -\left(R + \frac{a^2}{R} f\right) \sin\theta \partial_y \theta + \frac{a^2}{R} \partial_\theta f \partial_y \theta \cos\theta, \\ &= \frac{-\left(R + \frac{a^2}{R} f\right) \sin\theta + \frac{a^2}{R} \partial_\theta f \cos\theta}{\left(R + \frac{a^2}{R} f\right) \cos\theta + \frac{a^2}{R} \partial_\theta f \sin\theta}, \\ &= \frac{-\theta + \delta^2 \partial_\theta f}{1 - \frac{\theta^2}{2} + f\delta^2 + \delta^2 \theta \partial_\theta f}, \\ &= -\theta + \delta^2 \partial_\theta f + O\left(\delta^3\right). \end{aligned}$$

$$\begin{aligned} \partial_z x &= -\left(R + \frac{a^2}{R} f\right) \sin\theta \partial_z \theta + \frac{a^2}{R} \left(\partial_z f + \partial_\theta f \partial_z \theta\right) \cos\theta, \\ &= \frac{a^2}{R} \partial_z f \cos\theta + \left(\frac{a^2}{R} \partial_\theta f \cos\theta - R\sin\theta - \frac{a^2}{R} f \sin\theta\right) \partial_z \theta, \\ &= \frac{a^2}{R} \partial_z f + O\left(\delta^3\right). \end{aligned}$$

$$\begin{aligned}\hat{\boldsymbol{n}}_i &= \frac{(1, -\partial_y x, -\partial_z x)}{\sqrt{1 + (\partial_y x)^2 + (\partial_z x)^2}} \\ &= \left[1 - \frac{1}{2}(\partial_y x)^2 - \frac{1}{2}(\partial_z x)^2 + O\left(\delta^4\right), -\partial_y x + O\left(\delta^3\right), -\partial_z x + O\left(\delta^3\right)\right].\end{aligned}$$

3.2.3.4 Contact angle constraint

The constraint of constant contact angle reads

$$\hat{\boldsymbol{n}}_p \cdot \hat{\boldsymbol{n}}_i = \cos\theta_c \equiv -\frac{b}{a}. \tag{3.20}$$

To the order of $O(1)$, Equation 3.20 is always satisfied by definition. To order $O(\delta)$:

$$\begin{aligned}\hat{\boldsymbol{n}}_p \cdot \hat{\boldsymbol{n}}_i =& -\frac{R\theta^2}{2a} + \frac{a}{R}f - \frac{R\theta}{a}\left(-\theta + \delta^2\partial_\theta f\right) - \delta\partial_z f z \\ =& \frac{R\theta^2}{2a} + \delta f - \delta\theta\partial_\theta f - \delta\partial_z f z.\end{aligned}$$

The contact angle boundary condition is

$$\frac{R^2\theta^2}{2a^2} + f + \sqrt{a^2 - b^2}\hat{\boldsymbol{n}} \cdot \nabla f + O(\delta) = 0, \tag{3.21}$$

with the outward normal defined as $\hat{\boldsymbol{n}} = -\dfrac{R\theta\hat{\boldsymbol{\theta}} + z\hat{\boldsymbol{z}}}{\sqrt{a^2 - b^2}}$ and $\nabla \equiv \dfrac{\hat{\boldsymbol{\theta}}}{R}\partial_\theta + \hat{\boldsymbol{z}}\partial_z$.

3.3 Numerical solution of cylindrical interface

The Helmholtz equation 3.13 can be solved numerically with contact angle boundary condition 3.21. The MATLAB Partial Differential Equation (PDE) Toolbox (MathWorks Inc.) is used for a finite element approach. The cylinder was set with finite length L and radius $R = 1$, a quarter of which ($\theta \in [0, \pi]$, $z \in \left[0, \frac{L}{2}\right]$) was

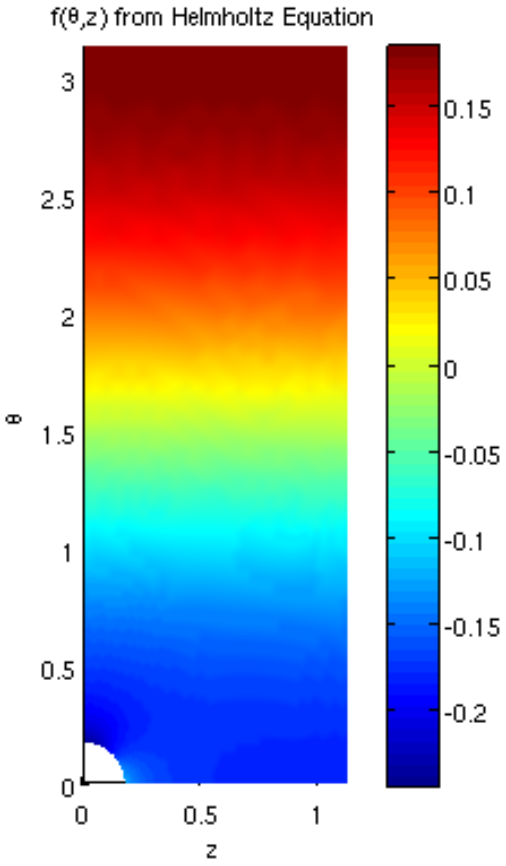

Figure 3.5: Numerical solution to Helmholtz equation.

unfolded and studied. The boundary conditions were all set as reflecting $\hat{\boldsymbol{n}} \cdot \nabla f = 0$ except at contact where Equation 3.21 was applied. In the following plots, the parameters were set as $a = .2$, $L = 2.25$ and $\theta_c = \frac{2\pi}{3}$. The generated triangular mesh consists over 1000 grid points and the shading was interpolated to desired resolution. Further refinement of meshes did not produce a much different color map.

At first we need to verify the assumption on the order of ∇f in the derivation of contact angle boundary condition 3.21. It is shown in Figure 3.5 and 3.6 that $f \sim a\nabla f \sim O(1)$ *at contact*. The leading terms in Equation 3.21 are also $O(1)$ at contact.

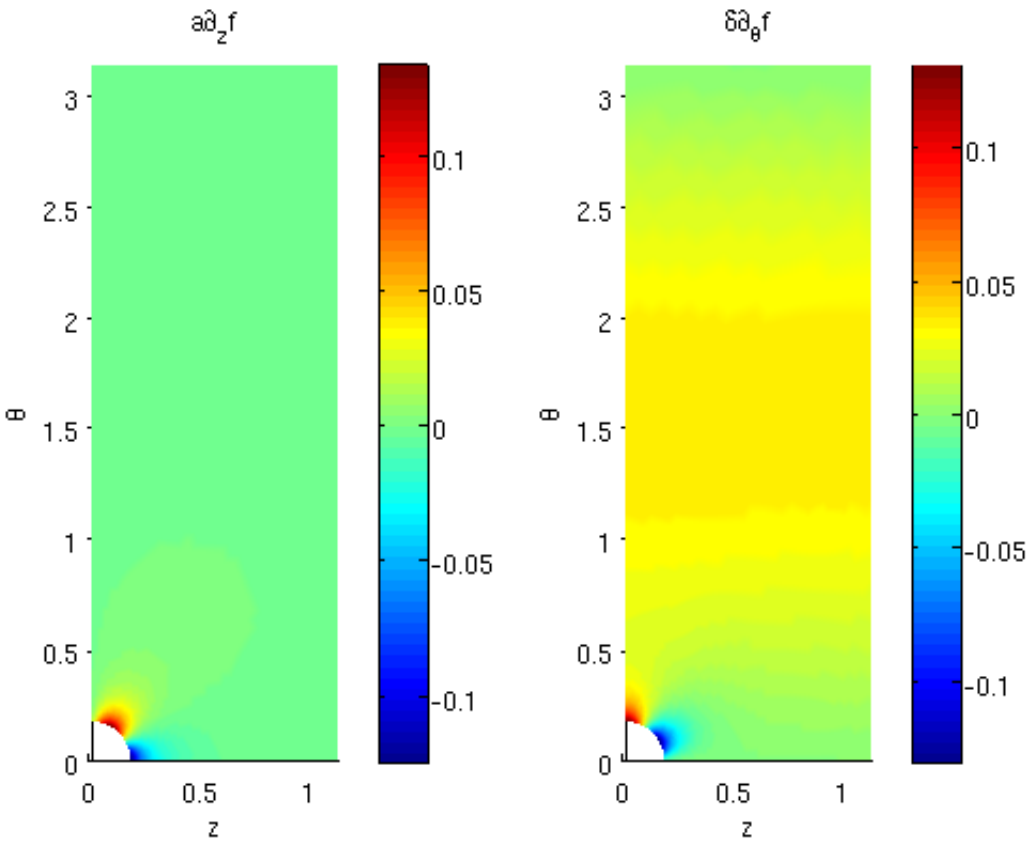

(a) (b)

Figure 3.6: Rescaled gradient of numerical solution $f(\theta, z)$. The two components of ∇f were shown in (a) and (b) respectively.

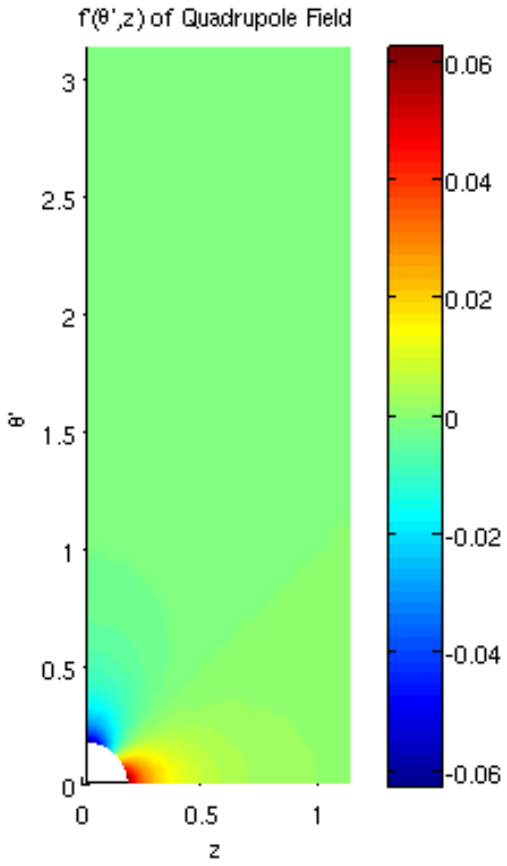

Figure 3.7: Quadrupole field summed with images (Equation 3.11).

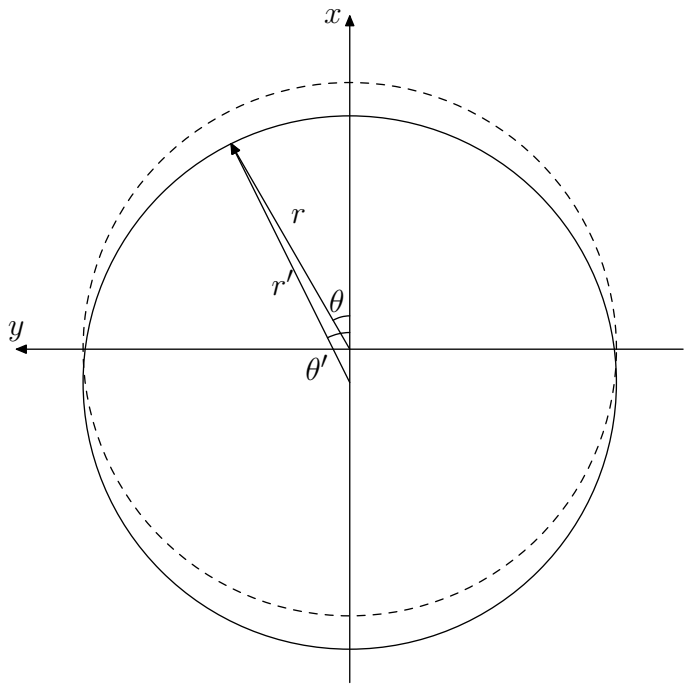

Figure 3.8: Cross-section of shifted cylinder.

The summed quadrupole field (Equation 3.11), which was obtained from the solution of the Poissons equation (Section 3.1), is plotted for comparison in Figure 3.7. This is obviously *not* the same as the solution in Figure 3.5. The difference comes from the shift term in Equation 3.5 and the subtlety of fixing the particle at $x = R + b$ (Equation 3.14). The problem with solution f in Figure 3.5 is that it does not vanish far away from contact. Instead, we find a leading term of $-\cos\theta$, implying a translation along $-\hat{\boldsymbol{x}}$ direction (Figure 3.8). The quadrupole field was actually obtained in another coordinate (θ', z) (Figure 3.8), with the origin at $\left(x = -\dfrac{a^2 \sin^2\theta_c}{4R}, y = 0, z = 0\right)$:

$$r' = R + \frac{a^4 \sin^4\theta_c}{24R^3} \frac{\cosh\dfrac{z}{R}\cos\theta' - 1}{\left(\cosh\dfrac{z}{R} - \cos\theta'\right)^2}. \tag{3.22}$$

With the shift defined, the relationship between r', θ' and r, θ is

$$r' \cos\theta' = r\cos\theta + \frac{a^2 \sin^2\theta_c}{4R}, \tag{3.23}$$

$$r' \sin\theta' = r\sin\theta, \tag{3.24}$$

while z is unchanged.

Far from contact ($\theta, \frac{z}{R} \sim O(1)$), the order of quadrupole perturbation in Equation 3.22 is negligible ($f \sim O(\delta^2)$). In this case one can solve Equations 3.22, 3.23, 3.24 for $r(\theta)$ and get the $O(1)$ term of f. It is just

$$f = -\frac{1}{4}\sin^2\theta_c \cos\theta, \tag{3.25}$$

as one can check with Figure 3.5. It is easy to verify that this is actually an analytical solution to the Helmholtz equation 3.13.

As shown in Figure 3.9, the solution to Helmholtz equation was transformed to the coordinate (θ', z) and compared with summed quadrupole field. Similar to f, f' is defined as

$$r' = R + \frac{a^2}{R} f'. \tag{3.26}$$

The difference between quadrupole field $f'_Q(\theta', z)$ and shifted solution $f'_H(\theta', z)$ is shown in Figure 3.9b. The difference is much smaller than 1. But the pattern of $\Delta f'$ shows a trend of $-\cos\theta'$, which implies a higher order correction to the value of shift $-\frac{a^2 \sin^2\theta_c}{4R}$.

3.4 Analytical solution for cylindrical interface

In this section we solve the Helmholtz equation 3.13 directly for the deformation of cylindrical interface upon adsorption of spherical particle. We have to solve it in a strip ($\theta \in [-\pi, \pi]$, $\tilde{z} \in (-\infty, \infty)$) with the boundary conditions summarized in Figure 3.10. The periodic boundary condition along θ implies the reflective condition on $\theta = \pi$. We first solve this equation on an infinite domain and then we use the

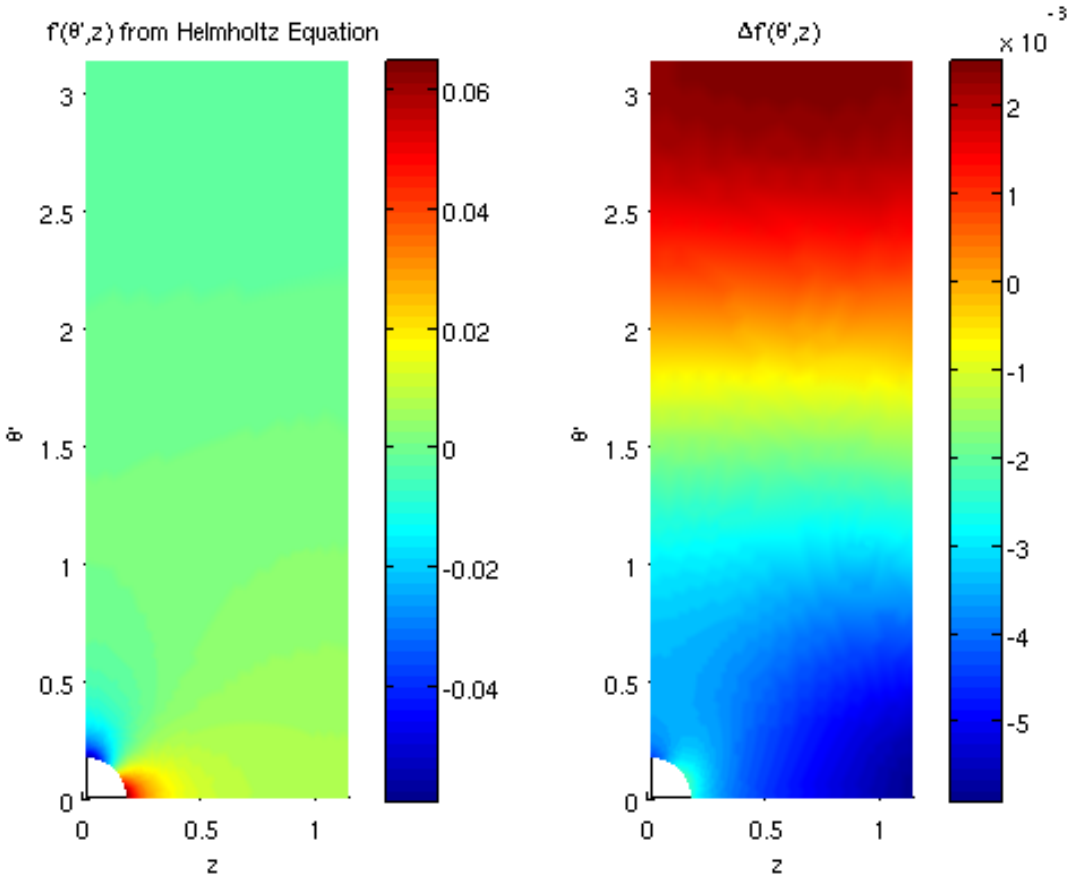

(a) (b)

Figure 3.9: Solution to Helmholtz equation shifted and compared with quadrupole field. ($\Delta f' = f'_Q - f'_H$.)

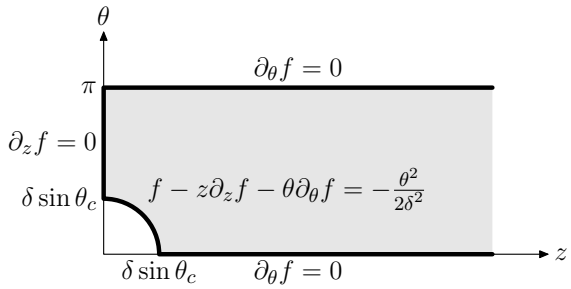

Figure 3.10: Boundary conditions for the Helmholtz equation 3.13. The first quadrant of $z\theta$ coordinate system is flattened and shown. The particle is positioned at the origin. The contact line approximates to a ring with radius $a \sin\theta_c$. As described in the text, the boundary condition at contact is obtained from the contact angle constraint. The boundary conditions at $\tilde{z} = 0$, $\theta = 0$ and $\theta = \pi$ are determined by the mirror symmetries.

images method to find a solution which satisfies the boundary condition $\partial_\theta f(\tilde{z}, \pm\pi) = 0$.

3.4.1 General form of solution

We use polar coordinates:

$$\tilde{z} = \rho \cos\phi, \tag{3.27}$$

$$\theta = \rho \sin\phi. \tag{3.28}$$

The PDE to solve is now

$$\left(\partial^2_{\rho,\rho} + \frac{1}{\rho}\partial_\rho + \frac{1}{\rho^2}\partial^2_{\phi,\phi}\right) f(\rho, \phi) = -f(\rho, \phi), \tag{3.29}$$

with boundary conditions

$$f(\phi + 2\pi, \rho) = f(\phi, \rho), \tag{3.30}$$

$$f(-\phi, \rho) = f(\phi, \rho), \tag{3.31}$$

$$f(\pi - \phi, \rho) = f(\phi, \rho). \tag{3.32}$$

The expression of the contact line is

$$\rho = \rho^* \equiv \delta \sin\theta_c. \tag{3.33}$$

The boundary condition along the contact line 3.33 is

$$f(\rho^*, \phi) - \rho^* \, \partial_\rho f(\rho, \phi)|_{\rho=\rho^*} = -\frac{1}{2}\frac{\rho^{*2}}{\delta^2}\sin^2\phi + O(\delta). \tag{3.34}$$

Separate variables:

$$f(\rho, \phi) = g(\rho)h(\phi). \tag{3.35}$$

The PDE becomes

$$\frac{\rho g'(\rho)}{g(\rho)} + \frac{\rho^2 g''(\rho)}{g(\rho)} + \rho^2 = -\frac{h''(\phi)}{h(\phi)}. \tag{3.36}$$

We have

$$h''(\phi) = -k^2 h(\phi) \tag{3.37}$$

with separation constant $k > 0$. The general solution for h is a linear combination of trigonometric functions. The symmetry condition of the problem further requires

$$h(\phi) = \sum_k \alpha_k \cos k\phi, \tag{3.38}$$

with $k = 0, 2, 4 \ldots$. The equation for g is then a Bessel differential equation

$$\rho^2 g'' + \rho g' + (\rho^2 - k^2)g = 0. \tag{3.39}$$

The canonical solutions of this equation are Bessel functions $J_k(\rho)$ and $Y_k(\rho)$. The complete solution so far is

$$f(\rho, \phi) = \sum_{k=0}^{\infty} [\alpha_k J_{2k}(\rho) + \beta_k Y_{2k}(\rho)] \cos 2k\phi. \tag{3.40}$$

As explained in Chapter 3, there could be a vertical shift $\cos\theta$ in f due to the subtlety of fixing the particle at $x = R + b$ (Equation 3.14). Explicitly [78],

$$f(\rho,\phi) = \alpha\left[J_0(\rho) + 2\sum_{k=1}^{\infty} J_{2k}(\rho)\cos 2k\phi\right] + \sum_{k=0}^{\infty}\left[\alpha_k J_{2k}(\rho) + \beta_k Y_{2k}(\rho)\right]\cos 2k\phi, \tag{3.41}$$

$$= \alpha\cos(\rho\sin\phi) + \sum_{k=0}^{\infty}\left[\alpha_k J_{2k}(\rho) + \beta_k Y_{2k}(\rho)\right]\cos 2k\phi, \tag{3.42}$$

with the term with the coefficient α is a shift. We need now to choose α such that the energy is minimized, *i.e.*, the interface is deformed as little as possible.

Part of the remaining coefficients are fixed by Equation 3.34. We have

$$\begin{aligned}
&\alpha\left[J_0(\rho^*) + 2\sum_{k=1}^{\infty} J_{2k}(\rho^*)\cos 2k\phi\right] \\
-&\alpha\rho^*\left[J_0'(\rho^*) + 2\sum_{k=1}^{\infty} J_{2k}'(\rho^*)\cos 2k\phi\right] \\
+&\sum_{k=0}^{\infty}\left[\alpha_k J_{2k}(\rho^*) + \beta_k Y_{2k}(\rho^*)\right]\cos 2k\phi \\
-&\rho^*\sum_{k=0}^{\infty}\left[\alpha_k J_{2k}'(\rho^*) + \beta_k Y_{2k}'(\rho^*)\right]\cos 2k\phi = -\frac{1}{4}\sin^2\theta_c(1-\cos 2\phi).
\end{aligned} \tag{3.43}$$

The coefficients for $\cos 2k\phi$ should balance for all k, because of orthogonality

$$\frac{1}{\pi}\int_0^{2\pi}\cos 2m\phi\cos 2n\phi \mathrm{d}\phi = \delta_{m,n}. \tag{3.44}$$

So

$$(\alpha_0+\alpha)\left[J_0(\rho^*) - \rho^* J_0'(\rho^*)\right] + \beta_0\left[Y_0(\rho^*) - \rho^* Y_0'(\rho^*)\right] = -\frac{1}{4}\sin^2\theta_c, \tag{3.45}$$

$$(\alpha_1+2\alpha)\left[J_2(\rho^*) - \rho^* J_2'(\rho^*)\right] + \beta_1\left[Y_2(\rho^*) - \rho^* Y_2'(\rho^*)\right] = \frac{1}{4}\sin^2\theta_c, \tag{3.46}$$

$$(\alpha_k+2\alpha)\left[J_{2k}(\rho^*) - \rho^* J_{2k}'(\rho^*)\right] + \beta_k\left[Y_{2k}(\rho^*) - \rho^* Y_{2k}'(\rho^*)\right] = 0, \quad k \geq 2. \tag{3.47}$$

The asymptotic behavior as $\rho^* \to 0$ is

$$\alpha_0 + \alpha + \frac{2\beta_0}{\pi}\left(\gamma_E - \ln 2 - 1 + \ln \rho^*\right) = -\frac{1}{4}\sin^2\theta_c, \tag{3.48}$$

$$-\frac{1}{8}\left(\alpha_1 + 2\alpha\right)\rho^{*2} - \frac{12\beta_1}{\pi\rho^{*2}} = \frac{1}{4}\sin^2\theta_c, \tag{3.49}$$

$$\frac{(1-2k)\left[\alpha_k + 2\alpha\right]\rho^{*2k}}{(2k)!4^k} - \frac{4^k(2k+1)\Gamma(2k)\beta_k}{\pi\rho^{*2k}} = 0. \tag{3.50}$$

Setting $\alpha_k = \beta_k = 0$ $(k \neq 1)$ to reduce deformation of the interface[2], we have

$$\alpha = -\frac{1}{4}\sin^2\theta_c, \tag{3.51}$$

$$\frac{\pi\alpha_1\rho^{*4}}{96} + \beta_1 = -\frac{\pi}{48}\delta^2\sin^4\theta_c. \tag{3.52}$$

The solution so far is

$$f(\rho,\phi) = \alpha\cos(\rho\sin\phi) + \left[\alpha_1 J_2(\rho) + \beta_1 Y_2(\rho)\right]\cos 2\phi. \tag{3.53}$$

This solution reflects the quadrupolar symmetry of the system. In fact, the short-range ($\rho \to 0$) asymptotics of $f(\rho,\phi)$ is proportional to the quadrupole deformation obtained in Section 3.1. In order to satisfy the condition of periodicity and continuity about θ, we apply method of images in the following section. The coefficients α_1 and β_1 will be determined by enforcing the convergence of sum over images.

3.4.2 Method of images

Denote the quadrupolar deformation as

$$f_Q(\tilde{z},\theta) = \left[\alpha_1 J_2(\rho) + \beta_1 Y_2(\rho)\right]\cos 2\phi. \tag{3.54}$$

[2] $\alpha_k = \beta_k$ $(k \neq 1)$ is also required for the convergence of the summation over images as described in the following sections.

The function f_{strip} that satisfy the boundary conditions along the borders of the strip (Figure 3.10) is then

$$f_{\text{strip}}(\tilde{z},\theta) = \alpha\cos\theta + \sum_{n=-\infty}^{\infty} f_Q(\tilde{z},\theta+2n\pi), \tag{3.55}$$

$$= \alpha\cos\theta + f_Q(\tilde{z},\theta) + \sum_{n=1}^{\infty}\left[f_Q(\tilde{z},\theta+2n\pi) + f_Q(\tilde{z},\theta-2n\pi)\right]. \tag{3.56}$$

We need to examine the asymptotics of $f_Q(\tilde{z},\theta+2n\pi) + f_Q(\tilde{z},\theta-2n\pi)$ for large n. Define

$$\rho_n = \sqrt{(\theta+2n\pi)^2+\tilde{z}^2}, \tag{3.57}$$

$$\phi_n = \arctan\frac{\theta+2n\pi}{\tilde{z}}. \tag{3.58}$$

Without loss of generality, look at the quadrant of $\theta\in[0,\pi]$, $\tilde{z}\in(0,\infty)$. Then

$$\rho_n = 2|n|\pi + \frac{|n|}{n}\theta + O\left(\frac{1}{n^2}\right), \tag{3.59}$$

$$\phi_n = \frac{\pi}{2} - \frac{\tilde{z}}{2n\pi} + O\left(\frac{1}{n^2}\right). \tag{3.60}$$

Expand the Bessel functions as power series:

$$J_2(\rho_n) = \frac{1}{\sqrt{|n|}\pi}\cos\left(\frac{|n|}{n}\theta+\pi+\frac{\pi}{4}\right) + O\left(\frac{1}{|n|^{\frac{3}{2}}}\right), \tag{3.61}$$

$$= \frac{1}{\sqrt{2|n|}\pi}\left(-\cos\frac{|n|}{n}\theta + \sin\frac{|n|}{n}\theta\right) + O\left(\frac{1}{|n|^{\frac{3}{2}}}\right). \tag{3.62}$$

$$Y_2(\rho_n) = -\frac{1}{\sqrt{|n|}\pi}\sin\left(\frac{|n|}{n}\theta+\pi+\frac{\pi}{4}\right) + O\left(\frac{1}{|n|^{\frac{3}{2}}}\right), \tag{3.63}$$

$$= \frac{1}{\sqrt{2|n|}\pi}\left(\cos\frac{|n|}{n}\theta + \sin\frac{|n|}{n}\theta\right) + O\left(\frac{1}{|n|^{\frac{3}{2}}}\right). \tag{3.64}$$

Then

$$f_Q(\tilde{z}, \theta + 2n\pi) = \frac{1}{\sqrt{2|n|}\pi}\left[(-\alpha_1 + \beta_1)\cos\frac{|n|}{n}\theta + (\alpha_1 + \beta_1)\sin\frac{|n|}{n}\theta\right] + O\left(\frac{1}{|n|^{\frac{3}{2}}}\right). \tag{3.65}$$

Now for $n > 0$:

$$f_Q(\tilde{z}, \theta + 2n\pi) + f_Q(\tilde{z}, \theta - 2n\pi) = \frac{\sqrt{2}}{\pi}\frac{1}{\sqrt{n}}(\beta_1 - \alpha_1)\cos\theta + O\left(\frac{1}{n^{\frac{3}{2}}}\right). \tag{3.66}$$

Since the sum $\sum_{n=1}^{\infty}\frac{1}{\sqrt{n}}$ diverges, we need

$$\alpha_1 = \beta_1. \tag{3.67}$$

Now from Equation 3.52 and 3.67, we have

$$\alpha_1 = \beta_1 = -\frac{\pi}{48}\delta^2\sin^4\theta_c. \tag{3.68}$$

The final solution to the Helmholtz equation is

$$f = \alpha\cos\theta + \beta\sum_{n=-\infty}^{\infty}\left[J_2(\rho_n) + Y_2(\rho_n)\right]\cos 2\phi_n, \tag{3.69}$$

where

$$\alpha = -\frac{1}{4}\sin^2\theta_c, \tag{3.70}$$

$$\beta = -\frac{\pi}{48}\delta^2\sin^4\theta_c. \tag{3.71}$$

With the asymptotic forms of the Bessel functions for small arguments, the solution above agrees with the quadrupole deformation obtained in Section 3.1. For $\tilde{z}$ and θ of order $O(1)$, the summation of series is approximated numerically in the next section.

3.4.3 Summation of series

For given $\tilde{z}$ and θ, the sum to be approximated is:

$$S = s_0 + \sum_{n=1}^{\infty} \left(s_n + s_{-n} \right), \tag{3.72}$$

where

$$s_n = \left[J_2\left(\rho_n\right) + Y_2\left(\rho_n\right) \right] \cos 2\phi_n. \tag{3.73}$$

A numerical summation was done by computing a partial sum directly and approximating the remainder as follows.

In the limit of large n, a Taylor expansion yields

$$s_n + s_{-n} = \frac{A(\tilde{z},\theta)}{n^{\frac{3}{2}}} + \frac{B(\tilde{z},\theta)}{n^{\frac{7}{2}}} + O\left(\frac{1}{n^{\frac{9}{2}}}\right), \tag{3.74}$$

where

$$A(\tilde{z},\theta) = \frac{4\theta \sin\theta - (4\tilde{z}^2 + 15)\cos\theta}{4\sqrt{2}\pi^2}, \tag{3.75}$$

$$\begin{aligned} B(\tilde{z},\theta) = \frac{1}{6144\sqrt{2}\pi^4} \Big\{ \left[4\tilde{z}^2 \left(16\tilde{z}^4 + 1140\tilde{z}^2 + 4275 \right) - 720\theta^2 \left(4\tilde{z}^2 + 15 \right) - 945 \right] \cos\theta \\ -60\theta \left(16\tilde{z}^4 + 408\tilde{z}^2 - 16\theta^2 + 105 \right) \sin\theta \Big\}. \end{aligned} \tag{3.76}$$

The order of the leading term ($n^{-\frac{3}{2}}$) follows from Equation 3.66. For sufficiently large n,

$$s_n + s_{-n} \approx \frac{A(\tilde{z},\theta)}{n^{\frac{3}{2}}}, \tag{3.77}$$

which requires

$$n^2 \gg \left| \frac{B}{A} \right|. \tag{3.78}$$

Now the approximation is

$$S \approx s_0 + \sum_{n=1}^{N} \left(s_n + s_{-n} - \frac{A}{n^{\frac{3}{2}}} \right) + A\zeta\left(\frac{3}{2}\right) \tag{3.79}$$

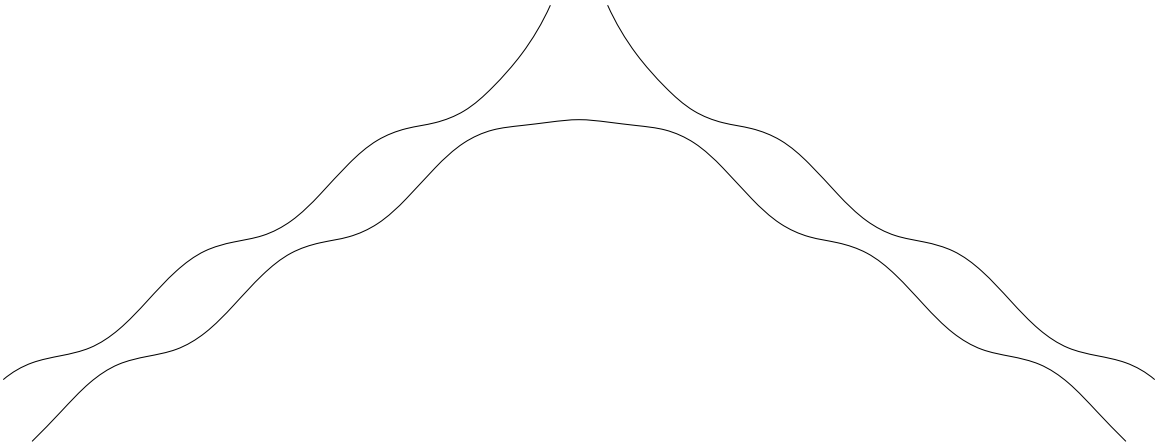

Figure 3.11: Cylinder perturbed upon adsorption of solid particle, with deformation exaggerated. To make the illustration more realistic, the actual perturbation and the angle of distortion should be reduced by a factor of $\pi\delta^4 \sin^4\theta_c/48$. The particle is not drawn.

with $\zeta(x)$ the Riemann zeta function.

The sum was computed at different points (~ 10000) in the $\tilde{z}\theta$-plane and the data showed the leading modes of S correspond to a kink followed with an undulation (Figure 3.11):

$$S = .6371\,|\tilde{z}|\cos\theta - .4502\cos\left(|\tilde{z}| - \frac{\pi}{4}\right) + \xi(\tilde{z},\theta). \tag{3.80}$$

The equation above was obtained by fitting data in the quadrant of positive $\tilde{z}$ and θ. The remainder $\xi(\tilde{z},\theta)$ decays approximately as $1/\tilde{z}^2$. The symmetry condition was shown by taking explicitly the absolute values of $\tilde{z}$ and θ. Note that the wavelength of the undulation corresponds to the zero mode of the Rayleigh instability [8].

As a summary to this chapter, we showed that the cylindrical interface is deformed by adsorbed spherical particle. We solved the deformation to the leading order, which has a quadrupolar symmetry and decays $1/r^2$ near the three-phase contact line. The next chapters consider energies and forces arising from the deformation, respectively.

CHAPTER 4

ADSORPTION ENERGY FOR CYLINDRICAL INTERFACE

With the particle partially immersed in the perturbed interface, the change of energy corresponding to the adsorption can be evaluated and compared with the case of a planar interface (Section 1.2). The parametrization of the interface is given by

$$\tilde{\mathbf{r}} = [\tilde{r}(\tilde{z},\theta)\cos\theta, \tilde{r}(\tilde{z},\theta)\sin\theta, \tilde{z}] \tag{4.1}$$

with

$$\tilde{r}(\tilde{z},\theta) \equiv \frac{r(\tilde{z},\theta)}{R} = 1 + \delta^2 f(\tilde{z},\theta). \tag{4.2}$$

The adsorption energy can be separated into two parts. In the short-range, the contribution of near-field deformation is calculated analytically in Section 4.1. In the long-range, the change of interfacial area will be estimated numerically in Section 4.2.

4.1 Near-field contribution

4.1.1 Area of fluid interface

We use polar coordinates

$$\tilde{z} = \rho\cos\phi, \tag{4.3}$$

$$\theta = \rho\sin\phi. \tag{4.4}$$

---

[0]Contributions: Anthony D. Dinsmore and Benny Davidovitch conducted the study. Chuan Zeng calculated the interfacial energies.

The contact line can be characterized as $\rho_c(\phi)$ with leading term $\delta \sin\theta_c$. The area of the perturbed cylinder is given by

$$\tilde{A} \equiv \frac{A}{R^2} = \int \mathrm{d}\phi \int \mathrm{d}\rho \left|\partial_\rho \mathbf{r} \times \partial_\phi \mathbf{r}\right|. \tag{4.5}$$

From the solution 3.69, the interface close to contact line can be well approximated in Cartesian coordinates as the near-field deformation:

$$\begin{aligned}\tilde{x} =& 1 - \frac{1}{2}\tilde{y}^2 - \frac{1}{4}\rho^{*2} - \frac{\pi}{48}\rho^{*4}\left[J_2(\rho) + Y_2(\rho)\right]\frac{\tilde{z}^2 - \tilde{y}^2}{\tilde{z}^2 + \tilde{y}^2}, &(4.6)\\ =& 1 - \frac{1}{2}\tilde{y}^2 - \frac{1}{4}\rho^{*2} + \frac{\rho^{*4}\left(\tilde{z}^2 - \tilde{y}^2\right)}{12\left(\tilde{z}^2 + \tilde{y}^2\right)^2} + O\left(\delta^4\right), &(4.7)\end{aligned}$$

where $\rho = \sqrt{\tilde{y}^2 + \tilde{z}^2}$, $\rho^* = \delta \sin\theta_c$ and $\tilde{z}, \tilde{y} \sim O(\delta)$. The origin is defined such that the center of particle is at $(\tilde{x}, \tilde{y}, \tilde{z}) = (1 - \delta\cos\theta_c, 0, 0)$ (Figure 3.2). We parameterize the interface as $(\tilde{x}, \tilde{y}, \tilde{z}) = [\tilde{x}(\rho, \phi), \rho\sin\phi, \rho\cos\phi]$. We have coefficients of the first fundamental form [79]

$$E \equiv \left(\partial_\rho \tilde{x}\right)^2 + \left(\partial_\rho \tilde{y}\right)^2 + \left(\partial_\rho \tilde{z}\right)^2 = \left(\partial_\rho \tilde{x}\right)^2 + \sin^2\phi + \cos^2\phi = 1 + \left(\partial_\rho \tilde{x}\right)^2, \tag{4.8}$$

$$F \equiv \partial_\rho \tilde{x}\partial_\phi \tilde{x} + \partial_\rho \tilde{y}\partial_\phi \tilde{y} + \partial_\rho \tilde{z}\partial_\phi \tilde{z} = \left(\partial_\rho \tilde{x}, \sin\phi, \cos\phi\right)\begin{pmatrix} \partial_\phi \tilde{x} \\ \rho\cos\phi \\ -\rho\sin\phi \end{pmatrix} = \partial_\rho \tilde{x}\partial_\phi \tilde{x}, \tag{4.9}$$

$$G \equiv \left(\partial_\phi \tilde{x}\right)^2 + \left(\partial_\phi \tilde{y}\right)^2 + \left(\partial_\phi \tilde{z}\right)^2 = \rho^2 + \left(\partial_\phi \tilde{x}\right)^2. \tag{4.10}$$

Then

$$\left|\partial_\rho \mathbf{r} \times \partial_\phi \mathbf{r}\right| = \sqrt{EG - F^2} = \sqrt{\rho^2 + \rho^2\left(\partial_\rho \tilde{x}\right)^2 + \left(\partial_\phi \tilde{x}\right)^2}.$$

We now compute the partial derivatives

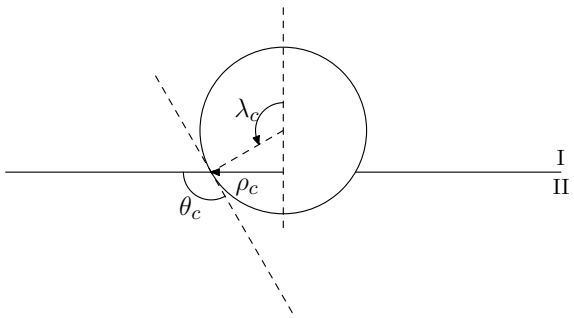

Figure 4.1: Parameterizations of the contact line. Phase I is outside the cylinder and phase II is inside. ρ is the radial coordinate $\sqrt{\tilde{z}^2+\tilde{y}^2}$. λ is the inclination angle measured from the zenith. To the lowest order (flat interface), $\rho_c=\rho^*$, $\lambda_c=\theta_c$.

$$\partial_\rho \tilde{x} = -\frac{1}{2}\rho - \frac{1}{2}\left(\frac{\delta^4 \sin^4\theta_c}{3\rho^3} - \rho\right)\cos 2\phi,$$
$$\partial_\phi \tilde{x} = -\frac{1}{2}\left(\frac{\delta^4 \sin^4\theta_c}{3\rho^2} + \rho^2\right)\sin 2\phi.$$

Now we obtain

$$\begin{aligned}
EG-F^2 =& \rho^2 + \frac{1}{4}\rho^4 + \frac{1}{2}\rho^2\left(\frac{\rho^{*4}}{3\rho^2} - \rho^2\right)\cos 2\phi + \frac{1}{4}\left(\frac{\rho^{*8}}{9\rho^4} + \rho^4\right) - \frac{1}{6}\rho^{*4}\cos 4\phi \\
\frac{1}{\rho}\sqrt{EG-F^2} =& 1 + \frac{1}{8}\rho^2 + \frac{1}{4}\left(\frac{\rho^{*4}}{3\rho^2} - \rho^2\right)\cos 2\phi + \frac{1}{8}\left(\frac{\rho^{*8}}{9\rho^6} + \rho^2\right) - \frac{\rho^{*4}\cos 4\phi}{12\rho^2} \\
& + O\left(\delta^4\right) \\
=& 1 + \frac{1}{2}\rho^2\sin^2\phi + \frac{\rho^{*4}\cos 2\phi}{12\rho^2} + \frac{\rho^{*8}}{72\rho^6} - \frac{\rho^{*4}\cos 4\phi}{12\rho^2} + O\left(\delta^4\right).
\end{aligned}$$

For the unperturbed interface $\tilde{x} = -\frac{1}{2}\rho^2\sin^2\phi - \frac{1}{4}\rho^{*2}$,

$$\begin{aligned}
\sqrt{EG-F^2} =& \rho\sqrt{1+\rho^2\sin^2\phi} \\
\frac{1}{\rho}\sqrt{EG-F^2} =& 1 + \frac{1}{2}\rho^2\sin^2\phi + O\left(\delta^4\right).
\end{aligned}$$

The contact line can be projected onto the $\rho\phi$-plane and thus expressed as $\rho_c = \rho_c(\phi)$ (Figure 4.1). The change of interfacial area is

$$\Delta\tilde{A}_{\mathrm{I/II}} = \int_0^{2\pi} \mathrm{d}\phi \int_{\rho_c}^{\rho_m} \mathrm{d}\rho\rho \left(\frac{\rho^{*4}\cos 2\phi}{12\rho^2} + \frac{\rho^{*8}}{72\rho^6} - \frac{\rho^{*4}\cos 4\phi}{12\rho^2} \right) - \int_0^{2\pi} \mathrm{d}\phi \int_0^{\rho_c} \mathrm{d}\rho\rho \left(1 + \frac{1}{2}\rho^2 \sin^2\phi \right). \tag{4.11}$$

We define ρ_m as the boundary between near and far field. We choose ρ_m so that $\delta \ll \rho_m \ll 1$. The integrand of the first integral is of order $O(\delta^2)$, the integral of which would give $O(\delta^4)$. Plugging in the leading term of ρ_c:

$$\int_0^{2\pi} \mathrm{d}\phi \int_{\rho_c}^{\rho_m} \mathrm{d}\rho\rho \left(\frac{\rho^{*4}\cos 2\phi}{12\rho^2} + \frac{\rho^{*8}}{72\rho^6} - \frac{\rho^{*4}\cos 4\phi}{12\rho^2} \right) \tag{4.12}$$

$$= \int_0^{2\pi} \mathrm{d}\phi \int_{\delta_c}^{\rho_m} \mathrm{d}\rho\rho \left(\frac{\rho^{*4}\cos 2\phi}{12\rho^2} + \frac{\rho^{*8}}{72\rho^6} - \frac{\rho^{*4}\cos 4\phi}{12\rho^2} \right) \tag{4.13}$$

$$= \int_{\delta_c}^{\rho_m} \rho \mathrm{d}\rho \int_0^{2\pi} \mathrm{d}\phi \left(\frac{\rho^{*4}\cos 2\phi}{12\rho^2} + \frac{\rho^{*8}}{72\rho^6} - \frac{\rho^{*4}\cos 4\phi}{12\rho^2} \right) \tag{4.14}$$

$$= \int_{\delta_c}^{\rho_m} \rho \mathrm{d}\rho \int_0^{2\pi} \mathrm{d}\phi \frac{\rho^{*8}}{72\rho^6} \tag{4.15}$$

$$= \frac{\pi\rho^{*4}}{144} - \frac{\pi\rho^{*8}}{144\rho_m^4} \tag{4.16}$$

$$= \frac{\pi\rho^{*4}}{144} + O\left(\frac{\delta^8}{\rho_m^4} \right). \tag{4.17}$$

Similarly, the other integral

$$- \int_0^{2\pi} \mathrm{d}\phi \int_0^{\rho_c} \mathrm{d}\rho\rho \left(1 + \frac{1}{2}\rho^2 \sin^2\phi \right) \tag{4.18}$$

$$= -\frac{1}{2} \int_0^{2\pi} \mathrm{d}\phi \left(\rho_c^2 + \frac{1}{4}\rho_c^4 \sin^2\phi \right), \tag{4.19}$$

$$= -\frac{1}{8}\pi\rho^{*4} - \frac{1}{2} \int_0^{2\pi} \mathrm{d}\phi \rho_c^2. \tag{4.20}$$

Now

$$\Delta\tilde{A}_{\mathrm{I/II}} = \frac{\pi\rho^{*4}}{144} - \frac{1}{8}\pi\rho^{*4} - \frac{1}{2} \int_0^{2\pi} \mathrm{d}\phi \rho_c^2. \tag{4.21}$$

We need to solve the following equation for $\rho_c(\phi)$:

$$(\tilde{x} - 1 + \delta\cos\theta_c)^2 + \rho_c^2 = \delta^2$$

$$\left(-\frac{1}{2}\rho_c^2\sin^2\phi - \frac{1}{4}\rho^{*2} + \frac{\rho^{*4}\cos 2\phi}{12\rho_c^2} + \delta\cos\theta_c\right)^2 + \rho_c^2 = \delta^2. \tag{4.22}$$

Rearranging, we obtain ρ_c^2 up to $O(\delta^4)$:

$$\rho_c^2 = \delta_c^2 + \delta\cos\theta_c\left(\rho^{*2}\sin^2\phi + \frac{1}{2}\rho^{*2} - \frac{1}{6}\rho^{*2}\cos 2\phi\right) + O\left(\delta^4\right) \tag{4.23}$$

$$= \rho^{*2} + \delta\rho^{*2}\left(1 - \frac{2}{3}\cos 2\phi\right)\cos\theta_c + O\left(\delta^4\right). \tag{4.24}$$

$$\rho_c^2 = \delta^2 - \left[\frac{1}{4}\left(1 - \cos 2\phi\right)\rho_c^2 + \frac{1}{4}\rho^{*2} - \delta\cos\theta_c - \frac{\rho^{*4}\cos 2\phi}{12\rho_c^2}\right]$$

$$= \delta^2 - \rho^{*4}\left[-\frac{\delta\cos\theta_c}{\rho^{*2}} + \frac{1}{2} - \frac{\cos 2\phi}{3} + \frac{1}{4}\left(1 - \frac{2}{3}\cos 2\phi\right)^2\delta\cos\theta_c\right]^2 + O\left(\delta^5\right) \tag{4.25}$$

$$= \rho^{*2} + \delta\rho^{*2}\left(1 - \frac{2}{3}\cos 2\phi\right)\cos\theta_c - \frac{1}{4}\rho^{*4}\left(1 - \frac{2}{3}\cos 2\phi\right)^2$$
$$+ \frac{1}{2}\rho^{*2}\delta^2\cos^2\theta_c\left(1 - \frac{2}{3}\cos 2\phi\right)^2 + O\left(\delta^5\right) \tag{4.26}$$

$$= \rho^{*2} + \delta\rho^{*2}\left(1 - \frac{2}{3}\cos 2\phi\right)\cos\theta_c + \frac{1}{4}\rho^{*2}\left(2\delta^2\cos^2\theta_c - \rho^{*2}\right)\left(1 - \frac{2}{3}\cos 2\phi\right)^2$$
$$+ O\left(\delta^5\right). \tag{4.27}$$

Following Equation 4.21, the change of interfacial area is

$$\Delta\tilde{A}_{\mathrm{I/II}} = \frac{\pi\rho^{*4}}{144} - \frac{1}{8}\pi\rho^{*4} - \pi\rho^{*2} - \pi\rho^{*2}\delta\cos\theta_c - \frac{1}{4}\pi\rho^{*2}\left(2\delta^2\cos^2\theta_c - \rho^{*2}\right)$$
$$- \frac{1}{18}\pi\rho^{*2}\left(2\delta^2\cos^2\theta_c - \rho^{*2}\right) + O\left(\delta^5\right) \tag{4.28}$$

$$= -\pi\rho^{*2} - \pi\rho^{*2}\delta\cos\theta_c + \frac{3}{16}\pi\rho^{*4} - \frac{11}{18}\pi\rho^{*2}\delta^2\cos^2\theta_c + O\left(\delta^5\right). \tag{4.29}$$

4.1.2 Area of particle surface outside the cylinder

On the surface of particle, the inclination angle of contact line λ_c is a function of ϕ (Figure 4.1). We have $(\tilde{x}, \tilde{y}, \tilde{z}) = (1 - \delta\cos\theta_c + \delta\cos\lambda, \delta\sin\lambda\sin\phi, \delta\sin\lambda\cos\phi)$. From Equation 4.7, solve for $\cos\lambda_c(\phi)$ up to $O(\delta^2)$:

$$\delta\cos\lambda_c = -\frac{1}{2}\delta^2\sin^2\lambda_c\sin^2\phi - \frac{1}{4}\rho^{*2} + \delta\cos\theta_c + \frac{\rho^{*4}\cos 2\phi}{12\delta^2\sin^2\lambda_c} \tag{4.30}$$

$$\cos\lambda_c = -\frac{1}{4}\delta\sin^2\lambda_c + \frac{1}{4}\delta\sin^2\lambda_c\cos 2\phi - \frac{\rho^{*2}}{4\delta} + \cos\theta_c + \frac{\rho^{*4}\cos 2\phi}{12\delta^3\sin^2\lambda_c} \tag{4.31}$$

$$= -\frac{1}{4}\delta(1-\cos 2\phi)\left(1-\cos^2\lambda_c\right) - \frac{\rho^{*2}}{4\delta} + \cos\theta_c + \frac{\rho^{*4}\cos 2\phi}{12\delta^3\left(1-\cos^2\lambda_c\right)} \tag{4.32}$$

$$= -\frac{\rho^{*2}}{4\delta}(1-\cos 2\phi) - \frac{\rho^{*2}}{4\delta} + \cos\theta_c + \frac{\rho^{*2}\cos 2\phi}{12\delta} + O\left(\delta^2\right). \tag{4.33}$$

Then

$$\cos^2\lambda_c = \cos^2\theta_c - \left[\frac{\rho^{*2}}{2\delta}(1-\cos 2\phi) + \frac{\rho^{*2}}{2\delta} - \frac{\rho^{*2}\cos 2\phi}{6\delta}\right]\cos\theta_c + O\left(\delta^2\right) \tag{4.34}$$

$$= \cos^2\theta_c - \frac{\rho^{*2}\cos\theta_c}{\delta}\left(1 - \frac{2}{3}\cos 2\phi\right) + O\left(\delta^2\right). \tag{4.35}$$

Plug Equation 4.35 into Equation 4.32:

$$\begin{aligned}\cos\lambda_c = &-\frac{1}{4}\delta\sin^2\theta_c + \frac{1}{4}\delta\sin^2\theta_c\cos 2\phi - \frac{\rho^{*2}}{4\delta} + \cos\theta_c \\ &+ \frac{\rho^{*4}\cos 2\phi}{12\delta^3\left[1-\cos^2\theta_c + \frac{\rho^{*2}\cos\theta_c}{\delta}\left(1-\frac{2}{3}\cos 2\phi\right)\right]} \\ &- \frac{1}{4}(1-\cos 2\phi)\left(1-\frac{2}{3}\cos 2\phi\right)\rho^{*2}\cos\theta_c + O\left(\delta^3\right)\end{aligned} \tag{4.36}$$

$$\begin{aligned}= &-\frac{1}{4}\left(2-\cos 2\phi\right)\delta\sin^2\theta_c + \cos\theta_c + \frac{\rho^{*2}\cos 2\phi}{12\delta}\left[1-\left(1-\frac{2}{3}\cos 2\phi\right)\delta\cos\theta_c\right] \\ &- \frac{1}{4}(1-\cos 2\phi)\left(1-\frac{2}{3}\cos 2\phi\right)\rho^{*2}\cos\theta_c + O\left(\delta^3\right)\end{aligned} \tag{4.37}$$

$$= \cos\theta_c - \frac{1}{2}\left(1-\frac{2}{3}\cos 2\phi\right)\delta\sin^2\theta_c - \frac{1}{4}\left(1-\frac{2}{3}\cos 2\phi\right)^2\rho^{*2}\cos\theta_c + O\left(\delta^3\right). \tag{4.38}$$

Now the area of particle surface outside the cylinder is (Figure 4.1)

$$\tilde{A}_{\mathrm{I}} = \delta^2 \int_0^{2\pi} \mathrm{d}\phi \int_0^{\lambda_c} \sin\lambda \mathrm{d}\lambda \tag{4.39}$$

$$\frac{\tilde{A}_{\mathrm{I}}}{\delta^2} = \int_0^{2\pi} \mathrm{d}\phi \left(1 - \cos\lambda_c\right) \tag{4.40}$$

$$= 2\pi - \int_0^{2\pi} \mathrm{d}\phi \cos\lambda_c \tag{4.41}$$

$$= 2\pi - 2\pi\cos\theta_c + \pi\delta\sin^2\theta_c + \frac{11}{18}\pi\rho^{*2}\cos\theta_c + O\left(\delta^3\right). \tag{4.42}$$

4.1.3 Adsorption energy

Consider the case when a particle is adsorbed to the cylinder from phase I (outside cylinder). Combining Equations 4.29 and 4.42, as well as $\gamma_{\mathrm{I}} - \gamma_{\mathrm{II}} = \gamma\cos\theta_c$:

$$\Delta E = \left(4\pi\delta^2 - \tilde{A}_{\mathrm{I}}\right)\left(\gamma_{\mathrm{II}} - \gamma_{\mathrm{I}}\right)R^2 + \gamma R^2 \Delta\tilde{A}_{\mathrm{I/II}} \tag{4.43}$$

$$= -2\pi\gamma R^2\delta^2\left(1 + \cos\theta_c\right)\cos\theta_c - \pi\gamma R^2\delta^2\sin^2\theta_c + \frac{3}{16}\pi\gamma R^2\delta^4\sin^4\theta_c \tag{4.44}$$

$$= \Delta E_{\mathrm{flat}} + \frac{3}{16}\pi\gamma R^2\delta^4\sin^4\theta_c. \tag{4.45}$$

ΔE_{flat} is negative for any well-defined contact angle. Therefore, if we look at the near vicinity of the particle, the binding is weakened by the curvature of the interface. Compared with $\Delta E_{\mathrm{flat}} \sim \gamma R^2 O\left(\delta^2\right)$, the weakening effect is two orders of magnitude smaller.

4.2 Long-range contribution

With the long-range deformation, the area of interface is

$$\iint R^2 \mathrm{d}\tilde{z}\mathrm{d}\theta \left|\partial_{\tilde{z}}\mathbf{r} \times \partial_\theta \mathbf{r}\right| = \iint R^2 \mathrm{d}\tilde{z}\mathrm{d}\theta \left[1 + \delta^2 f + O\left(\delta^4\right)\right], \tag{4.46}$$

where the integral covers the region $\rho = \sqrt{\tilde{z}^2 + \tilde{y}^2} \geq \rho_m$. The first term 1 in the integrand corresponds to unperturbed cylinder. The leading contribution from the long-range deformation is then

$$\Delta E = \gamma R^2 \delta^2 \iint \mathrm{d}\tilde{z}\mathrm{d}\theta f \tag{4.47}$$

$$= -\frac{\pi}{48}\gamma R^2 \rho^{*4} \iint \mathrm{d}\tilde{z}\mathrm{d}\theta S\left(\tilde{z},\theta\right). \tag{4.48}$$

The sum $S\left(\tilde{z},\theta\right)$ was estimated as Equation 3.80. The first two terms of Equation 3.80 do not contribute to the binding energy. The remainder is denoted as $\xi(\tilde{z},\theta)$. Since the short-range contribution was taken into account as a quadrupole field, it will be subtracted out from $\xi(\tilde{z},\theta)$. Numerical integration shows

$$\int_0^{\pi} \mathrm{d}\theta \left[\xi(\tilde{z},\theta) + \frac{4\cos 2\phi}{\rho^2}\right] \approx \frac{4.196}{10.47 + \tilde{z}^2}. \tag{4.49}$$

Further integration over z would converge. Therefore, the contribution of long-range deformation to the binding energy is of order $\gamma R^2 O\left(\delta^4\right)$, which is the same as that from short-range (Equation 4.45).

To summarize this chapter, we have shown that, for the special case of cylindrical interface, the adsorption energy depends on long-range ($\tilde{z}, \theta \sim O(1)$) deformation as well as short-range ($\tilde{z}, \theta \sim O(\delta)$) deformation. Then it is not determined by the local curvatures alone.

However, the long-range contribution to energy is linear with perturbation f (Equation 4.48). When there is more than one particle at the interface, the long-range deformation does not contribute to any particle-particle interaction in order $\gamma R^2 O\left(\delta^4\right)$. The leading particle-particle interaction would emerge when the separation between two particles d is of some intermediate scale $a \ll d \ll R$. In this region, deformation of interface can be approximated by linear combination of quadrupole fields from the two particles. We consider this problem in the following chapter.

CHAPTER 5

INTERACTION OF PARTICLES AT CYLINDRICAL INTERFACE

In this chapter, we describe calculations of the interaction between 2 spherical particles adsorbed on an initially cylindrical interface. From the case of the cylinders, we propose a general expression for the force on a spherical particle on a constant-mean-curvature interface. Although we found in Chapter 4 that the binding energy cannot be written as a function of local shape, we find that the in-plane force can be evaluated locally.

5.1 Calculation of interaction force

We choose to calculate the interaction of particles with a force approach, which relies only on the shape of interface near contact line [80, 19]. In principle, this should give the same answer as the energy approach, but the latter involves difficult integrals over the entire surface. We first demonstrate the interaction of two particles aligned along the axis of cylinder. Then we generalize the result to particles with arbitrary alignment with respect to the cylinder.

We hold particle 1 at $(z, \theta) = (0, 0)$ and particle 2 at $(z, \theta) = (d, 0)$ (Figure 5.1) with $a \ll d \ll R$. This choice of d allows us to approximate the deformation field as a quadrupole. And since $d \gg a$, we can superpose the quadrupole fields from particles without perturbing the contact line significantly. Thus the condition of contact angle

[0]Contributions: Anthony D. Dinsmore and Benny Davidovitch conducted the study. Chuan Zeng calculated the interaction.

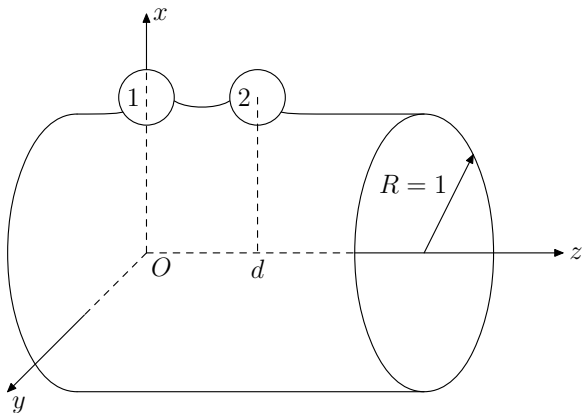

Figure 5.1: Two identical particles aligned on cylindrical interface.

is maintained to the leading order. The shape of interface can be described as $\tilde{x}(\rho, \phi)$, with polar coordinates

$$\tilde{z} = \rho \cos\phi, \tag{5.1}$$

$$\tilde{y} = \rho \sin\phi. \tag{5.2}$$

In the near vicinity of particles ($\tilde{y} \ll 1$), the cylindrical interface is approximately a parabola $\tilde{x} = 1 - \frac{1}{2}\rho^2 \sin^2\phi$. With superposition of one-particle deformations, the perturbed interface is

$$\tilde{x} = 1 - \frac{1}{2}\rho^2 \sin^2\phi - \frac{1}{4}\delta^2 \sin^2\theta_c + \frac{\delta^4 \sin^4\theta_c}{12} \frac{\tilde{z}^2 - \tilde{y}^2}{(\tilde{z}^2 + \tilde{y}^2)^2} + \frac{\delta^4 \sin^4\theta_c}{12} \frac{(\tilde{z} - \tilde{d})^2 - \tilde{y}^2}{\left[(\tilde{z} - \tilde{d})^2 + \tilde{y}^2\right]^2} \tag{5.3}$$

$$\begin{aligned} &= 1 - \frac{1}{2}\rho^2 \sin^2\phi - \frac{1}{4}\delta^2 \sin^2\theta_c + \frac{\delta^4 \sin^4\theta_c \cos 2\phi}{12\rho^2} \\ &\quad + \frac{\delta^4 \sin^4\theta_c}{12} \frac{\rho^2 \cos 2\phi - 2\tilde{d}\rho\cos\phi + \tilde{d}^2}{\left(\rho^2 - 2\tilde{d}\rho\cos\phi + \tilde{d}^2\right)^2}, \end{aligned} \tag{5.4}$$

where the last term corresponds to the deformation caused by particle 2. Near the contact line of particle 1, $\rho \sim \delta \ll \tilde{d}$. $\tilde{x}(\rho, \phi)$ can be expanded as

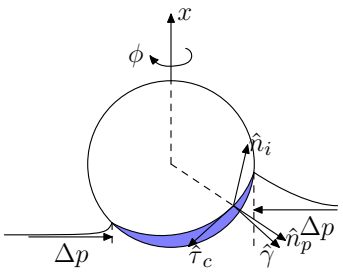

Figure 5.2: Forces on a particle sitting at a curved interface. $\hat{\boldsymbol{\gamma}}$ is the unit vector along the direction of capillary force. Δp is the Laplace pressure. The part of particle immersed inside the cylinder is shown in blue.

$$\begin{aligned}\tilde{x} =& 1 - \frac{1}{2}\rho^2 \sin^2\phi - \frac{1}{4}\delta^2 \sin^2\theta_c + \frac{\delta^4 \sin^4\theta_c \cos 2\phi}{12\rho^2} \\ &+ \frac{\delta^4 \sin^4\theta_c}{12\tilde{d}^2}\left[1 + \frac{2\rho\cos\phi}{\tilde{d}} + \frac{3\rho^2\cos 2\phi}{\tilde{d}^2} + \frac{4\rho^3\cos 3\phi}{\tilde{d}^3} + O\left(\frac{\rho^4}{\tilde{d}^4}\right)\right].\end{aligned} \tag{5.5}$$

At any point on the contact line, the direction of capillary force $\hat{\boldsymbol{\gamma}}$ is perpendicular to both the normal of interface $\hat{\boldsymbol{n}}_i$ and the tangent of contact line $\hat{\boldsymbol{\tau}}_c$ (Figure 5.2). The capillary force exerted on particle 1 is

$$\mathbf{F}^{(\gamma)} = \int_0^{2\pi} \gamma\sqrt{a^2\sin^2\theta_c + (\partial_\phi x)^2}\mathrm{d}\phi\hat{\boldsymbol{\gamma}}. \tag{5.6}$$

We are interested in the lateral component

$$F_z^{(\gamma)} = \gamma\int_0^{2\pi} \sqrt{a^2\sin^2\theta_c + (\partial_\phi x)^2}\mathrm{d}\phi\hat{\boldsymbol{\gamma}}\cdot\hat{\boldsymbol{z}} \tag{5.7}$$

where $\hat{\boldsymbol{z}} = \hat{\boldsymbol{\rho}}\cos\phi - \hat{\boldsymbol{\phi}}\sin\phi$. It can be shown that [19, 80]

$$\hat{\boldsymbol{\gamma}}\cdot\hat{\boldsymbol{z}} = \cos\psi\cos\phi + \frac{\partial_\phi\tilde{x}}{\delta\sin\theta_c}\sin\psi\sin\phi \tag{5.8}$$

where $\psi = \arctan\partial_\rho\tilde{x}$ is the slope angle of interface at the contact line. Combining Equations 5.5, 5.8, 5.7, we get

$$F_z^{(\gamma)} = \frac{\pi\gamma R\delta^6\sin^6\theta_c}{6\tilde{d}^3} + \frac{\pi\gamma R\delta^8\sin^8\theta_c}{3\tilde{d}^5}. \tag{5.9}$$

Another contribution to the interaction force is the Laplace pressure $\frac{\gamma}{R}$, where $R = 1$. Integrate along the contact line:

$$F_z^{(p)} = -\gamma \int_0^{2\pi} \left[\tilde{x}\left(\delta \sin\theta_c, \phi\right) - 1\right] \sqrt{a^2 \sin^2\theta_c + \left(\partial_\phi x\right)^2} \mathrm{d}\phi \cos\phi, \tag{5.10}$$

$$= -\frac{\pi\gamma R\delta^6 \sin^6\theta_c}{6\tilde{d}^3}. \tag{5.11}$$

The total force is then

$$F_z = F_z^{(\gamma)} + F_z^{(p)} = \frac{\pi\gamma R\delta^8 \sin^8\theta_c}{3\tilde{d}^5}. \tag{5.12}$$

The interaction is *attractive* since we are calculating the force on particle 1 and particle 2 is placed at positive z (Figure 5.1). If we take the derived perturbation for the cylinder, there will be a correction to the force in the order of $O\left(\frac{\gamma R\delta^{10}}{\tilde{d}^5}\right)$.

For arbitrary alignment, similar calculation can be performed if particle 2 is placed at $(z, R\theta) = (d\cos\omega, d\sin\omega)$ (Figure 5.3), yielding

$$F_z = \frac{\pi\gamma R\delta^8 \sin^8\theta_c}{3\tilde{d}^5} \cos 5\omega, \tag{5.13}$$

$$F_y = \frac{\pi\gamma R\delta^8 \sin^8\theta_c}{3\tilde{d}^5} \sin 5\omega. \tag{5.14}$$

Defining the unit vector from particle 1 to particle 2 as $\hat{\boldsymbol{d}} = \hat{\boldsymbol{z}}\cos\omega + \hat{\boldsymbol{y}}\sin\omega$, the in-line component of the interaction force is

$$F_d \equiv \boldsymbol{F}\cdot\hat{\boldsymbol{d}} = \frac{\pi\gamma R\delta^8 \sin^8\theta_c}{3\tilde{d}^3} \cos 4\omega. \tag{5.15}$$

The interaction could be either attractive or repulsive for different angle ω.

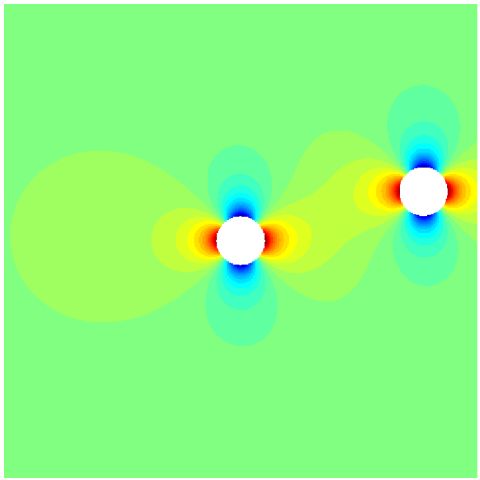

Figure 5.3: Superposition of two quadrupole fields. Red represents outward deformation; blue represents inward deformation.

Correspondingly the tangential direction is defined as $\hat{\boldsymbol{\omega}} = -\hat{\boldsymbol{z}}\sin\omega + \hat{\boldsymbol{y}}\cos\omega$ and thus

$$F_\omega \equiv \boldsymbol{F}\cdot\hat{\boldsymbol{\omega}} = \frac{\pi\gamma R\delta^8\sin^8\theta_c}{3\tilde{d}^5}\sin 4\omega. \tag{5.16}$$

It can be verified that Newton's third law holds so that the force on particle 2 is $\boldsymbol{F}' = -\boldsymbol{F}$. The vector field of $\boldsymbol{F}'$ with respect to particle 1 is drawn in Figure 5.4. By projecting the force onto the radial direction to the particle 2 from particle 1, one can show that the interaction is attractive for ω within $\pi/8$ from the y, z axes. The other component of the interparticle force is along the direction of increasing angle ω, which determines the alignment of the pair. It turned out that the pair would always align to the closest axes, as shown in Figure 5.4. Due to the interaction (Equations 5.13 and 5.14), particles tend to form chains along either axes.

5.2 Analogy to electrostatics

As described in Section 1.3.2.1, the Cheerios effect is analogous to Colombia interaction in two dimensions. The interaction of particles at cylindrical interface can also be mapped onto two-dimensional electrostatics. In the Cheerios effect, the vertical

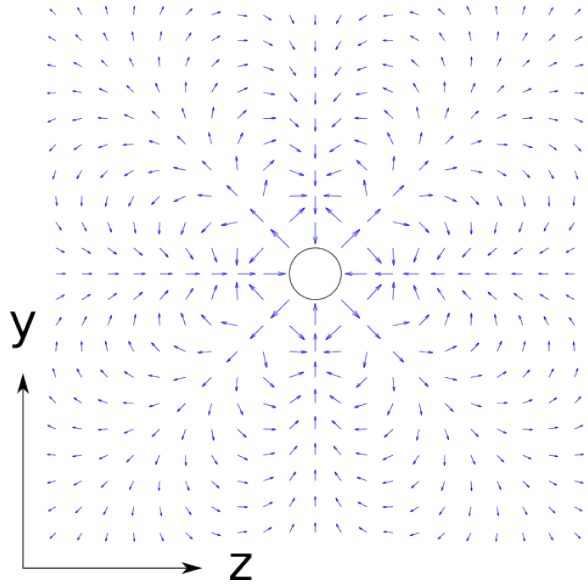

Figure 5.4: Force field of particle 2 with respect to particle 1. The arrows show the force on a spherical particle located at the center of the arrow, given there is a particle at the origin. The magnitudes are not drawn to scale.

force acting on particles can be defined as capillary point charge, corresponding to deformation of interface around contact line to one direction, either up or down. A positive charge corresponds to upward or outward deformation, while negative charge corresponds to downward or inward deformation. For particles adsorbed to cylindrical interfaces, the short-range deformation corresponds to capillary quadrupoles. Particles interact as two-dimensional quadrupoles, while the orientations of the quadrupoles are fixed with respect to the axis of the cylindrical interface.

5.3 Conjectured general form of the curvature effect

Our result for the interaction between two different spheres at a cylindrical interface allows us to explore the more general problem of a single sphere at an interface with constant mean curvature but non-uniform Gaussian curvature. If we place a particle of arbitrary radius a at the origin, the Gaussian curvature of the perturbed cylindrical interface can be calculated using [81]

$$K = \frac{\partial_{y,y}x\partial_{z,z}x - \left(\partial^2_{y,z}x\right)^2}{\left[1 + \left(\partial_y x\right)^2 + \left(\partial_z x\right)^2\right]^2}. \tag{5.17}$$

In polar coordinates (d, ω), we obtain

$$K = -\frac{1}{2R^2}\left(\frac{a\sin\theta_c}{d}\right)^4 \cos 4\omega + O\left(\frac{a^8}{R^2 d^8}\right). \tag{5.18}$$

Remarkably, for the second particle with radius $b \sim a$, the result for K completely accounts for d, ω dependence so that we can write

$$\boldsymbol{F} = -\frac{\pi\gamma b^4 \sin^4\theta_c}{6}\nabla K + O\left(\frac{\gamma a^4 b^6}{R^4 d^5}\right) + O\left(\frac{\gamma a^6 b^4}{R^4 d^5}\right). \tag{5.19}$$

Correspondingly, the potential energy regarding to the position of particle at a curved interface may be written as

$$U(\boldsymbol{r}) \approx \frac{\pi\gamma b^4 \sin^4\theta_c}{6} K(\boldsymbol{r}). \tag{5.20}$$

We propose that this is a general result for constant-mean-curvature surfaces.

While our result agrees with that of the pioneering work of Würger [60], the difference in scope are summarized in Table 5.1. Würger worked on the case where small Gaussian curvature dominates zero mean curvature. In our problem, Gaussian curvature is much smaller than the finite mean curvature, but the gradient of Gaussian curvature could have a wide range when compared with H^3. In both works, the size of particle should be much smaller than any characteristic scale of the constant mean curvature surface.

5.4 Experimental measurement of interfacial topography

The topography of fluid interface can be measured directly using scanning force microscope (SFM) by Kathleen McEnnis in Professor T. P. Russell's group in the

Table 5.1: Some dimensionless ratios characterizing the interfacial geometry. H and K are the curvatures that exist before a test particle is inserted onto the interface.

Dimensionless Ratio	Zeng et al.	Würger
K/H^2	$(a/d)^4 \ll 1$	$\gg 1(\to \infty)$
$\nabla K/H^3$	Ra^4/d^5	$\gg 1(\to \infty)$
$\nabla K/\lvert K\rvert^{3/2}$	$Rd/a^2 \gg 1$	$\gg 1$

Polymer Science and Engineering Department, UMass Amherst. A typical set of data is shown in Figure 5.5. The height map $z(x, y)$ of fluid interface and particle surface exposed in air is scanned over an area of micron scale. In this section, I describe numerical methods developed for the purpose of analyzing these images.

The contact line where the fluid interface meets a particle surface can be detected using image segmentation techniques, particularly thresholding the Laplacian of the height map. At the contact line, the gradient of height is discontinuous from fluid interface to particle surface, resulting in a large absolute value of Laplacian. Morphological operators [82] can be applied to clean up the artifacts caused by noise.

5.4.1 Mean curvature and Gaussian curvature

Once the particle surface is distinguished from the fluid interface, the mean curvature and Gaussian curvature of the surface can be calculated from the height map. We use [54, 81]

$$H = \frac{\left[1 + (\partial_x z)^2\right] \partial^2_{y,y} z - 2\partial_x z \partial_y z \partial^2_{x,y} z + \left[1 + (\partial_y z)^2\right] \partial^2_{x,x} z}{\left[1 + (\partial_x z)^2 + (\partial_y z)^2\right]^{3/2}}, \tag{5.21}$$

$$K = \frac{\partial_{x,x} z \partial_{y,y} z - \left(\partial^2_{x,y} z\right)^2}{\left[1 + (\partial_x z)^2 + (\partial_y z)^2\right]^2}. \tag{5.22}$$

Because direct numerical differentiation (finite difference) would be dominated by measurement error, we chose to fit small patches of surface with a quadric form and then read the first and second derivatives from the quadric form. For each point in

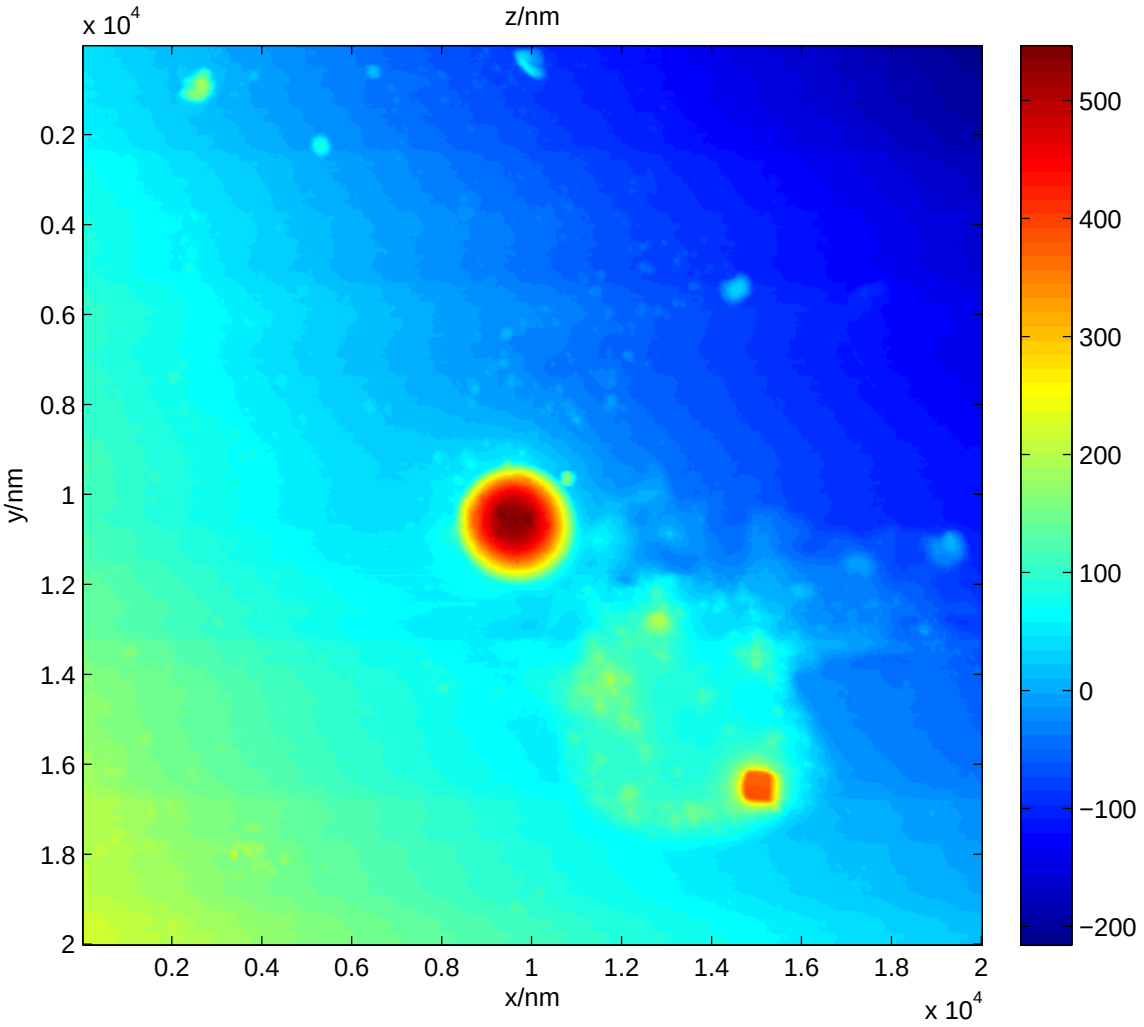

Figure 5.5: Height map of a silica particle at the interface of polystyrene and air scanned using SFM. The particle radius is 4 μm, part of which is above the interface at the center of the height image. (Data from Kathleen McEnnis.)

the height map, $z(x_0, y_0)$, we fit the surface patch $z(x, y)$, $x \in [x_0 - w/2, x_0 + w/2]$, $y \in [y_0 - w/2, y_0 + w/2]$ to

$$z = A + Bx' + Cy' + Dx'^2 + Ex'y' + Fy'^2, \tag{5.23}$$

where $x' := x - x_0, y' := y - y_0$. The width of window w must be chosen to be small enough so that cubic terms about x' and y' are negligible compared with linear and quadric terms. On the other hand, w has to be large enough so that the fit is robust against measurement error at each scanning point. A typical choice for w in our analysis is half of the particle radius.

The standard method of least squares was applied to obtain the fitting parameters A to F. The derivatives needed for curvature calculation can be read directly as

$$\partial_x z = B, \tag{5.24}$$

$$\partial_y z = C, \tag{5.25}$$

$$\partial^2_{x,x} z = 2D, \tag{5.26}$$

$$\partial^2_{x,y} z = E, \tag{5.27}$$

$$\partial^2_{y,y} z = 2F. \tag{5.28}$$

Notice that $\partial_x = \partial_{x'}, \partial_y = \partial_{y'}$. H and K can then calculated using Equations 5.21, 5.22.

Special care should be taken when the point (x_0, y_0) is close to the contact line. If the contact line passes the patch $x \in [x_0 - w/2, x_0 + w/2]$, $y \in [y_0 - w/2, y_0 + w/2]$, part of the patch is particle surface instead of fluid interface. The region of particle surface should be excluded from the least squares fitting. This is realized by labeling the region of particle surface with a mask.

5.4.2 Contact angle

The contact angle can be measured at every point at the contact line. Our initial assumption of constant contact angle can thus be tested directly.

To measure contact angle from an image, we consider one point at the contact line (x_0, y_0). Again we investigate the surface patch $x \in [x_0 - w/2, x_0 + w/2]$, $y \in [y_0 - w/2, y_0 + w/2]$. Since the contact line passes the center of the patch (x_0, y_0), part of the patch is fluid interface and the rest is particle surface. By definition, (x_0, y_0) is a common point shared by the fluid interface and particle surface. Contact angle is defined as the angle between $\hat{\boldsymbol{n}}_i$ and $\hat{\boldsymbol{n}}_p$, where $\hat{\boldsymbol{n}}_i$ is the unit normal vector of fluid interface at (x_0, y_0), and $\hat{\boldsymbol{n}}_p$ is the unit normal vector of particle surface at the same point. The unit normal of surface is related to the first derivatives as

$$\hat{\boldsymbol{n}} = \frac{(-\partial_x z, -\partial_x z, 1)}{\sqrt{1 + (\partial_x z)^2 + (\partial_y z)^2}}. \tag{5.29}$$

Therefore, we need to find the first derivatives of fluid interface at (x_0, y_0), as well as that of particle surface at the same point. This can be done by fitting patches of surface to linear forms. An alternative is to reuse the result of quadric fittings in the previous subsection (Equations 5.24, 5.25). The contact angle θ_c is finally obtained by

$$\theta_c = \arccos\left(\hat{\boldsymbol{n}}_i \cdot \hat{\boldsymbol{n}}_p\right). \tag{5.30}$$

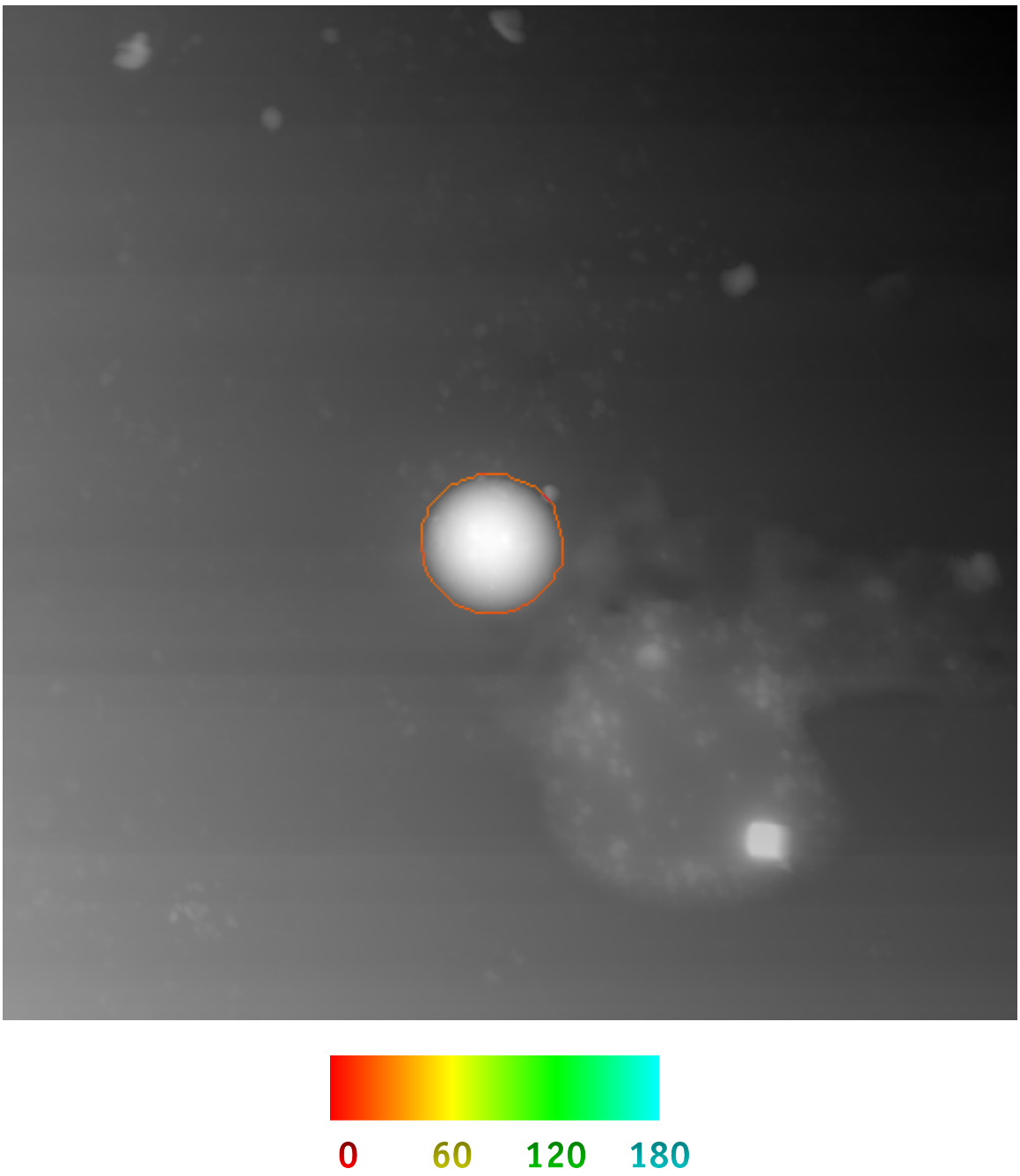

Figure 5.6: Silica particle at the interface of polystyrene and air. The gray scale shows the height map from SFM, which is the same set of data as in Figure 5.5. The color ring shows detected contact line. The color on the contact line indicates the contact angle at each point. The palette is hue in the HSB/HSL encodings of RGB [83]. The contact angle is around 30° as shown in the figure.

CHAPTER 6

GENERALIZED FORCE BETWEEN TWO PARTICLES AT AN INTERFACE: A CORRECTION OF THE CHEERIOS MODEL

With the result from previous chapters, we can revisit the Cheerios effect as introduced in Section 1.3.2.1 and extend the discussion of curvature effect to the case of non-zero normal forces. Here we show that the standard model for Cheerios effect leaves out an important piece which can in some cases be dominant.

6.1 Gravity and curvature: monomer-quadrupole interaction

Consider two particles adsorbed to an otherwise flat interface as shown in Figure 6.1. Assume there is a vertical force f on particle 1, while there is no external force on particle 2. As predicted by the standard model of Cheerios effect, the two particles do not interact with each other. However, particle 2 is adsorbed to a curved interface, the curvature of which is caused by the vertical force on particle 1. According the curvature effect described in the previous chapter, particle 2 should experience an in-plane force because of the curvature.

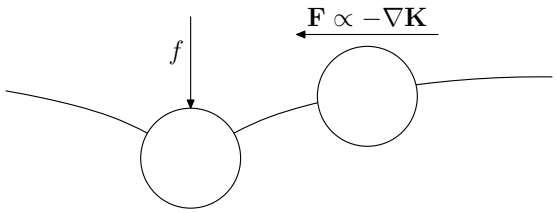

Figure 6.1: Interaction between a "heavy" particle and a "neutral" particle.

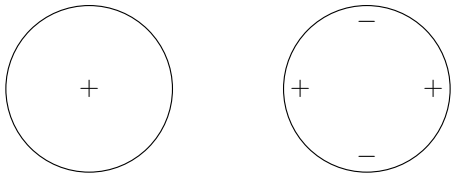

Figure 6.2: Orientation of quadrupole induced by a monopole.

The deformation caused by f is proportional to $\ln r$. Then, in the limit of small deformation, the distribution of Gaussian curvature K is proportional to $\frac{1}{r^4}$. According to prediction (5.20), the lateral capillary force on particle 2 is proportional to $-\nabla K$. The corresponding interaction potential is

$$U(d) = -\frac{f^2 b^4 \sin^4 \theta_c}{24\pi\gamma d^4}, \tag{6.1}$$

where a and θ_c are radius and contact angle of particle 2, respectively, and d is the separation between centers of the two particles. Notice the interaction is always attractive regardless of the sign of f, and it does not depend on any property of particle 1. Compared with the Cheerios effect as originally introduced, the monopole-quadrupole interaction is of higher-order in b/d and shorter-range ($U \sim d^{-4}$). Nonetheless, the curvature effect can predominate, as shown by the case where the vertical force on one of the two particles is zero, where the standard model predicts $\mathbf{F} = \mathbf{0}$.

The predicted curvature effect can also be shown directly from calculation of interfacial deformation and the consequential capillary force on particles. The curvature of interface induces quadrupolar deformation around particle 2. One can calculate the capillary force on particle 2 by integrating the tangential force and Laplace pressure as we did in the previous chapter. The result of force is equal to the prediction (6.1).

In analogy to electrostatics, the curvature capillary force corresponds to interaction between a monopole and an induced quadrupole. The quadrupole is oriented so that the interface deforms in the same direction as the monopole at the point closest to particle 1 and the point furthest to particle 1 (Figure 6.2). Because capillary

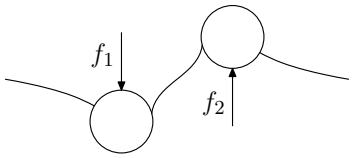

Figure 6.3: General Cheerios effect. In this example particle 1 has a net downward force while particle 2 has a net upward force, *e.g.* because of buoyancy.

charges of the same sign attract each other, this alignment of induced quadrupole with respect to monopole ensures that the interaction is always attractive.

6.2 Curvature correction to Cheerios effect

The higher-order correction can be applied to general Cheerios effect, in which different vertical forces are acting on particles (Figure 6.3). We show that the interaction between two particles is

$$U(d) = \frac{f_1 f_2}{2\pi\gamma} \ln d - \frac{f_1^2 b^4 \sin^4\theta_c}{24\pi\gamma d^4} - \frac{f_2^2 a^4 \sin^4\theta_c}{24\pi\gamma d^4} + \cdots \tag{6.2}$$

The first term is the lowest order Cheerios interaction, *i.e.*, monopole-monopole interaction which was described in Chapter 1. The second term is the interaction between monopole f_1 and the quadrupole induced by f_1 around particle 2 because the deformation from f_1 is not axisymmetric about particle 2. The third term is the symmetric counterpart of the second term, *i.e.*, the interaction between monopole f_2 and the quadrupole induced by f_2 around particle 1. We will show that in some relevant cases, the second and third terms are dominant.

In the context of electrostatics, this is the finite-size extension to the original Cheerios effect, in which particles can be treated as point charges. When the finite sizes of particles are taken into consideration, the contact lines act as conducting shells. The capillary charge can be freely distributed around the contact line while maintaining the total value. As the size of one particle tends to zero, the induced

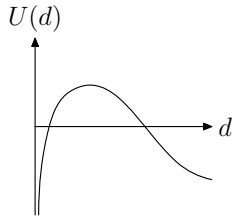

Figure 6.4: Predicted interaction potential between a "heavy" particle and a "light" particle.

quadrupole around it vanishes. And there could be even higher-order terms beyond monopole-quadrupole interaction, which are not addressed in the present study.

The case when f_1 and f_2 have opposite sign is of great interest to experimentalists, because monopole-monopole interaction compete with the monopole-quadrupole interaction (Figure 6.4). The combined interaction features an unstable critical separation. Within the critical separation, the heavy particle attracts the light particle, which is contradict with monopole-monopole Cheerios effect.

In [22], Vella *et al.* showed a similar short-range attraction between two plates at a fluid interface. In the long-range, a wetting plate and a nonwetting plate repel each other. If the plates are both wetting or both nonwetting, they attract each other. However, there is a short-range attraction between them regardless of their wetting properties. This is qualitatively the same as the interaction between two particles at an interface.

6.3 Relevance to cluster-monomer interaction

As reported in Section 2.5, isolated particle pairs at an air-water interface do not show significant interaction. In addition, there were no measurable forces between monomers and large clusters at the air-water interface. However, attraction between clusters and monomers were observed at the interface between air and trifluoroheptan-2-ol. We now investigate whether the gravity-induced deformation of the interface (*i.e.*, the modified Cheerios effect) can explain these results.

We assume 90° contact angle for simplicity (the forces would be weaker if the the angle is not 90°.). Consider the interaction between a monomer and a cluster with N particles. The cluster can be approximated as a disk with radius $b \approx \sqrt{N}a$, where a is the radius of a monomer. If the normal force accumulates linearly, the normal force f_2 on the cluster is proportional to f_1 on a monomer:

$$f_2 = Nf_1. \tag{6.3}$$

From Equation 6.2, interaction force between the cluster and a monomer is

$$F(d) = \frac{f_1 f_2}{2\pi\gamma d} + \frac{f_1^2 b^4}{6\pi\gamma d^5} + \frac{f_2^2 a^4}{6\pi\gamma d^5}. \tag{6.4}$$

The first term corresponds to monopole-monopole term, and the other terms correspond to interactions involving quadrupoles. Then

$$\frac{F_{\text{quad}}}{F_{\text{mono}}} = \frac{\frac{f_1}{f_2}b^4 + \frac{f_2}{f_1}a^4}{3d^4}, \tag{6.5}$$

$$\approx \frac{\left(\frac{1}{N}N^2 + N\right)a^4}{d^4}, \tag{6.6}$$

$$\approx N\left(\frac{a}{d}\right)^4. \tag{6.7}$$

If $d \ll N^{\frac{1}{4}}a$, we have $F_{\text{quad}} \gg F_{\text{mono}}$. However, the distance between the monomer and cluster can not be less than the sum of their radius:

$$d \geq a + b \approx \sqrt{N}a. \tag{6.8}$$

Therefore, according to assumption 6.3, the correction due to curvature would not dominate over the usual Cheerios force between two monomers. We showed in Chapter 2 that this force scale is 10^{-21} N for the case of air-water. This magnitude of force is

far below the detectable limit of our experiments (which is of order fN) so the model is consistent with our results. For the interface between air and trifluoroheptan-2-ol, the order of magnitude of the Cheerios force is smaller because of the smaller density difference ($\sim 10^{-23}$ N). In this case, the generalized Cheerios model cannot explain the measured forces on the order of 70 fN. We propose that these large forces are induced by charge dissociation on the oil side of the particle [61, 62, 63, 64, 30].

6.4 Design of experiments to demonstrate the curvature effect

If one can show experimentally the short-range attraction between heavy particle and light particle, it will serve as direct evidence of higher-order correction to the Cheerios effect. We are interested in the critical separation between the heavy particle and light particle, beyond which the interaction is repulsive, and within which the interaction is attractive. This critical separation d_c corresponds to the unstable equilibrium point in Figure 6.4. From Equation 6.2 and $\partial_d U = 0$, we have

$$d_c = 3^{-\frac{1}{4}} \left(-\frac{f_1}{f_2} b^4 \sin^4 \theta_c - \frac{f_2}{f_1} a^4 \sin^4 \theta_c \right)^{\frac{1}{4}}. \tag{6.9}$$

Note that f_1 and f_2 are with opposite sign, and in general the two particles can have different contact angle with the fluid interface. Considering the hard-core repulsion, we need $d_c \geq a+b$. Nesrin Senbil is currently investigating this effect with millimeter-sized spheres at an oil-water interface.

Alternatively, one can measure the force between a solid cylinder and a floating particle. A solid cylinder vertically dipped across a fluid interface (such as a micropipette held perpendicular to the interface) can perturb the interface if it makes a contact angle $\theta_c \neq 90°$. A cylinder with radius a generates a capillary monopole of $f_1 = 2\pi\gamma a \cos\theta_c$, corresponding to a height profile of interface $h(r) = -a\cos\theta_c \ln r$.

CHAPTER 7

COLLOIDAL CLUSTERS AT LIQUID INTERFACES

7.1 Introduction

As summarized in Section 1.3, particles adsorbed at liquid interfaces attract each other for various reasons, the consequence of which is the formation of clusters. If the attraction is induced by a normal force f on each monomer, the deformation of an otherwise flat interface near one particle is shown as Equation 1.16 involving the modified Bessel function of the second kind. For the limiting case of $r \ll l_c$, it reduces to

$$h(r) = \frac{f}{2\pi\gamma} \ln r, \quad r \ll l_c, f \ll \gamma r, \tag{7.1}$$

where γ is the interfacial tension. As a shortcut[1], the attraction potential between two monomers can be obtained by considering the work done by f on particle 2 over a normal displacement $h(r)$, *i.e.*

$$U(r) = fh(r), \tag{7.2}$$

$$= \frac{f^2}{2\pi\gamma} \ln r. \tag{7.3}$$

The attraction between a cluster and a monomer is stronger than that between two monomers, but whether or not it is proportional to the number of particles N in the

[1]The interaction energy is a combination of work done by the vertical forces on each particle plus the change of interfacial energy. It can be shown that the interfacial energy cancels the work done by one of the vertical forces. Thus the interaction between two particles is approximately the work done by one force f along the vertical direction (Section 1.3.2.1).

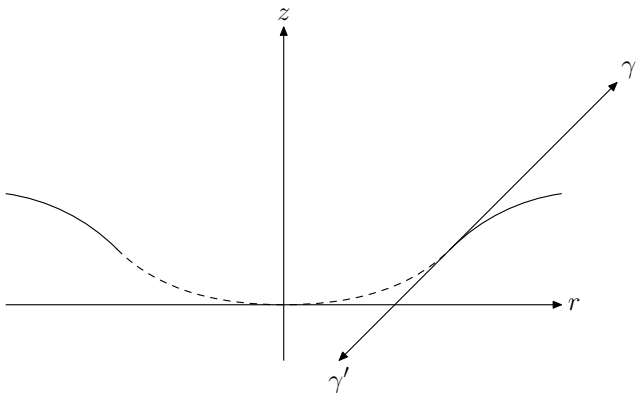

Figure 7.1: Height profile of liquid interface with a cluster of heavy particles, a cross-section view. The dashed line denotes the interface occupied by the cluster. We assume the deformation along z is very small, while in the illustration it is exaggerated.

cluster is a nontrivial question. Furthermore, as we shown in previous chapters, the deformation caused by one particle has non-uniform Gaussian curvature. As a result, particle 2 near particle 1 would also feel a curvature-driven force. We want to know the impact of this curvature-driven force compared with the vertical-force-induced attraction (7.3).

In the present investigation, we model the cluster as a continuous modified interface with effective tension γ' which is a function of particle number density and adsorption energy [70]. This approximation is valid in the case when N is large. We further assume the particles form an isotropic two-dimensional liquid. We try to answer the above questions with this simple continuous model.

7.2 Cheerios cluster

Consider an initially flat liquid interface with heavier particles adsorbed. The particles form a cluster due to the Cheerios effect and perhaps in combination with a short-range van der Waals attraction. In the horizontal plane, the projection of the cluster is a disk since we assumed that the particles act like an isotropic 2D liquid. In the region of interface without particles, the pressure difference is approximated

as zero. Here we neglect the possible density mismatch between the two fluids by assuming the scale $r \ll l_c$. For the region of interface occupied by the cluster (dashed line in Figure 7.1), the vertical forces f on the particles act on the modified interface like a downward pressure. The consequence of this pressure is a non-zero mean curvature of the modified interface. At the boundary between the clear interface and modified interface, the mismatch between γ and γ' causes the cluster to be stretched. Note that γ is always greater than γ', otherwise the particles will not be adsorbed to the interface.

Suppose the cluster can resist positive tension along its tangential direction, which is the same as the direction of γ'. Then the boundary condition for the height profile is continuity of value and first derivative, so that the force is balanced at any point on the boundary. If the deformation is very small, the force f from the weight of the particles is almost normal to the modified interface despite the deformation[2]. For a cluster with radius R and N particles, the pressure on the modified interface is roughly $Nf/\pi R^2$. The profile $z(r)$ satisfies

$$\gamma' \nabla^2 h_N(r) = \frac{Nf}{\pi R^2}, \quad r \leq R, \tag{7.4}$$

where $\nabla^2 = \frac{1}{r}\partial_r r \partial_r$. The solution is

$$h_N(r) = \frac{Nf}{4\pi\gamma' R^2} r^2 + \text{const.} \tag{7.5}$$

The pressure on the clear interface is zero, corresponding to differential equation

$$\gamma \nabla^2 h_N(r) = 0, \quad r \geq R. \tag{7.6}$$

[2]For finite deformation of interface, the force f has a component tangential to the deformed cluster, the consequence of which is a compression of the cluster.

The solution for $r \geq R$ is proportional to $\ln r$ with a constant shift. Applying the continuity of first derivative at $r = R$, we found the height of the clear interface is

$$h_N(r) = \frac{Nf}{2\pi\gamma'} \ln r, \quad r \geq R, N \gg 1. \tag{7.7}$$

Compared with Equation 7.1, we see that the height is amplified linearly with N and a factor of γ/γ'.

If the density mismatch between the two fluids is $\Delta\rho$, Equation 7.4 and 7.6 become

$$\gamma'\nabla^2 h_N(r) = \begin{cases} \dfrac{Nf}{\pi R^2} - \Delta\rho g h_N(r), & r \leq R, \\ -\Delta\rho g h_N(r), & r \geq R. \end{cases} \tag{7.8}$$

The profile $h_N(r)$ can be solved in the similar way as in Section 1.3.2.1. The solution involves modified Bessel functions $I_0(x)$ and $K_0(x)$ for $r \leq R$ and $r \geq R$, respectively. It agrees with the results in [84], but is obtained from a much simpler interpretation.

7.3 Monomer-monomer interaction

As stated above, if there is no vertical force on the particle 2, the curvature of interface caused by the particle 1 will induce quadrupole deformation around the particle 2. We assume the induced quadrupole is additive to the monopole deformation caused by vertical force f on the particle 2. By integrating the capillary force along the three-phase contact line, we can find the magnitude of the quadrupole and calculate the force between the quadrupole around particle 2 and the monopole around particle 1. As shown in previous chapters, the result of this calculation is consistent with our $U \sim K$ relation. Particle 2 feels a curvature-induced force

$$F_\kappa = \frac{f^2 b^4 \sin^4\theta_c}{6\pi\gamma r^5}, \tag{7.9}$$

where r is the distance between the two particles, b and θ_c are radius and contact angle of particle 2, respectively. Compared with the vertical-force-induced interaction, F_κ is smaller by a factor of $\frac{1}{3}\left(\frac{b\sin\theta_c}{r}\right)^4$.

7.4 Cluster-monomer interaction

From Equation 7.7, the monopole-monopole attraction force between an N-cluster and a monomer is

$$F_f = \frac{Nf^2}{2\pi\gamma' r}. \tag{7.10}$$

The subscript f means that the attraction is induced by the vertical force f. In this case the curvature-induced force can be shown as

$$F_\kappa = \frac{N\gamma f^2 b^4 \sin^4\theta_c}{6\pi\gamma'^2 r^5}. \tag{7.11}$$

Then we have

$$\frac{F_\kappa}{F_f} = \frac{1}{3}\frac{\gamma}{\gamma'}\left(\frac{b\sin\theta_c}{r}\right)^4. \tag{7.12}$$

Since $\gamma > \gamma'$, F_κ may dominate F_f for $r \le \left(\frac{\gamma}{3\gamma'}\right)^{\frac{1}{4}} b\sin\theta_c$.

7.5 Line tension

Line tension arises from interface of two-dimensional fluids as an analogy of surface tension from interface of three-dimensional fluids. But in the current problem, the effect of line tension should be negligible as shown below.

The line tension at the boundary between cluster and clear interface is in the order of $U_{\text{colloid}}/\mu\text{m}$, where U_{colloid} is the interaction among particles at interface and the particle diameter is approximately one micron. The interfacial tension γ and γ' are both in the order of $U_{\text{molecule}}/\text{Å}^2$, where U_{molecule} is the interaction among molecules. The contribution of line tension δ on an element of boundary is $\delta\kappa$, where κ is the

curvature of the boundary line. In order to make the contribution of line tension large enough to be at least comparable to that from the interfacial tension, we need

$$\kappa \gtrsim \frac{U_{\text{molecule}} \times \mu\text{m}}{U_{\text{colloid}} \times \text{Å}^2} \sim \frac{U_{\text{molecule}}}{U_{\text{colloid}} \times 10 \text{ fm}}. \tag{7.13}$$

Then the size of cluster is roughly

$$\frac{1}{\kappa} \lesssim \frac{U_{\text{colloid}} \times 10 \text{ fm}}{U_{\text{molecule}}}. \tag{7.14}$$

We know the size of a cluster is at least $\sim \mu$m, then we need $\frac{U_{\text{colloid}}}{U_{\text{molecule}}} > 10^8$, *i.e.* $U_{\text{colloid}} > 10^8 k_{\text{B}}T$. If this were true, the cluster will *not* be liquid-like.

CHAPTER 8

CONCLUSION

The behavior of micron-sized, charged-stabilized colloidal spheres and liquid droplets confined at fluid interfaces was studied using microscopy. We measured the long-range interaction between carboxyl-modified polystyrene spheres (radius $\sim$ 1 micron) at the interface using image analysis and particle tracking. At an air-water interface, single pairs of particles isolated from others do not exhibit significant interaction down to the scale of femtonewtons. In presence of other particles and clusters around, the apparent pair-interaction is still insignificant within the resolution of our measurement. This is in agreement with the predicted capillary forces among neutral particles but contradiction with the method of extracting interaction potential from radial distribution function $g(r)$, because the $g(r)$ for our data also implies artificial repulsive interaction. In general, measurement of the interaction among interfacial particles using $g(r)$ might not reflect the true interaction potential between pairs of particles.

Aggregates of colloidal particles were observed for polystyrene particles at the interface of water and 1,1,1-trifluoroheptan-2-ol, suggesting an attractive capillary force arising from electrostatic stress on the interface. We also measured the interaction of single particles with large clusters as well as the interactions between clusters. We found strong attractive forces with a complex angular dependence owing to the anisotropy of the meniscus around a cluster. We have ruled out the contribution of gravity-induced interfacial curvature to this many-body effect. This strong collec-

tive attraction might be material-specific or dependent on the material of the sample container or the charge properties of the interface.

Theoretically, we modeled the adsorption of solid particles to curved fluid interfaces. In this modeling we consider only the capillary effect while disregarding other possible factors like gravity, electrostatics, *etc.* We have shown that the adsorption of spherical particles deforms a cylindrical interface. This deformation induces interaction among particles adsorbed to the interface, which was calculated through a force approach. The deformation is analogous to induced polarization in electrostatics, and the curvature-induced capillary interaction is analogous to the interaction between electrostatic quadrupoles in two dimensions.

For particles adsorbed to an arbitrarily curved interface, we found that the interface drives the particles to regions with lower Gaussian curvature. Our formalism opens a way to study curvature effects beyond the near-Euclidean approximation. The results may guide new methods of microparticle and nanoparticle self-assembly [85, 86]. Specifically, we can estimate the velocity of particle driven by the curvature effect. If the curved interface has a characteristic length ξ, we have $|\nabla K| \approx \xi^{-3}$. Then the velocity of a particle with radius a is

$$v = \frac{F}{6\pi\eta a}, \tag{8.1}$$

$$= \frac{\frac{\pi}{6}\gamma a^4 |\nabla K|}{6\pi\eta a}, \tag{8.2}$$

$$= \frac{1}{36}\frac{\gamma}{\eta}\left(\frac{a}{\xi}\right)^3. \tag{8.3}$$

The combination of interfacial tension γ and viscosity η gives a characteristic velocity $v^* := \gamma/\eta$. For typical values of γ and η,

$$v^* \sim \frac{10^{-2}\ \mathrm{N/m}}{10^{-3}\ \mathrm{Pa \cdot s}} = 10\ \mathrm{m/s}. \tag{8.4}$$

For $a/\xi = 1/10$, $v \sim 1$ mm/s. Even for $a/\xi = 1/100$, $v \sim 1$ μm/s, which is measurable with optical microscopy, and much stronger than what we observed for particles at flat interfaces.

Our model is based on two assumptions: constant mean curvature and constant contact angle. However, many interesting physical systems are beyond these two assumptions. If the fluid interface is affected by an external field, *e.g.* gravitational field, the mean curvature is a function of spatial coordinates. For particles with pinned contact line (*e.g.* disk-shaped particle, Janus particle), the boundary condition is distinct from that of constant contact angle. Our model could be expanded by consideration the external field and/or using other boundary conditions. Particularly in biological systems, the shape of lipid membrane is governed by the tension and pressure difference [87], which is mathematically identical to fluid interface. Our formalism could be applied to lipid membrane with inclusions, *e.g.*, proteins. The boundary conditions may differ from the constant contact angle as for solid particles.

We also expect similarities between curvature-driven interactions in different dimension. The system of interfacial tension that we studied is about two-dimensional surface in three-dimensional space, governed by Young-Laplace equation $p = 2\gamma H$. For one-dimensional boundary of two-dimensional fluids, the governing equation is $T = \sigma k$, where T is the stress across the 1D boundary, σ is the line tension associated with the boundary, and k is the curvature of the boundary. Due to the simplicity of one-dimensional boundary, there is no geometrical frustration as we found for contact contact angle for curved interface. In higher dimension, the link to general relatively may be explored, where the stress-curvature relation is described by Einstein field equations [88]

$$T_{\mu\nu} = \frac{c^4}{8\pi G} G_{\mu\nu}. \tag{8.5}$$

We expect quantitative analogy across different dimensions and a unified framework for all curvature-driven interactions.

BIBLIOGRAPHY

[1] Pickering, S. U. Emulsions. *Journal of the Chemical Society 91* (1907), 2001–2021.

[2] Zeng, C., Bissig, H., and Dinsmore, A. D. Particles on droplets: From fundamental physics to novel materials. *Solid State Communications 139*, 11-12 (2006), 547–556.

[3] McGorty, R., Fung, J., Kaz, D., and Manoharan, V. N. Colloidal self-assembly at an interface. *Materials Today 13*, 6 (2010), 34 – 42.

[4] Bragg, S. L., and Nye, J. F. A dynamical model of a crystal structure. *Proceedings of the Royal Society of London. Series A, Mathematical and Physical Sciences, 190*, 1023 (1947), 474.

[5] Bragg, L., and Lomer, W. M. A dynamical model of a crystal structure. ii. *Proceedings of the Royal Society of London. Series A, Mathematical and Physical Sciences, 196*, 1045 (1949), 171–181.

[6] Wasan, D. T., Nikolov, A. D., Lobo, L. A., Koczo, K., and Edwards, D. A. Foams, thin-films and surface rheological properties. *Progress in Surface Science 39*, 2 (1992), 119–154.

[7] Israelachvili, J. N. *Intermolecular and Surface Forces*, 3rd ed. Elsevier, 2011.

[8] *Capillary and Wetting Phenomena - Drops, Bubbles, Pearls, Waves*. Springer, 2002.

[9] Lin, Y., Skaff, H., Emrick, T., Dinsmore, A. D., and Russell, T. P. Nanoparticle assembly and transport at liquid-liquid interfaces. *Science 299*, 5604 (2003), 226–229.

[10] Levine, S., and Bowen, B. D. Capillary interaction of spherical-particles adsorbed on the surface of an oil-water droplet stabilized by the particles .1. *Colloids and Surfaces 59* (1991), 377–386.

[11] Levine, S., and Bowen, B. D. Capillary interaction of spherical-particles adsorbed on the surface of an oil-water droplet stabilized by the particles .2. *Colloids and Surfaces 65*, 4 (1992), 273–286.

[12] Levine, S., and Bowen, B. D. Capillary interaction of spherical-particles adsorbed on the surface of an oil-water droplet stabilized by the particles .3. effective interfacial-tension. *Colloids and Surfaces a-Physicochemical and Engineering Aspects 70*, 1 (1993), 33–45.

[13] Pieranski, P. Two-dimensional interfacial colloidal crystals. *Physical Review Letters 45*, 7 (1980), 569–572.

[14] Hurd, A. J. The electrostatic interaction between interfacial colloidal particles. *Journal of Physics A: Mathematical and General 18* (1985), L1055–L1060.

[15] Dominguez, A., Frydel, D., and Oettel, M. Multipole expansion of the electrostatic interaction between charged colloids at interfaces. *Physical Review E (Statistical, Nonlinear, and Soft Matter Physics) 77*, 2 (2008), 020401.

[16] Hsu, M. F., Dufresne, E. R., and Weitz, D. A. Charge stabilization in nonpolar solvents. *Langmuir 21*, 11 (2005), 4881–4887.

[17] Aveyard, R., Clint, J. H., Nees, D., and Paunov, V. N. Compression and structure of monolayers of charged latex particles at air/water and octane/water interfaces. *Langmuir 16*, 4 (2000), 1969–1979.

[18] Danov, K. D., Kralchevsky, P. A., and Boneva, M. P. Electrodipping force acting on solid particles at a fluid interface. *Langmuir 20*, 15 (2004), 6139–6151.

[19] Kralchevsky, P. A., and Nagayama, K. Capillary interactions between particles bound to interfaces, liquid films and biomembranes. *Advances in Colloid and Interface Science 85*, 2-3 (MAR 31 2000), 145–192.

[20] Danov, K. D., Kralchevsky, P. A., Naydenov, B. N., and Brenn, G. Interactions between particles with an undulated contact line at a fluid interface: Capillary multipoles of arbitrary order. *Journal of Colloid and Interface Science 287* (2005), 121–134.

[21] Dominguez, A., Oettel, M., and Dietrich, S. Force balance of particles trapped at fluid interfaces. *Journal of Chemical Physics 128*, 11 (2008).

[22] Vella, D., and Mahadevan, L. The "cheerios effect". *American Journal of Physics 73*, 9 (2005), 817–825.

[23] Huh, C., and Scriven, L. E. Shapes of axisymmetric fluid interfaces of unbounded extent. *Journal of Colloid and Interface Science 30*, 3 (1969), 323.

[24] Vassileva, N. D., van den Ende, D., Mugele, F., and Mellema, J. Capillary forces between spherical particles floating at a liquid-liquid interface. *Langmuir 21*, 24 (2005), 11190–11200.

[25] Hu, D. L., and Bush, J. W. M. Meniscus-climbing insects. *Nature 437*, 7059 (2005), 733–736.

[26] Wurger, A., and Foret, L. Capillary attraction of colloidal particles at an aqueous interface. *Journal of Physical Chemistry B 109*, 34 (2005), 16435–16438.

[27] Oettel, M., Dominguez, A., and Dietrich, S. Attractions between charged colloids at water interfaces. *Journal of Physics-Condensed Matter 17*, 32 (2005), L337–L342.

[28] Oettel, M., Dominguez, A., and Dietrich, S. Effective capillary interaction of spherical particles at fluid interfaces. *Physical Review E 71*, 5 (2005), 051401.

[29] Oettel, M., Dominguez, A., and Dietrich, S. Comment on electrodipping force acting on solid particles at a fluid interface. *Langmuir 22*, 2 (2006), 846–847.

[30] Frydel, D., Dietrich, S., and Oettel, M. Charge renormalization for effective interactions of colloids at water interfaces. *Physical Review Letters 99*, 11 (2007), 118302.

[31] Dominguez, A., Oettel, M., and Dietrich, S. Absence of logarithmic attraction between colloids trapped at the interface of droplets - comment on "capillary attraction of charged particles at a curved liquid interface" by alois wurger. *Epl 77*, 6 (2007), 68002.

[32] Dominguez, A., Oettel, M., and Dietrich, S. Theory of capillary-induced interactions beyond the superposition approximation. *Journal of Chemical Physics 127* (2007), 204706.

[33] Lucassen, J. Capillary forces between solid particles in fluid interfaces. *Colloids and Surfaces 65*, 2-3 (1992), 131–137.

[34] Kralchevsky, P. A., Paunov, V. N., Denkov, N. D., and Nagayama, K. Capillary image forces: I. theory. *Journal of Colloid and Interface Science 167*, 1 (1994), 47–65.

[35] Velev, O. D., Denkov, N. D., Paunov, V. N., Kralchevsky, P. A., and Nagayama, K. Capillary image forces .2. experiment. *Journal of Colloid and Interface Science 167*, 1 (1994), 66–73.

[36] Kralchevsky, P. A., Denkov, N. D., and Danov, K. D. Particles with an undulated contact line at a fluid interface: Interaction between capillary quadrupoles and rheology of particulate monolayers. *Langmuir 17* (2001), 7694–7705.

[37] Stamou, D., Duschl, C., and Johannsmann, D. Long-range attraction between colloidal spheres at the air-water interface: The consequence of an irregular meniscus. *Physical Review E 62* (2000), 5263–5272.

[38] Brown, A. B. D., Smith, C. G., and Rennie, A. R. Fabricating colloidal particles with photolithography and their interactions at an air-water interface. *Physical Review E 62* (2000), 951–960.

[39] Bowden, N., Terfort, A., Carbeck, J., and Whitesides, G. M. Self-assembly of mesoscale objects into ordered two-dimensional arrays. *Science 276*, 5310 (1997), 233–235.

[40] Bowden, N., Choi, I. S., Grzybowski, B. A., and Whitesides, G. M. Mesoscale self-assembly of hexagonal plates using lateral capillary forces: Synthesis using the "capillary bond". *Journal of the American Chemical Society 121*, 23 (1999), 5373–5391.

[41] Wolfe, D. B., Snead, A., Mao, C., Bowden, N. B., and Whitesides, G. M. Mesoscale self-assembly: Capillary interactions when positive and negative menisci have similar amplitudes. *Langmuir 19*, 6 (2003), 2206–2214.

[42] Loudet, J. C., Alsayed, A. M., Zhang, J., and Yodh, A. G. Capillary interactions between anisotropic colloidal particles. *Physical Review Letters 94* (2005), 018301.

[43] Goulian, M., Bruinsma, R., and Pincus, P. Long-range forces in heterogeneous fluid membranes. *Europhysics Letters 22*, 2 (1993), 145.

[44] Golestanian, R. Casimir dispersion forces and orientational pairwise additivity. *Physical Review E 62*, 4 (2000), 5242 LP – 5247.

[45] Lehle, H., and Oettel, M. Importance of boundary conditions for fluctuation-induced forces between colloids at interfaces. *Physical Review E 75*, 1 (2007), 011602.

[46] Loudet, J. C., and Pouligny, B. Self-assembled capillary arrows. *Europhysics Letters 85*, 2 (2009).

[47] Loudet, J. C., Yodh, A. G., and Pouligny, B. Wetting and contact lines of micrometer-sized ellipsoids. *Physical Review Letters 97*, 1 (2006), 018304.

[48] Lehle, H., Noruzifar, E., and Oettel, M. Ellipsoidal particles at fluid interfaces. *European Physical Journal E 26*, 1-2 (2008), 151–160.

[49] van Nierop, E. A., Stijnman, M. A., and Hilgenfeldt, S. Shape-induced capillary interactions of colloidal particles. *Europhysics Letters 72*, 4 (2005), 671–677.

[50] *Elementary Differential Geometry*. Academic Press, 1997.

[51] *Differential Geometry of Curves and Surfaces*. Prentice-Hall, 1976.

[52] *Lecture Notes on Elementary Topology and Geometry*. Springer-Verlag, 1967.

[53] *Modern Differential Geometry of Curves And Surfaces With Mathematica*. CRC Press, 2006.

[54] *A comprehensive introduction to differential geometry*, 3rd ed. Publish or Perish Press, 1999.

[55] Hey, Michael J., and Kingston, John G. Maximum stability of a single spherical particle attached to an emulsion drop. *Journal of Colloid and Interface Science 298*, 1 (2006), 497 – 499.

[56] S., Komura, Hirose, Y., and Nonomura, Y. Adsorption of colloidal particles to curved interfaces. *Journal of Chemical Physics 124* (2006), 241104.

[57] Lewandowski, E. P., Bernate, J. A., Searson, P. C., and Stebe, K. J. Rotation and alignment of anisotropic particles on nonplanar interfaces. *Langmuir 24*, 17 (2008), 9302–9307.

[58] Lewandowski, E. P., Bernate, J. A., Tseng, A., Searson, P. C., and Stebe, K. J. Oriented assembly of anisotropic particles by capillary interactions. *Soft Matter 5*, 4 (2009), 886–890.

[59] Lewandowski, E. P., Cavallaro, M., Botto, L., Bernate, J. C., Garbin, V., and Stebe, K. J. Orientation and self-assembly of cylindrical particles by anisotropic capillary interactions. *Langmuir 26*, 19 (2010), 15142–15154.

[60] Würger, A. Curvature-induced capillary interaction of spherical particles at a liquid interface. *Physical Review E 74*, 4 (2006), 041402.

[61] Nikolaides, M. G., Bausch, A. R., Hsu, M. F., Dinsmore, A. D., Brenner, M. P., and Weitz, D. A. Electric-field-induced capillary attraction between like-charged particles at liquid interfaces. *Nature 420*, 6913 (2002), 299–301.

[62] Megens, M., and Aizenberg, J. Like-charged particles at liquid interfaces. *Nature 424*, 6952 (2003), 1014–1014.

[63] Nikolaides, M. G., Bausch, A. R., Hsu, M. F., Dinsmore, A. D., Brenner, M. P., Gay, C., and Weitz, D. A. Like-charged particles at liquid interfaces - reply. *Nature 424* (2003), 1014–1014.

[64] Aveyard, R., Binks, B. P., Clint, J. H., Fletcher, P. D. I., Horozov, T. S., Neumann, B., Paunov, V. N., Annesley, J., Botchway, S. W., Nees, D., Parker, A. W., Ward, A. D., and Burgess, A. N. Measurement of long-range repulsive forces between charged particles at an oil-water interface. *Physical Review Letters 88*, 24 (2002), 246102.

[65] Gomez-Guzman, O., and Ruiz-Garcia, J. Attractive interactions between like-charged colloidal particles at the air/water interface. *Journal of Colloid and Interface Science 291*, 1 (2005), 1–6.

[66] Chen, W., Tan, S. S., Ng, T. K., Ford, W. T., and Tong, P. Long-ranged attraction between charged polystyrene spheres at aqueous interfaces. *Physical Review Letters 95*, 21 (2005), 218301.

[67] Ruiz-Garcia, J. private communications, 2011.

[68] Leunissen, M. E., van Blaaderen, A., Hollingsworth, A. D., Sullivan, M. T., and Chaikin, P. M. Electrostatics at the oil-water interface, stability, and order in emulsions and colloids. *Proceedings of the National Academy of Sciences of the United States of America 104*, 8 (2007), 2585–2590.

[69] Leunissen, M. E., Zwanikken, J., van Roij, R., Chaikin, P. M., and van Blaaderen, A. Ion partitioning at the oil-water interface as a source of tunable electrostatic effects in emulsions with colloids. *Physical Chemistry Chemical Physics 9* (2007), 6405–6414.

[70] Du, K., Glogowski, E., Emrick, T., Russell, T. P., and Dinsmore, A. D. Adsorption energy of nano- and microparticles at liquid-liquid interfaces. *Langmuir 26*, 15 (2010), 12518–12522.

[71] Fernandez-Toledano, J. C., Moncho-Jorda, A., Martinez-Lopez, F., and Hidalgo-Alvarez, R. Spontaneous formation of mesostructures in colloidal monolayers trapped at the air-water interface: A simple explanation. *Langmuir 20*, 17 (2004), 6977–6980.

[72] Chen, W., Tan, S. S., Huang, Z. S., Ng, T. K., Ford, W. T., and Tong, P. Measured long-ranged attractive interaction between charged polystyrene latex spheres at a water-air interface. *Physical Review E 74*, 2 (2006), 021406.

[73] Crocker, J. C., and Grier, D. G. Microscopic measurement of the pair interaction potential of charge-stabilized colloid. *Physical Review Letters 73*, 2 (1994), 352–355.

[74] Sainis, S. K., Germain, V., and Dufresne, E. R. Statistics of particle trajectories at short time intervals reveal fN-scale colloidal forces. *Physical Review Letters 99*, 1 (2007), 018303.

[75] Bowman, A. W., and Azzalini, A. *Applied Smoothing Techniques for Data Analysis*. Oxford University Press, New York, 1997.

[76] Hoover, B, Radue, E., Bromberg, B., and Dinsmore, A. D. private communications, 2011.

[77] Davidovitch, B., Ertaş, D., and Halsey, T. C. Ripening of porous media. *Physical Review E 70*, 3 (2004), 031609.

[78] *Table of integrals, series and products*. Academic Press, New-York, 1980.

[79] *Elementary Differential Geometry*. Springer, 2000.

[80] Kralchevsky, P. A., Paunov, V. N., Denkov, N. D., Ivanov, I. B., and Nagayama, K. Energetical and force approaches to the capillary interactions between particles attached to a liquid fluid interface. *Journal of Colloid and Interface Science 155*, 2 (1993), 420–437.

[81] *Differential Geometry: Curves - Surfaces - Manifolds*. American Mathematical Society, 2006.

[82] Haralick, R. M., and Shapiro, L. G. *Computer and Robot Vision*, vol. I. Addison-Wesley, 1992.

[83] Wikipedia. Hue — Wikipedia, the free encyclopedia, 2011.

[84] Pergamenshchik, V. M. Strong collective attraction in colloidal clusters on a liquid-air interface. *Physical Review E (Statistical, Nonlinear, and Soft Matter Physics) 79*, 1 (2009), 011407.

[85] Straford, K., Adhikari, R., Pagonabarraga, I., Desplat, J. C., and Cates, M. E. Colloidal jamming at interfaces: A route to fluid-bicontinuous gels. *Science 309*, 5744 (2005), 2198–2201.

[86] Dinsmore, A. D. Colloids - a useful boundary. *Nature Materials 6*, 12 (2007), 921–922.

[87] Engelman, D. M. Membranes are more mosaic than fluid. *Nature 438*, 7068 (2005), 578–580.

[88] Carroll, S. *Spacetime and Geometry - An Introduction to General Relativity*. Benjamin Cummings, 2004.